

# **USING IMPACT MODULATION TO IDENTIFY LOOSE BOLTS ON A SATELLITE**

**Janette Jaques and Doug Adams**

**Purdue University  
Center for Systems Integrity  
1500 Kepner Drive  
Lafayette, IN 47905**

**21 Oct 2011**

**Final Report**

**APPROVED FOR PUBLIC RELEASE; DISTRIBUTION IS UNLIMITED.**



**AIR FORCE RESEARCH LABORATORY  
Space Vehicles Directorate  
3550 Aberdeen Ave SE  
AIR FORCE MATERIEL COMMAND  
KIRTLAND AIR FORCE BASE, NM 87117-5776**

## DTIC COPY

### NOTICE AND SIGNATURE PAGE

Using Government drawings, specifications, or other data included in this document for any purpose other than Government procurement does not in any way obligate the U.S. Government. The fact that the Government formulated or supplied the drawings, specifications, or other data does not license the holder or any other person or corporation; or convey any rights or permission to manufacture, use, or sell any patented invention that may relate to them.

This report is the result of contracted fundamental research deemed exempt from public affairs security and policy review in accordance with SAF/AQR memorandum dated 10 Dec 08 and AFRL/CA policy clarification memorandum dated 16 Jan 09. This report is available to the general public, including foreign nationals. Copies may be obtained from the Defense Technical Information Center (DTIC) (<http://www.dtic.mil>).

AFRL-RV-PS-TR-2011-0134 HAS BEEN REVIEWED AND IS APPROVED FOR PUBLICATION IN ACCORDANCE WITH ASSIGNED DISTRIBUTION STATEMENT.

//signed//  
WHITNEY REYNOLDS  
Program Manager

//signed//  
BRETT J. DEBLONK, Ph.D.  
Technical Advisor, Spacecraft Component Technology Branch

//signed//  
B. SINGARAJU, Ph.D.  
Deputy Chief, Spacecraft Technology Division  
Space Vehicles Directorate

This report is published in the interest of scientific and technical information exchange, and its publication does not constitute the Government's approval or disapproval of its ideas or findings.

REPORT DOCUMENTATION PAGE				Form Approved OMB No. 0704-0188	
Public reporting burden for this collection of information is estimated to average 1 hour per response, including the time for reviewing instructions, searching existing data sources, gathering and maintaining the data needed, and completing and reviewing this collection of information. Send comments regarding this burden estimate or any other aspect of this collection of information, including suggestions for reducing this burden to Department of Defense, Washington Headquarters Services, Directorate for Information Operations and Reports (0704-0188), 1215 Jefferson Davis Highway, Suite 1204, Arlington, VA 22202-4302. Respondents should be aware that notwithstanding any other provision of law, no person shall be subject to any penalty for failing to comply with a collection of information if it does not display a currently valid OMB control number. <b>PLEASE DO NOT RETURN YOUR FORM TO THE ABOVE ADDRESS.</b>					
1. REPORT DATE (DD-MM-YY) 21-10-2011		2. REPORT TYPE Final Report		3. DATES COVERED (From - To) 11-Feb-2009 – 12-Sep-2011	
4. TITLE AND SUBTITLE Using Impact Modulation to Identify Loose Bolts on a Satellite				5a. CONTRACT NUMBER  FA9453-09-1-0317	
				5b. GRANT NUMBER	
				5c. PROGRAM ELEMENT NUMBER 62601F	
6. AUTHOR(S)  Janette Jaques and Doug Adams				5d. PROJECT NUMBER MIPR	
				5e. TASK NUMBER	
				5f. WORK UNIT NUMBER 837389	
7. PERFORMING ORGANIZATION NAME(S) AND ADDRESS(ES)  Purdue University Center for Systems Integrity 1500 Kepner Drive Lafayette, IN 47905				8. PERFORMING ORGANIZATION REPORT NUMBER	
9. SPONSORING / MONITORING AGENCY NAME(S) AND ADDRESS(ES) Air Force Research Laboratory Space Vehicles Directorate 3550 Aberdeen Ave., SE Kirtland AFB, NM 87117-5776				10. SPONSOR/MONITOR'S ACRONYM(S) AFRL/RVSV	
				11. SPONSOR/MONITOR'S REPORT NUMBER(S) AFRL-RV-PS-TR-2011-0134	
12. DISTRIBUTION / AVAILABILITY STATEMENT Approved for public release; distribution is unlimited.					
13. SUPPLEMENTARY NOTES					
14. ABSTRACT This report investigates the use of Impact Modulation (IM) as a means for detecting loose bolts in a satellite structure. First, a two-beam, one-bolt assembly is studied to establish guidelines for implementing IM. Then, theoretical models are developed to provide a basis for applying IM to bolted joints. Two analysis methods for identifying loose bolts within a structure are then proposed. These methods are demonstrated on a three-beam, two-bolt structure; a four-beam, three-bolt structure; and a realistic satellite structure. The results of IM testing on the two-beam, one-bolt assembly showed that the nonlinear response of the system is significantly affected by the underlying linear characteristics of the system and that IM is an effective method for differentiating the responses of the bolted structure with different bolt torque levels. The first analysis method was able to identify the presence of loose bolts within increasingly complex structures without the use of historical data by quantifying the difference in response amplitudes at the natural frequencies and those at the sideband frequencies across an array of impact locations. The second analysis method tracked changes in bolt torque by comparing the area under the response spectra in the modulation range to a baseline reference.					
15. SUBJECT TERMS Impact Modulation, Satellite, Structural Health Monitoring, Loose Bolts					
16. SECURITY CLASSIFICATION OF:			17. LIMITATION OF ABSTRACT	18. NUMBER OF PAGES	19a. NAME OF RESPONSIBLE PERSON
a. REPORT	b. ABSTRACT	c. THIS PAGE			19b. TELEPHONE NUMBER (include area code)
Unclassified	Unclassified	Unclassified	Unlimited	140	Whitney Reynolds

(This page intentionally left blank)

## Vcdng'qh'Contents

1.0	SUMMARY	1
2.0	INTRODUCTION	1
2.1	Motivation and Problem Statement . . . . .	1
2.2	Introduction to Impact Modulation . . . . .	2
2.3	Literature Review . . . . .	3
2.3.1	Current Methods for Detecting Loose Bolts. . . . .	4
2.3.2	Bolt Models. . . . .	5
2.3.3	Applications of Impact Modulation. . . . .	7
2.4	Objectives . . . . .	7
3.0	METHODS, ASSUMPTIONS, AND PROCEDURES	8
3.1	Implementing Impact Modulation: Experimental Development and Sensitivity Analysis . . . . .	8
3.1.1	Experimental Setup and Test Procedure. . . . .	8
3.1.2	Sensitivity Study. . . . .	10
3.1.3	Conclusions. . . . .	40
3.2	Theoretical and Model Development . . . . .	41
3.2.1	Single Degree of Freedom Model. . . . .	41
3.2.2	Finite Element Model. . . . .	45
3.3	Conclusions . . . . .	68
4.0	RESULTS AND DISCUSSION	70
4.1	Using Impact Modulation for the History-Free Detection of Loose Bolts . . . . .	70
4.1.1	Method for Loose Bolt Detection. . . . .	70
4.1.2	Finite Element Model Analysis. . . . .	72
4.1.3	Three-Beam, Two-Bolt Assembly. . . . .	74
4.1.4	Four-Beam, Three-Bolt Assembly. . . . .	81
4.1.5	Satellite Panel. . . . .	87
4.1.6	Conclusions. . . . .	95
4.2	Loose Bolt Detection Using Impact Modulation With Baseline Data . . . . .	97
4.2.1	Experimental Procedure and Analysis Method. . . . .	97
4.2.2	Results. . . . .	99
4.2.3	Conclusions. . . . .	108
5.0	CONCLUSIONS	110
5.1	Conclusions . . . . .	110
5.2	Recommendations for Future Work . . . . .	111
	References . . . . .	113
	Appendix A: Simulation Parameters and MATLAB Code.....	118
	Appendix B: Newmark's Method MATLAB code.....	124

## List of Figures

Figure		Page
1	Response spectrum of a two-beam, one-bolt assembly to: (a) an impact only (b) an actuator signal only (c) to both an impact and an actuator signal as used in Impact Modulation (IM) testing. . . . .	3
2	Two-beam experimental setup. . . . .	9
3	Experimental equipment. . . . .	9
4	Setup and parameters for impact amplitude testing. The numbered, red dots represent reference nodes. . . . .	11
5	Two-beam, one-bolt setup with fixed boundary conditions. . . . .	11
6	Response spectra from an IM test from impact amplitude testing. . . . .	12
7	Scaled amplitudes of modal response ( $\circ$ ), left sidebands ( $\square$ ) and right sidebands ( $\diamond$ ) versus scaled impact amplitude from IM testing. Green lines (—) indicate a least-squares linear curve fit of each set of data. . . . .	14
8	Normalized response amplitude versus scaled impact amplitude from IM testing for left ( $\square$ ) and right ( $\diamond$ ) sidebands. The green line (—) indicates the ideal case. . . . .	15
9	Setup and parameters for impact location testing. . . . .	16
10	Scaled imaginary part of the response versus impact location as measured along the beam from IM testing for the modal response ( $\bullet$ ) and for the left ( $\blacksquare$ ) and right ( $\blacktriangleright$ ) sidebands. . . . .	17
11	Setup and parameters for sensor location testing. . . . .	18
12	Two-beam, one-bolt setup with sensor array. . . . .	18
13	Scaled imaginary part of the response versus sensor location as measured along the beam from IM testing for the modal response ( $\bullet$ ) and for the left ( $\blacksquare$ ) and right ( $\blacktriangleright$ ) sidebands. . . . .	20
14	Setup and parameters for actuator amplitude testing. . . . .	21
15	Scaled response amplitudes versus scaled actuator force amplitude from IM testing for left ( $\blacksquare$ ) and right ( $\blacktriangleright$ ) sidebands and for the response at the actuator frequency ( $\bullet$ ). . . . .	22
16	Normalized response amplitude versus scaled actuator amplitude from IM testing for left ( $\blacksquare$ ) and right ( $\blacktriangleright$ ) sidebands. The green line (—) indicates the ideal case. . . . .	23
17	Setup and parameters for actuator frequency testing. . . . .	24
18	Sideband amplitudes from IM tests using an actuator frequency of 7,500 Hz and 10,510 Hz. . . . .	25
19	Amplitude of response of the two-beam assembly when subjected to a sine sweep ( $\blacksquare$ ) and sideband amplitudes from Figure 18 ( $\circ$ ). . . . .	26
20	Setup and parameters for bolt torque sensitivity testing. . . . .	27
21	High frequency portion of the response spectra from IM testing for bolt torques of 32 in-lbs ( $\blacksquare$ ), 16 in-lbs ( $\blacktriangleright$ ), 8 in-lbs ( $\bullet$ ), 4 in-lbs ( $\blacksquare$ ), 2 in-lbs ( $\blacktriangleright$ ), 1 in-lb ( $\bullet$ ), and hand-tight ( $\blacktriangleright$ ). . . . .	28

22	Response spectra (zoomed in near the actuator frequency, 10,510 Hz) from IM testing with first right sideband highlighted with a black box for bolt torques of 32 in·lbs (█), 16 in·lbs (█), 8 in·lbs (█), 4 in·lbs (█), 2 in·lbs (█), 1 in·lb (█), and hand-tight (█). . . . .	29
23	Left (█) and right (█) sideband amplitudes versus bolt torque for the first four modes from IM testing. . . . .	31
24	Left (█) and right (█) sideband amplitudes versus bolt torque for the first four modes from IM testing. . . . .	32
25	Response spectrum near the first four modes from IM testing for bolt torques of 32 in·lbs (█), 16 in·lbs (█), 8 in·lbs (█), 4 in·lbs (█), 2 in·lbs (█), 1 in·lbs (█), and hand-tight (█). . . . .	33
26	Normalized area under the response spectrum over the left (█) and right (█) modulation spectra versus bolt torque for fixed boundary conditions using 10,510 Hz actuator frequency. . . . .	35
27	Normalized area under the response spectrum over the left (█) and right (█) modulation spectra versus bolt torque for fixed boundary conditions using 7,500 Hz actuator frequency. . . . .	36
28	Setup and parameters for boundary condition sensitivity testing. . . . .	37
29	Two-beam, one-bolt setup with free boundary conditions. . . . .	37
30	Normalized area under the response spectrum over the left (█) and right (█) modulation spectra versus bolt torque for free boundary conditions. . . . .	39
31	Force-deflection curve for the bolt stiffness used in the simulations (█). The linear force-deflection curve (█) is shown for reference. . . . .	42
32	Schematic of the single degree of freedom system. . . . .	42
33	Schematic of the two-beam, one-bolt assembly used in the finite element model simulations. . . . .	46
34	Two-bar schematic showing impact, probing force input, and sensor locations for the nominal case. The color of each square indicates the color that will be used when plotting results from that sensor location. . . . .	53
35	Response spectra from the simulation of an IM test for N=10 (nominal results). Line colors correspond to different sensor locations as indicated in Figure 34. . . . .	53
36	Scaled left and right sideband amplitudes corresponding to the first four modes versus scale factor of impact amplitude from IM simulations. Line colors correspond to different sensor locations as indicated in Figure 34. . . . .	55
37	Two-bar schematic showing impact, probing force input, and sensor locations for the impact location study. . . . .	56
38	Scaled imaginary part of the response versus impact location as measured along the beam from IM simulations measured at sensor location 7 for the modal response (█) and for the left (█) and right (█) sidebands. . . . .	57
39	Scaled imaginary part of the response versus sensor location as measured along the beam from IM simulations as measured at sensor location 7 for the modal response (█) and for the left (█) and right (█) sidebands. . . . .	58
40	(a) First right sideband deflection shape (7,598 Hz) and (b) underlying deflection shape at 7,598 Hz. . . . .	59

41	Scaled dot product between the left ( $SB_L$ ) and right ( $SB_R$ ) sidebands and the mode shape ( $M$ ), the deflection shape at the probing force frequency ( $A$ ), the point-wise multiplication of $M$ and $A$ ( $M \times A$ ), and the underlying deflection shapes at the sideband frequencies ( $U_L$ and $U_R$ ) for each of the first four modes. . . . .	60
42	Scaled left and right sideband amplitudes corresponding to the first four modes versus scale factor of probing force amplitude from IM simulations. Line colors correspond to different sensor locations as indicated in Figure 34. . . . .	62
43	Sideband amplitudes from simulated IM tests using an actuator frequency of 7,500 Hz and 10,510 Hz. . . . .	63
44	Frequency response function of the two-beam assembly when subjected to a simulated sine sweep (—) and sideband amplitudes from Figure 43 (○). . . . .	64
45	Scaled left and right sideband amplitudes corresponding to the first four modes versus scale factor of coefficients of nonlinear springs at the bolted joint from IM simulations. Line colors correspond to different sensor locations as indicated in Figure 34. . . . .	65
46	Scaled left and right sideband amplitudes corresponding to the first four modes versus scale factor of the coefficients of the linear springs at the bolted joint from IM simulations. Line colors correspond to different sensor locations as indicated in Figure 34. . . . .	66
47	Normalized area under the response spectrum over the left (—) and right (—) modulation spectra versus scale factor of the coefficients of the linear springs at the bolted joint for IM simulations with fixed boundary conditions. . . . .	67
48	Normalized area under the response spectrum over the left (—) and right (—) modulation spectra versus scale factor of the coefficients of the linear springs at the bolted joint for IM simulations with free boundary conditions. . . . .	68
49	(a) Normalized amplitudes of response at the natural frequency versus impact location. (b) Normalized sideband amplitudes versus impact location for a structure with tight bolts. (c) Normalized sideband amplitudes versus impact location for a structure with a loose bolt. . . . .	72
50	Three-beam, two-bolt setup. . . . .	73
51	Scaled response amplitudes versus impact location from IM simulation results. (Line colors correspond to the sensor locations as indicated in Figure 50b.) . . . .	73
52	Three-beam, two-bolt setup. . . . .	75
53	Setup and parameters for the three-beam, two-bolt IM testing. The color of each square indicates the color that will be used when plotting results from that sensor location. . . . .	75
54	High frequency portion of the response spectra of the three-beam, two-bolt structure to an IM test from sensor S4 and impact location I3. . . . .	77
55	Torque index versus sensor number for each sensor for Case 32-32 (—), Case 2-32 (—), and Case 32-2 (—). . . . .	77
56	Scaled response amplitudes versus impact location for the three different bolt torque cases as measured from the seven different sensors. (Line colors correspond to the sensor locations as indicated in Figure 53.) . . . . .	78
57	Torque index for Case 32-32 (—), Case 2-32 (—), and Case 32-2 (—). The green line indicates the damage threshold. . . . .	79



58	Average torque index for Case 32-32 (■), Case 4-32 (■), and Case 32-4 (■).	79
59	Average torque index for Case 32-32 (■), Case 8-32 (■), and Case 32-8 (■).	80
60	Average torque index for Case 32-32 (■), Case 8-32 (■), and Case 32-8 (■) with higher impact amplitude force. . . . .	80
61	Torque index versus torque on bolt 1. . . . .	81
62	Four-beam, three-bolt setup. . . . .	82
63	Setup and parameters for the four-beam, three-bolt IM testing. The color of each square indicates the color that will be used when plotting results from that sensor location. . . . .	82
64	High frequency portion of the response spectra of the four-beam, three-bolt structure to an IM test from sensor S7 and impact location I5. . . . .	83
65	Scaled response amplitudes versus impact location for the four different bolt torque cases as measured from the ten different sensors. (Line colors correspond to the sensor locations as indicated in Figure 63.) . . . . .	84
66	Torque index for Cases 32-32-32 (■), Case 2-32-32 (■), Case 32-2-32 (■), and Case 32-32-2 (■). . . . .	85
67	Torque index for Cases 32-32-32 (■), Case 4-32-32 (■), Case 32-4-32 (■), and Case 32-32-4 (■). . . . .	85
68	Torque index for Cases 32-32-32 (■), Case 8-32-32 (■), Case 32-8-32 (■), and Case 32-32-8 (■). . . . .	86
69	Torque index for Cases 32-32-32 (■), Case 8-32-32 (■), Case 32-8-32 (■), and Case 32-32-8 (■) with higher impact amplitude force. . . . .	86
70	Satellite panel with close-up views of the simulated component and one of the ten access plates. . . . .	88
71	The underside of the satellite panel. . . . .	88
72	Setup and parameters for the satellite panel IM testing. . . . .	89
73	Low frequency portion of the response spectra from IM testing at several impact locations. . . . .	90
74	High frequency portion of the response spectra from IM testing at several impact locations. . . . .	91
75	Scaled response amplitudes versus impact location for IM tests for Case 24. . . . .	93
76	Torque index for Case 24 for the first three modes. . . . .	94
77	Torque index for Case 24 (■), Case 2 (■), Case 1 (■), and Case 0 (■) for the first three modes. . . . .	94
78	Torque index for Case 24 (■), Case 2 (■), and Case 1 (■) for the first three modes with higher impact amplitude force. . . . .	95
79	Setup and parameters for the three-beam, two-bolt IM testing. The color of each square and of each X indicates the color that will be used when plotting results from that sensor or impact location. . . . .	99
80	Modulation index, $I$ versus torque on bolt 1 for IM testing for (a) different sensor locations and (b) different impact locations. Line colors correspond to the sensor and impact locations indicated in Figure 79. . . . .	100
81	Distributions of the modulation index, $I$ , versus bolt torque from ten repetitions of IM at each torque level for the three-beam, two-bolt structure. . . . .	101

82	Mean $I$ values versus percent loss in torque on bolt 1 (—) and a corresponding hyperbolic tangent curve fit (—) for the three-beam, two-bolt test results. . . . .	102
83	Setup and parameters for the four-beam, three-bolt IM testing. . . . .	102
84	Distributions of the modulation index, $I$ , versus bolt torque from ten repetitions of IM at each torque level for the four-beam, three-bolt structure. . . . .	104
85	Mean $I$ values versus percent loss in torque on bolt 1 (—) and a corresponding hyperbolic tangent curve fit (—) for the four-beam, three-bolt test results. . . . .	104
86	Setup and parameters for satellite panel IM testing. . . . .	105
87	Distributions of the modulation index, $I$ , versus bolt torque from ten repetitions of IM at each torque level for the satellite panel. . . . .	106
88	Mean $I$ values versus percent loss in torque on the bolts (—) and a corresponding hyperbolic tangent curve fit (—) for the satellite panel test results. . . . .	107
89	PnP satellite with close-up views of the L-shaped bracket. . . . .	107
90	Setup and parameters for the PnP satellite IM testing. . . . .	108
91	$I$ values versus percent loss in torque on the bolts for the PnP satellite test results. .	109

## List of Tables

Table		Page
1	Simulation parameters. . . . .	52
2	Comparison of experimental and simulated results. . . . .	54
3	Sideband frequencies. . . . .	90
4	Three-beam, two-bolt results. . . . .	101
5	Four-beam, three-bolt results. . . . .	103
6	Satellite panel results. . . . .	106
7	PnP satellite results. . . . .	109

(This page intentionally left blank)

## 1.0 SUMMARY

Quickly-assembled, on-demand satellites are being developed to meet the needs of responsive space initiatives. The short testing times and rapid assembly procedures associated with these satellites create the need for an efficient method to verify the satellite's structural integrity. In particular, the ability to identify loose bolts within the satellite structure is of interest. In this work, Impact Modulation (IM) is explored as a possible means of detecting loose bolts. First, a simple two-beam, one-bolt assembly is studied to establish guidelines for the implementation of IM. Then, theoretical and analytical models are developed to provide a basis for applying IM to bolted joints. Two analysis methods for identifying loose bolts within a structure are then proposed. These methods are demonstrated on a three-beam, two-bolt structure; a four-beam, three-bolt structure; and a realistic satellite structure.

The results of IM testing on the two-beam, one-bolt assembly showed that the nonlinear response of the system is significantly affected by the underlying linear characteristics of the system, that nonlinear stiffness and damping contribute to the response, that IM is an effective method for differentiating the responses of the bolted structure with different bolt torque levels, and that changes in boundary conditions do not diminish the effectiveness of IM testing. It was demonstrated that the first analysis method was able to identify the presence of loose bolts within increasingly complex structures without the use of historical data by using a dot product analysis to quantify the difference in response amplitudes at the natural frequencies and those at the sideband frequencies across an array of impact locations. The second analysis method successfully tracked changes in bolt torque by comparing the area under the response spectra in the modulation range to a baseline reference.

## 2.0 INTRODUCTION

### 2.1 Motivation and Problem Statement

Today's satellites are often designed to perform specific tasks and can take months, even years, to develop, assemble, test, and launch [1]. New efforts are underway to develop modular satellites that can accomplish a wide range of tasks and can be ready for launch within days of when their need is established [2]. These quickly-built satellites have unique issues due to time constraints and the variability of their geometry which are not typically associated with traditional satellites. One such issue is the ability to quickly assure the structural integrity of the satellite after rapid assembly in order to make certain that it will survive the launch environment.

A satellite's structural integrity is determined by properties such as its geometry, its materials, and the state of its interfaces, including bolted joints. While some properties like the geometry and materials of the satellite are chosen early in the design process and remain unchanged throughout the assembly, the state of other properties, including the state of the bolted joints, can change as the satellite is assembled. These changes can lead to the degradation of a satellite's structural integrity. In the case of bolted joints, the loss of torque on a bolt lessens the structure's stiffness. If enough bolts are under-torqued, the resonant frequencies of the satellite may be lowered beyond the acceptable range determined by the initial design, and the satellite would become more susceptible to damage during launch. Therefore, to help ensure the satellite's structural integrity, a method of diagnosing the condition of the bolted joints of the satellite is required.

The requirements for any method used to assess the bolted joints of the satellites are that the method be insensitive to the geometry of the satellite and that the method be time efficient. Methods that require extensive baseline readings are not applicable because changes in the geometry of the satellite would require the time consuming task of collecting new baseline data. Methods that require extended setup and testing times are also not applicable because the method must be time efficient. One method that meets both criteria is Impact Modulation. Impact Modulation is a non-linear, vibrations-based method which uses a combination of low and high frequency excitations to interrogate structures for damage. Impact Modulation is ideally insensitive to changes in the geometry of the structure and requires minimal iterations to perform.

Impact Modulation (IM) has been shown to be a reliable method to detect damage such as cracks and delamination in structures. This work seeks to extend the use of IM to the assessment of bolted joints. To accomplish this goal, three main objectives were addressed. First, a simple two-beam, one-bolt structure was studied both experimentally and analytically to develop an understanding of how the test parameters associated with IM affect the results. Secondly, analysis methods that identified the presence of a loose bolt within a structure were developed. Finally, the effectiveness of these methods was then demonstrated on several, increasingly complex structures.

## **2.2 Introduction to Impact Modulation**

IM is a method in a class of nondestructive evaluation techniques commonly referred to in the literature as Nonlinear Elastic Wave Spectroscopy methods. These methods have proven to be highly effective in damage identification in materials. As described in [3], the methods are based on the premise that waves traveling through a nonlinear system are distorted and mixed creating harmonics, changes in resonant frequencies, and other phenomena not present in linear systems. In the case of IM, the distortion of waves created by the combination of an impact and a high frequency input, called a probing or carrier signal, is analyzed. The purpose of the impact is to excite the structure's low frequency modes, which in the case of a bolted joint, varies the contact interface and generates nonlinear contact forces. As the high frequency probing wave passes through this nonlinear area, it is modulated by the modal response [4]. In the frequency domain, the results of the interaction between the modal response and the high frequency input are response peaks at frequencies which are linear combinations of the probing signal and the natural frequencies. These peaks are called sidebands. Peaks which occur at frequencies lower than the probing frequency will be referred to as left sidebands. Peaks which occur at frequencies greater than the probing frequency will be referred to as right sidebands.

In practice, IM testing is performed by exciting a structure with both an impact hammer and a high frequency actuator simultaneously. The response of the structure is measured with one or more accelerometers and then converted into the frequency domain for analysis. Sidebands in the frequency data indicate that nonlinearities are present in the system. Figure 1 shows the response spectrum of a structure to excitation by an impact only (a), by an actuator only (b), and by an impact and actuator, i.e. Impact Modulation (c). It is clear that the IM results are not merely a sum of the other two, as evidenced by the appearance of sidebands in the IM data. IM testing provides valuable information about the nonlinearities present in a system. The goal of this work is to use that information to make inferences about the health of the bolted joints within the structure.

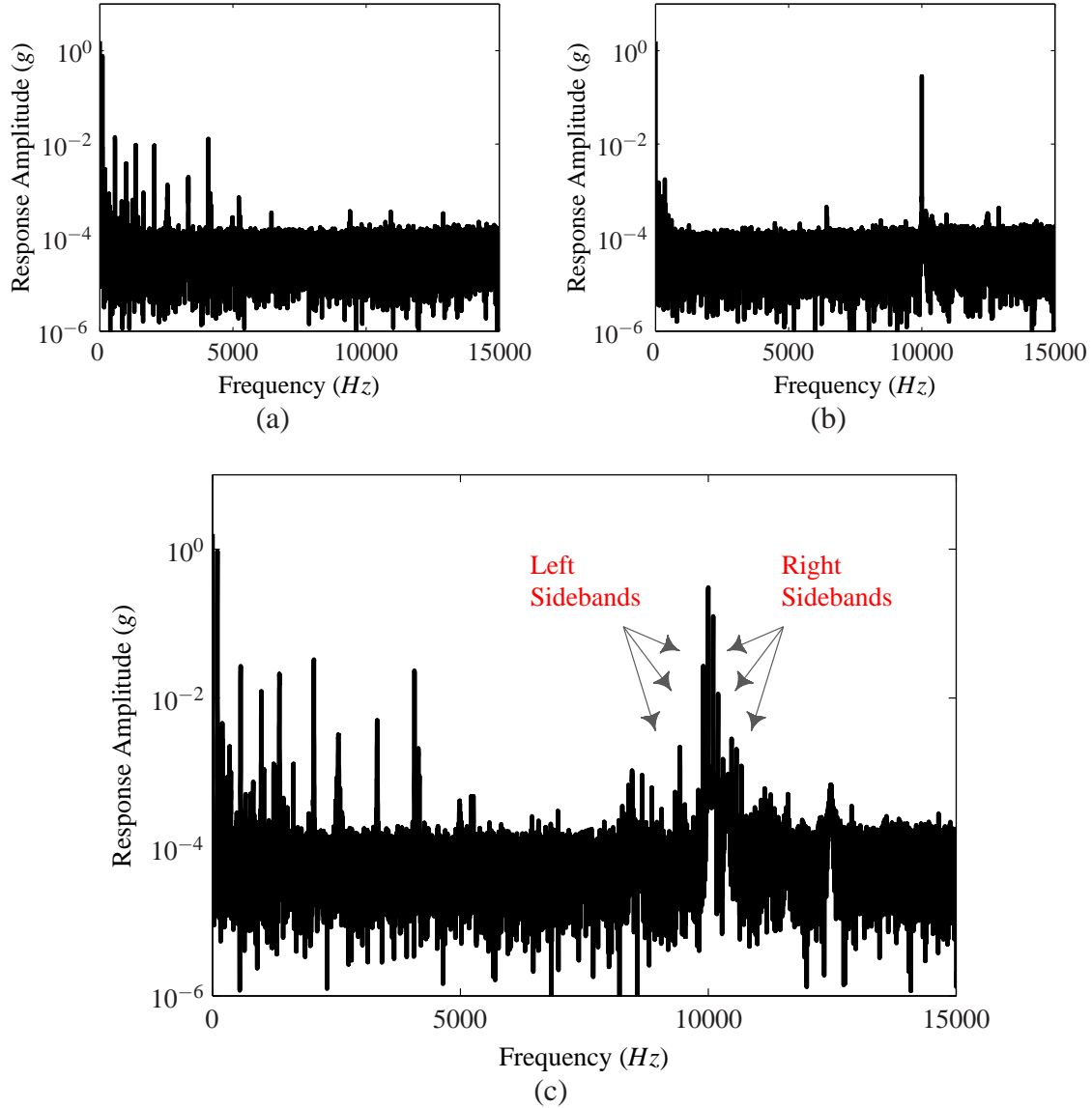


Figure 1: Response spectrum of a two-beam, one-bolt assembly to: (a) an impact only (b) an actuator signal only (c) to both an impact and an actuator signal as used in Impact Modulation (IM) testing.

### 2.3 Literature Review

The following literature review is broken up into three sections. The first addresses the current methods available for identifying and locating loose bolts. While detecting loose bolts on a satellite structure is a recent venture, detecting loose bolts on structures such as bridges and aircraft has been well researched. The second section presents work on the modeling of bolted joints. Models of bolted joints range from simple spring and damper models to complex finite element models that represent each individual bolt thread. The models that best apply to the study of IM are presented here. Finally, although IM has not been applied to bolted joints, it has been proven throughout

the literature to be an effective damage detection method for cracks, delamination, and fatigue in various structures. Some of those applications are highlighted in the third section.

**2.3.1 Current Methods for Detecting Loose Bolts.** There are a number of techniques presented in current literature that are effective for identifying and, in some cases, locating loose bolts within a structure. In the field of civil engineering, techniques have been developed to monitor the state of bolted joints in bridges, reinforced concrete walls, and pipelines. [5] and [6] present methods in which analytical models are developed for the structure of interest. Bolt parameters such as stiffness and damping are identified by matching analytical data with experimental data from a healthy structure. Once the baseline model is defined, changes in the bolt parameters served as a damage index that identifies the loosening of the bolts. This method works well for civil structures because well defined models are available and the structures' conditions can be monitored over time. Guarino, et al. [7] present an acoustic method to analyze the response of a bridge measured by a digital stethoscope to identify loose bolts.

Another group of methods more geared toward aerospace applications uses a database of experimental measurements taken at different damage configurations, typically corresponding to different bolt torque levels, to identify the condition of the bolts within a structure. Clayton, et al. [8] used ultrasonic propagating waves and a prediction algorithm based on minimizing the error between the measured response of the structure and a database of measurements taken at various bolt torque levels. They were able to differentiate between four different bolt torque levels. A similar analysis approach was taken by Olson, et al. [9]. Their database included information that allowed them to identify the location of a loose bolt from an array of four bolts located at the corners of a square aluminum plate. Coelho, et al. [10] were able to identify loose bolts and fatigue damage using optimized sensor locations using a Support Vector Machines algorithm to classify the damage. Finally, Moniz, et al. [11] developed an analysis method based on chaotic amplification of attractor distortion, which allows data from multiple sensors to be synthesized to identify loss of torque in a bolted connection.

In addition to those mentioned above, many wave propagation techniques are also being investigated. Lovell and Pines [12] used wave number scattering analysis to show that wave scattering increases as bolt torque decreases. The method is based on tracking a wave as it travels through the specimen where the bolted joint serves as a scattering mechanism. The implementation of this method requires measuring the response of the specimen at many points in order to track the wave. The use of a laser vibrometer was presented in [13] as an alternative to using a large number of sensors. One disadvantage of this method is that testing times are relatively long. Most recently, Reynolds, et al. [14] compared wave propagation velocities to identify and locate loose bolts within a satellite structure similar to the one that will be studied in this work. Reynolds, et al. compared the signal from a healthy structure to the signal from the same structure with a loosened bolt. They used the time and amplitude of a peak corresponding to the first wave interaction with the loose bolt to construct an ellipse which allowed them to determine the location of the loose bolt.

Several frequency domain methods were also found in the literature. Caccese, et al. [15] used the transmittance function between two response points to quantify changes in nonlinearity in the structure. By comparing transmittance functions of the healthy structure with those of the structure that contained a loose bolt, they were able to detect torque loss as low as 8% of the original value. In [16], Amerini and Meo use a technique similar to IM called Vibro-Acoustic Modulation



(VM). For a two-plate, one-bolt structure, they were able to detect torque loss by measuring the difference in the amplitude of response at the actuator frequency and the average amplitude of the first sidebands. To quantify the torque loss, they fit a hyperbolic tangent curve to the data. Amerini and Meo's work is the most similar to the work that will be presented in the following chapters.

Although rare, there are a few methods presented in the literature that do not rely on baseline data or on an analytical model. Milanese, et al. [17] developed a method which looked for frequency content in the measured strain response of a test specimen above the maximum excitation frequency to indicate that the bolt was loose. A damage index was developed based on probabilistic analysis that was proven effective in identifying loose bolts. In the method presented by Nichols, et al. [18], surrogate baseline data was generated from the response of a structure by using the iterative amplitude adjusted Fourier transform method (IAAFT). IAAFT operates under the assumption that a healthy structure is linear and a damaged structure is nonlinear. The linear part of the response is extracted from the full data and compared to the full data itself. The level of nonlinearity present in the response is used as an indicator of the presence of loose bolts within the system.

With the exception of [17] and [18], the current methods available for diagnosing bolted joints are heavily reliant on either baseline data or an experimentally validated analytical model. These requirements cannot be met for the application to rapidly-assembled satellites. The fact that IM-based methods can potentially be effective without relying on baseline data or analytical models was a contributing reason that IM was chosen for this work.

**2.3.2 Bolt Models.** The topic of modeling bolted joints is a well researched field. Several comprehensive reviews are available that track the development of the state of the art methods throughout the last half century. Ungar [19] detailed work prior to 1970 which focused on how energy is dissipated in a bolted joint. At that time, it was well understood that the damping in so-called "built-up" structures, i.e. structures with bolted joints, is far greater than the damping in a similar continuous system. Ferri's review [20] includes a section on bolted joints which details the development of the understanding of micro- and macro-slip. These terms are used to describe the stick-slip phenomena that occur at the joint interface, and they indicate the nonlinear nature of bolted joints. Gaul and Nitsche [21] reviewed how these phenomena were being modeled. They sorted current works into phenomenological models, which are based on experimental observations, and constitutive models, which are based on the physics at the joint interface. The models they presented included the Jenkins element, the LuGre model, and the Valanis model. Segalman [22] took a similar approach but also included a description of the Iwan model and discussed current solution techniques. Finally, Ibrahim and Pettit [23] highlighted the uncertainties associated with bolted joints in addition to presenting a thorough review of current and past works on all aspects of bolted joint modeling and parameter identification.

Much of the current research on modeling bolted joints is focused on parameter identification for various nonlinear friction models. These works focus on describing the nonlinear energy dissipation due to shear loading with reduced order models typically consisting of a combination of springs and sliders. [24] contains detailed descriptions of current models including the Iwan, Valanis, and Bouc-Wen. The most common approach to identifying the parameters in these models is to perform experimental tests on an isolated bolted connection and then use the data from those tests to tune the model parameters. In [25], Gaul and Lenz used this approach to tune the

parameters of a Valanis model of a lap joint. Then, they incorporated Valanis elements into a finite element model of a simple structure and compared experimental results. The Valanis model was shown to accurately capture the micro- and macro-slip phenomena that are known to occur in bolted connections. Similarly, Oldfield, et al. [26] showed the accuracy of the Jenkins element and the Bouc-Wen model in capturing the nonlinear nature of bolted lap joints. Song, et al. [27] and Hartwigsen, et al. [28] have proven the validity of using Iwan beam elements to model bolted joints. As with the previous works, they used experimental data to tune the parameters of their models. Based on these works, other researchers have continued to study the effectiveness of these damping models in capturing the dynamics of bolted joints. For example, Ouyang, et al. [29] observed experimentally that the response of an isolated bolted joint contains more super-harmonics and that the hysteresis loop deviates further from an elliptical shape as bolt torque is decreased and excitation amplitude is increased. They then showed that a model of the bolted joint with a Jenkins element representing the friction at the interface is able to represent these phenomena. In [30], Mayer and Gaul developed a contact element for use in finite element analysis to model bolted joints. This element used the Masing element to model the friction and allowed for nonlinear constitutive contact behavior in both the normal and tangential directions.

While the works described above have focused mainly on modeling the damping associated with the shearing of a bolted joint, studies on the effects of bolted joints in the normal direction have also been conducted. In [31], the joint in a two-beam, one-bolt assembly was modeled by a linear spring and an external, nonlinear force applied normal to the beam. A method for identifying the coefficients for the stiffness in the springs and for identifying the nonlinear force from correlated experimental data was presented. In [32], Ma, et al. developed a method using laser vibrometry to measure the transverse response of a beam with and without a bolted joint. It was shown that by comparing the responses, lumped spring and damping parameters can be extracted. Bowden and Dugundji [33] and Esteben and Rogers [34] also identified stiffness and damping parameters in a beam model, but unlike Ma's work, they allowed for a nonlinear stiffness. Ahmadian and Jalali [35] took a similar approach, modeling the bolted joint with a cubic translational spring and linear rotational springs and dampers. By comparing analytical results with experimental data, the spring and damping coefficients were identified. Later in [36], Jalali, et al. refined the model of the bolted joint to include displacement-dependent damping. In that study, it was shown that as the pre-load on the bolt within a bolted interface is increased, the nonlinearity of the interface decreases. Most recently, Jalali [37] developed a model that accounts for both tangential direction micro-slip and normal direction micro-impacts. Experimental data was used to validate the model. Based on these models that describe the dynamics of a bolted joint in the normal direction, Ahmadian and Jalali [38] developed a "generic" element for use in finite element models that captures the dynamics of a bolted joint. Generic mass, stiffness, and damping parameters associated with the bolted joint were presented. Experimental data was required to identify the parameters. Finally, Barhorst [39] took an analytical approach to describing the motions in a bolted joint by formulating equations of motion that model impact dynamics and friction forces that occur in a loose joint.

Other research has focused on characterizing the effects of bolted joints on a structure as a whole. Walker, et al. [40] performed experimental testing to identify the parameters which most effect the damping of a structure with bolted joints. They found that lower bolt torque levels led to higher loss factors, but larger overlap area led to lower loss factors due to the increase in stiffness at the joint. They also noted that different modes of the structure are affected differently by changes in bolt torque depending on the location of the bolted joint. Nassar, et al. [41] measured the de-

flections of a bolted lap joint to gain an understanding of the mechanical behavior of the joint. The results showed a definite nonlinear trend in the force-deflection curves. Hartwigsen summarizes the most significant effects a bolted joint has on a structure as being an overall reduction in stiffness of the structure, an increase in damping, slightly distorted mode shapes, and energy dissipation in a power-law relation with respect to the applied force. These effects are consistently mentioned throughout current literature.

**2.3.3 Applications of Impact Modulation.** As mentioned previously, no work was found in the literature on applying IM to bolted joints. The main application for IM is to detect cracks in a specimen. IM has been applied successfully to glass [42], sandstone [3], and steel [4] specimens proving its robustness across materials with different properties. IM has been shown to be effective on more complex structures as well. [43] applied IM to steel pipes to identify the presence of cracks, and [44] detected cracks in a carbon filament wound canister. In [45], a similar method called Vibro-Acoustic Modulation (VM) was used to detect delamination in a composite plate. The difference between VM and IM is that VM uses a single low frequency excitation instead of an impact. That application showed the method's effectiveness for specimens with complex material properties. In [46], Zaitsev and Sas optimized the testing parameters of VM as applied to a cracked aluminum plate and found that, with certain parameter choices, the amplitudes of the sidebands in the response spectrum exceeded the amplitude of response at the probing frequency. Finally, as detailed earlier, Amerini and Meo [16] used VM to interrogate bolted joints in a simple two-plate, one-bolt structure. These are a sampling of the many applications of IM for damage detection presented in literature.

## 2.4 Objectives

The objectives of this work are to:

1. Develop a theoretical understanding of Impact Modulation as it applies to a system with a bolted joint.
2. Develop analytical models which can simulate the response of structures which contain bolted joints to Impact Modulation.
3. Experimentally verify that Impact Modulation is an effective method for differentiating the response of systems which contain bolts having different torque levels.
4. Develop a damage index which can identify the presence of loose bolts in a structure without a priori knowledge.
5. Demonstrate the effectiveness of the damage index on a realistic satellite structure.

### 3.0 METHODS, ASSUMPTIONS, AND PROCEDURES

#### 3.1 Implementing Impact Modulation: Experimental Development and Sensitivity Analysis

Impact Modulation (IM) has not previously been used to identify loose bolts in a structure. Therefore, in order to substantiate the effectiveness of using IM to interrogate bolted joints, it must be shown experimentally that IM can distinguish between the responses of a structure that are measured when the bolts are at different torque levels. In order to design an optimal experiment which accentuates the differences in the response spectra due to changes in bolt torque, the effect of variation in other test parameters must be well understood. In this chapter, results from a sensitivity study are presented that describe how changing certain parameters affect the results of IM testing on a simple two-beam, one-bolt assembly. Findings from this sensitivity study will be applied to designing an optimum experimental setup which can be used to detect loose bolts without a priori knowledge.

In addition to the level of torque on the bolt, the test parameters that must be selected when implementing IM testing include sensor location and orientation; probing force input location, orientation, amplitude and frequency; impact location, orientation, amplitude, and frequency range; and the boundary conditions of the test specimen. Although other researchers have implemented IM testing for other applications, few of them addressed the effects of these test parameters on the test results. Haroon and Adams [47] noted qualitatively that variability in impact level affected IM results during testing for cracks on a slender beam. Using Vibro-Acoustic Modulation (VM), a technique similar to IM in which the impact is replaced with a continuous excitation, Courtney, et al. [48] did preliminary work which showed that VM is effective in detecting fatigue cracks in engineering components despite changes in actuator location and boundary conditions. Polimeno and Meo [49] and Duffour, et al. [50] also noted the dependence of VM results on the boundary conditions of their test rigs. Finally, Yoder and Adams [51] investigated the dependence of the sideband amplitudes that result from VM testing on the probing force frequency and identified the modes that most contribute to the operating deflection shape at the sideband frequencies. The following work aims to comprehensively study the effects of test parameters on the IM results in order to optimize the test procedure for application to loose bolt detection.

**3.1.1 Experimental Setup and Test Procedure.** Testing was performed on a two-beam, one-bolt specimen. (See Figure 2.) This assembly was chosen because of its simple geometry and low number of components. Each beam was made of Al 6061-T6 and measured  $11\frac{3}{4}$  in. x  $\frac{3}{4}$  in. x  $\frac{1}{4}$  in. The beams had a 1 inch lap joint fastened by a 10-32 bolt and a standard nut with no washers. A CDI 401SM torque screw driver was used throughout this work to tighten the bolts to a desired torque. The torque values used will be specified later in the description of each experiment. A PI P-010.10P piezo stack actuator was used to generate a high frequency excitation and a PCB 086C01 impact hammer was used to excite the low frequency modes of the structure. PCB accelerometers were used to measure the response of the structure. The type of accelerometer model that was used varied between experiments and will be identified below in the description of each experiment. Although most of the sensor models that were used were triaxial accelerometers, only the transverse response (perpendicular to the top face of the beam) was analyzed. A PCB 209C01 force sensor was used when it was necessary to measure the actuator force. An Agilent E8408A VXI data acquisition system was used to collect time histories from the sensors and the

impact hammer as well as to drive the actuator. All post-processing of the data was performed in MATLAB.

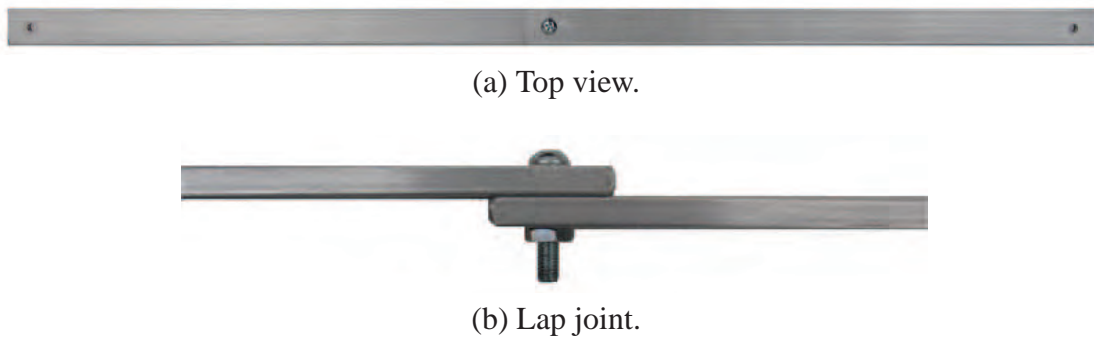


Figure 2: Two-beam experimental setup.

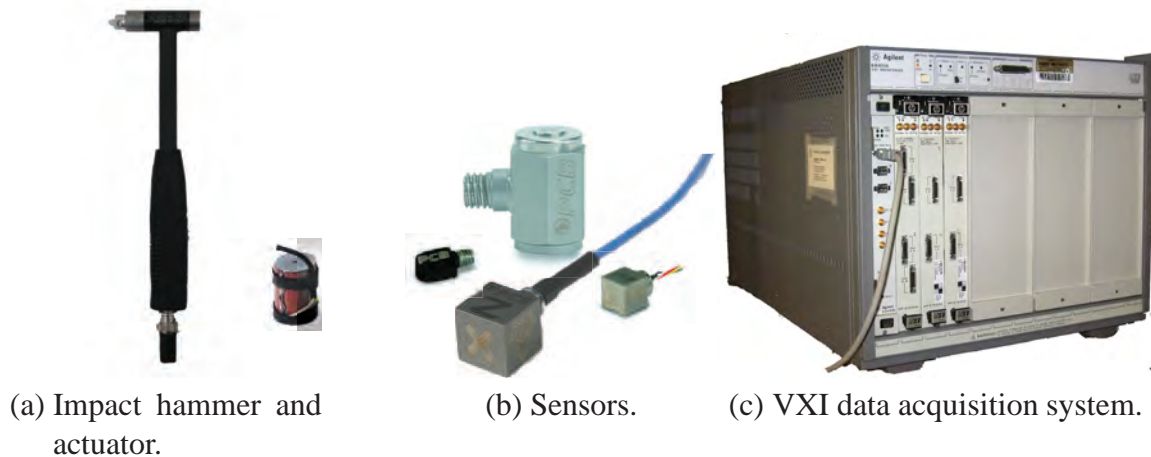


Figure 3: Experimental equipment.

The procedure for the IM testing presented in this chapter was as follows:

1. Testing parameters (sensor location, impact location, actuator frequency, etc.) were chosen. Note that these parameters were varied throughout the different tests presented here and will be specified in detail as the results are discussed.
2. Data was collected.
  - A) The structure was struck with the impact hammer while simultaneously being excited with the actuator. This combination of excitations was repeated three to five times so that the data could be averaged.
  - B) The response of the structure was measured with accelerometers.
  - C) The forces were measured by force sensors.

3. The time data collected during Step 2 was averaged and windowed using a Hanning window. Then the Discrete Fourier Transform algorithm in MATLAB was used to convert the time series data to frequency spectra.
4. The first four natural frequencies and the magnitude (or imaginary part, depending on the intent of the analysis) of the response at those four frequencies were identified and recorded.
5. The magnitude (or imaginary part) and frequency of the first four right and left sidebands were identified and recorded.

Following this procedure, a sensitivity study was completed using IM testing to investigate the effects of changing the following test parameters on the response:

1. Impact amplitude
2. Impact location
3. Sensor location
4. Actuator (probing force) amplitude
5. Actuator (probing force) frequency
6. Bolt torque
7. Boundary Conditions

The sensitivity of the amplitude of the sidebands to changes in test parameters was of particular interest. The results of the study are presented in the following section.

### **3.1.2 Sensitivity Study.**

#### **Impact Amplitude**

One of the more difficult parameters to control when performing IM is the amplitude of the impact. It is possible to set upper and lower bounds on the amplitude of the impact based on the measurement of the impact force from the impact hammer. However, the tighter the range of these bounds, the more time consuming the data collection process becomes, because it takes more attempts to produce an impact at an acceptable amplitude. One solution to this problem is to broaden the range of acceptable impact amplitudes so that more impacts fall into that range. However, there are likely to be consequences to letting the amplitude of the impact vary over such a wide range, especially since the structure is assumed to exhibit nonlinearity due to the bolted interface. The objective of this section is to identify the consequences of allowing the impact amplitude to vary over a wide range.

According to the testing procedure outlined in the previous section, the first step in IM testing is to choose the testing parameters. Parameters were initially chosen based on previous experience



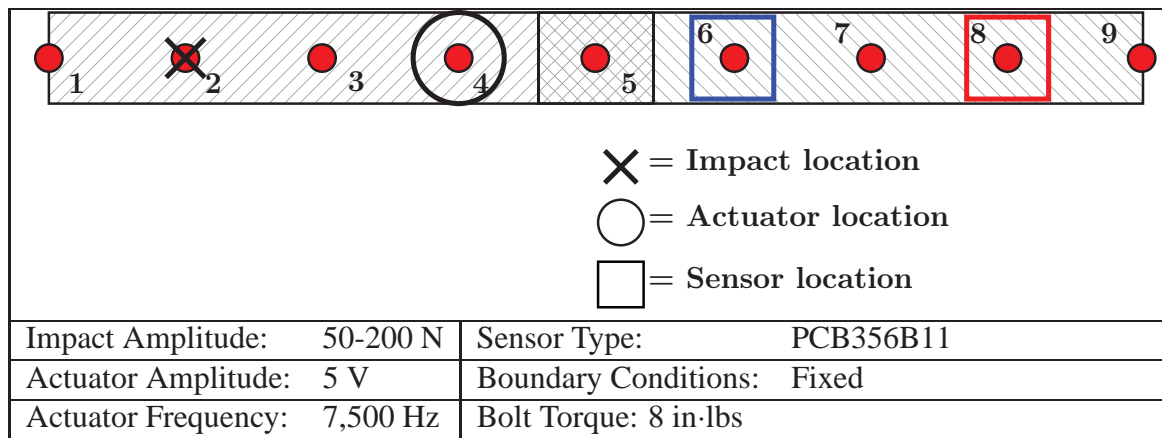


Figure 4: Setup and parameters for impact amplitude testing. The numbered, red dots represent reference nodes.



Figure 5: Two-beam, one-bolt setup with fixed boundary conditions.

and were then refined throughout the sensitivity study. For the first set of tests, which studied the effects of varying the impact amplitude, the impact location, actuator location, and other test parameters were selected as outlined in Figure 4. A bolt torque of 8 in·lbs was chosen because it is a fairly low torque level at which distinct sidebands were evident in the response data. The actuator amplitude (5 V) was chosen because it was in the middle of its range (1-10 V). Fixed boundary conditions and sensor location were chosen arbitrarily. Fixed boundary conditions were

enforced by bolting the two-beam assembly to two 90 lb steel blocks with a torque of 36 in-lbs. (See Figure 5.)

After the test parameters were chosen, IM was repeated for a range of impact amplitudes. One hundred fifty IM tests were performed with one impact per test (i.e. no averaging). The amplitude of the impacts were between 50 and 200 N. The response of the system was measured with two sensors, as shown in Figure 4. Data from the sensor at node 6 was analyzed. Results from the sensor at node 8 were similar and are not presented here. A typical response spectrum is shown in Figure 6a. The low frequency spectrum was used to identify the natural frequencies of interest. As shown in Figure 6b, the first four natural frequencies are: 98 Hz, 366 Hz, 576 Hz, 958 Hz. The high frequency spectrum shows the sidebands which occur at frequencies equal to the actuator frequency (7,500 Hz) plus and minus each natural frequency: 7,402 and 7,598 Hz for mode 1; 7,134 and 7,866 Hz for mode 2; 6,924 and 8,076 Hz for mode 3; and 6,542 and 8,458 Hz for mode 4. Some of these sidebands are more visible than others as seen in Figure 6c. Recall that the sidebands which occur at frequencies lower than the actuator frequency will be referred to as left sidebands and sidebands which occur at frequencies higher than the actuator frequency will be called right sidebands.

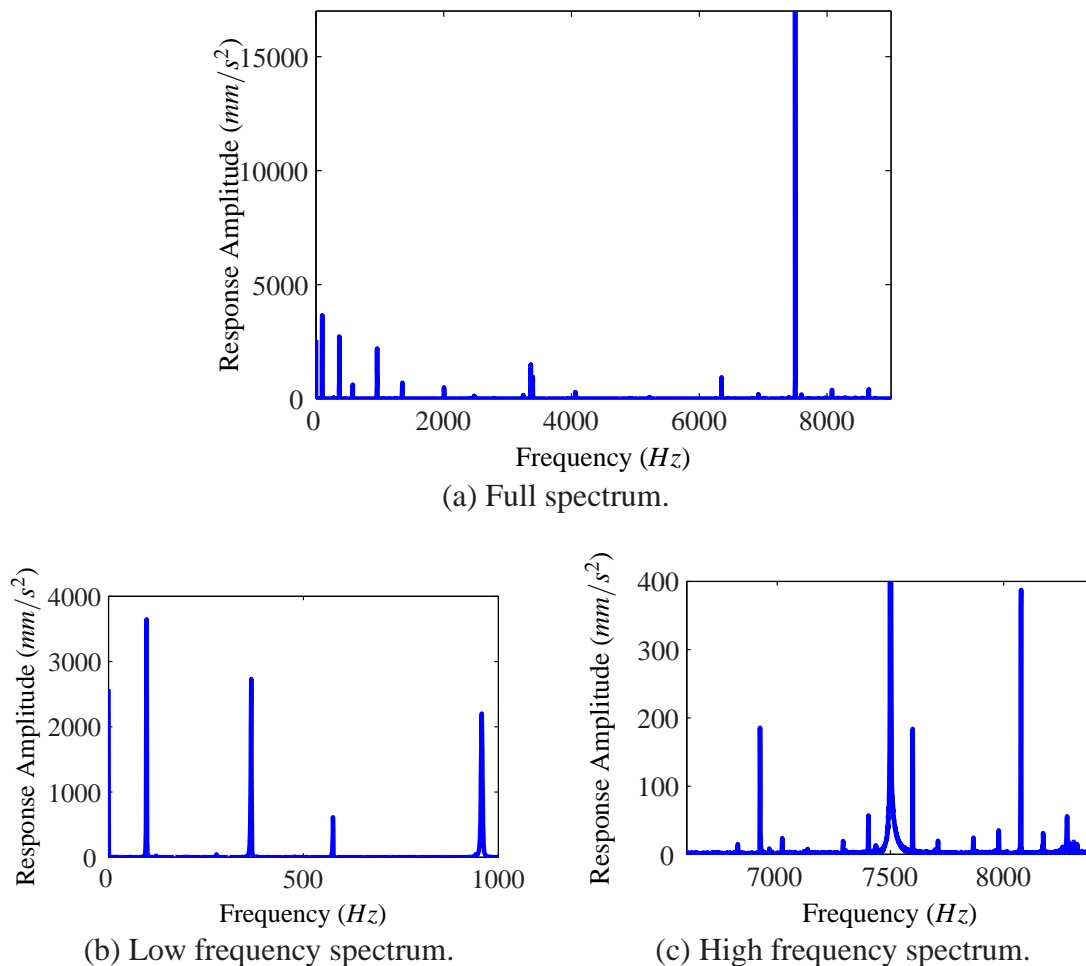


Figure 6: Response spectra from an IM test from impact amplitude testing.



In order to determine the effect of varying the impact amplitude, the magnitude of the first four left and right sidebands for each of the 150 impacts were plotted versus impact amplitude. For comparison, the amplitude of response at each of the first four natural frequencies was plotted, as well. In each plot, the response data was normalized by the magnitude of the response to the lowest amplitude impact, and each impact force amplitude was normalized by the smallest impact force amplitude. Figure 7 shows that an increase in the impact amplitude leads to an increase in the amplitudes of the sidebands. In general, the growth of the modal response and the sidebands is linear. A least-squares based linear curve fit is shown for each plot as a green line. Mode 2 shows a flattening out of the response at higher amplitudes, and the right sideband response appears to mirror that trend. The sidebands in mode 4 also show nonlinear trends. It is likely that the higher amplitude impacts are more strongly exercising the nonlinearities in the joint for these cases.

In every case, it is clear that the amplitude of the impact has a direct effect on the amplitude of the sidebands. Thus, it can be concluded that when implementing IM as a method for detecting loose bolts, the impact amplitude must be controlled. Two methods for controlling the impact amplitude are to maintain a narrow range of acceptable amplitudes and to normalize the response to account for differences in the impact amplitudes between tests. The ability to maintain a narrow range of acceptable impact amplitudes is based on the physical capabilities of the investigator as some people are better at producing consistent impacts with the impact hammer than others. A balance between keeping the amplitude range narrow to avoid too much variation and keeping the range broad enough to ensure the test can be completed in a timely manner must be achieved. The second method of normalizing the data to account for variation in impact amplitudes is also effective. It was observed from the data shown in Figure 7 that the modal responses grow at approximately the same rate as the sideband responses. Therefore, the sideband response can be scaled by the modal response as a means of accounting for variation in the impact amplitude. Figure 8 shows the result of normalizing the sideband amplitudes by the corresponding modal response. The green line indicates a one-to-one ratio of modal response growth to sideband growth, which is the ideal case when viewing the normalized, scaled data. In all cases, the normalization by the modal vibration response is effective at minimizing the variation in sideband amplitudes caused by variation in the impact amplitudes.

## **Impact Location**

As opposed to impact amplitude, the control of the impact location is easily accomplished. However, the initial choice of an impact location is not a trivial matter. Therefore, to investigate the effect of the impact location on the response of the structure to IM testing, IM testing was performed using nine different impact locations, as shown in Figure 9. Three averages were taken at each location, and the imaginary part of the response at the natural frequencies and sideband frequencies was plotted as a function of impact location, as seen in Figure 10. Each data set was scaled by its largest value. The plot for the natural frequencies reflect the operating deflection shape, which is an approximation of the mode shape. The plots for the sideband responses are not operating deflection shapes because reciprocity cannot be assumed since the formation of sidebands is a nonlinear phenomenon. The operating shapes of the sidebands will be discussed again later in the section on sensor location.

The sidebands corresponding to modes 2 through 4 show good agreement with the modal deflection shapes. From modal analysis theory, it is known that the location at which the beam is

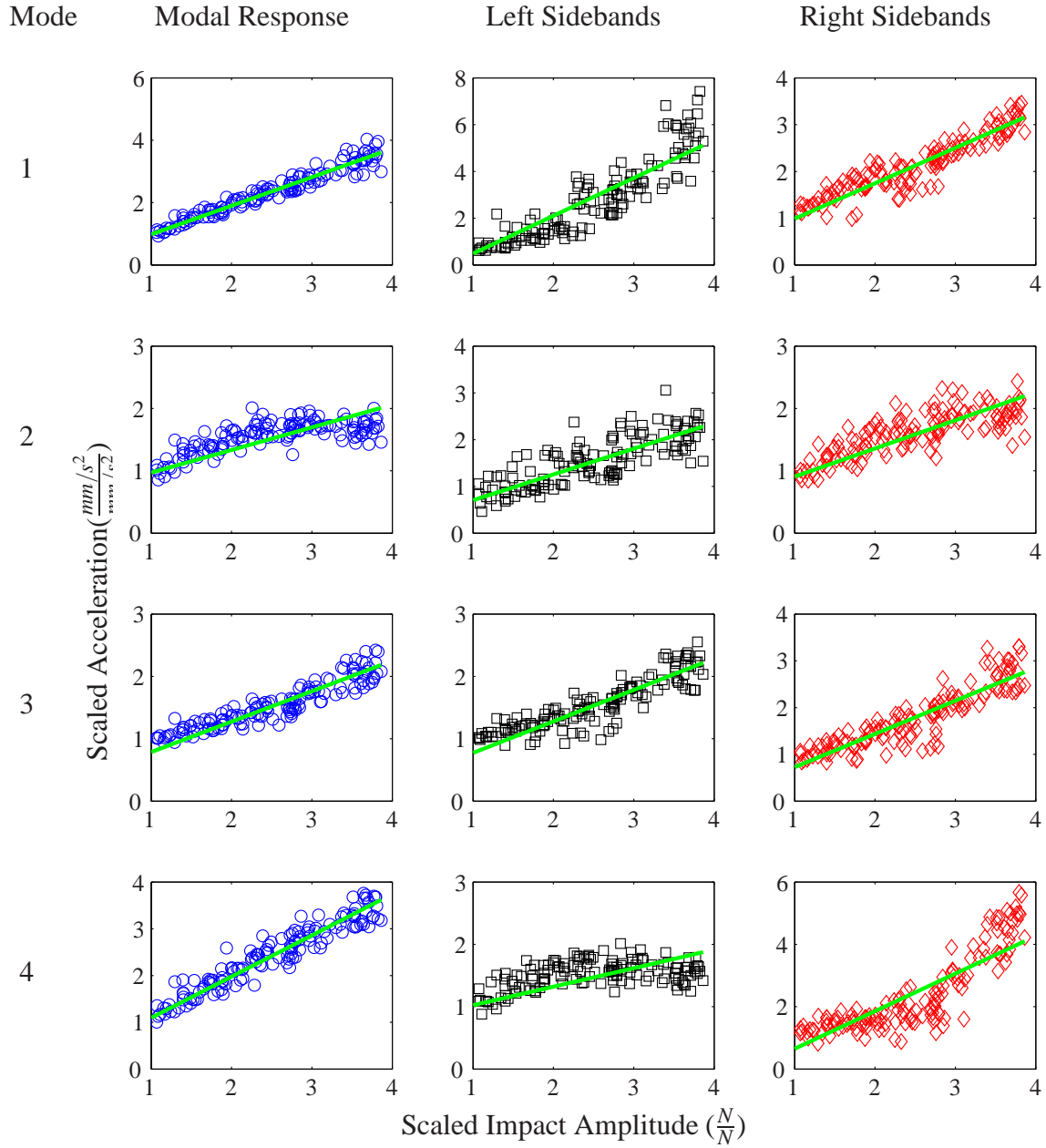


Figure 7: Scaled amplitudes of modal response ( $\circ$ ), left sidebands ( $\square$ ) and right sidebands ( $\diamond$ ) versus scaled impact amplitude from IM testing. Green lines ( $\text{—}$ ) indicate a least-squares linear curve fit of each set of data.

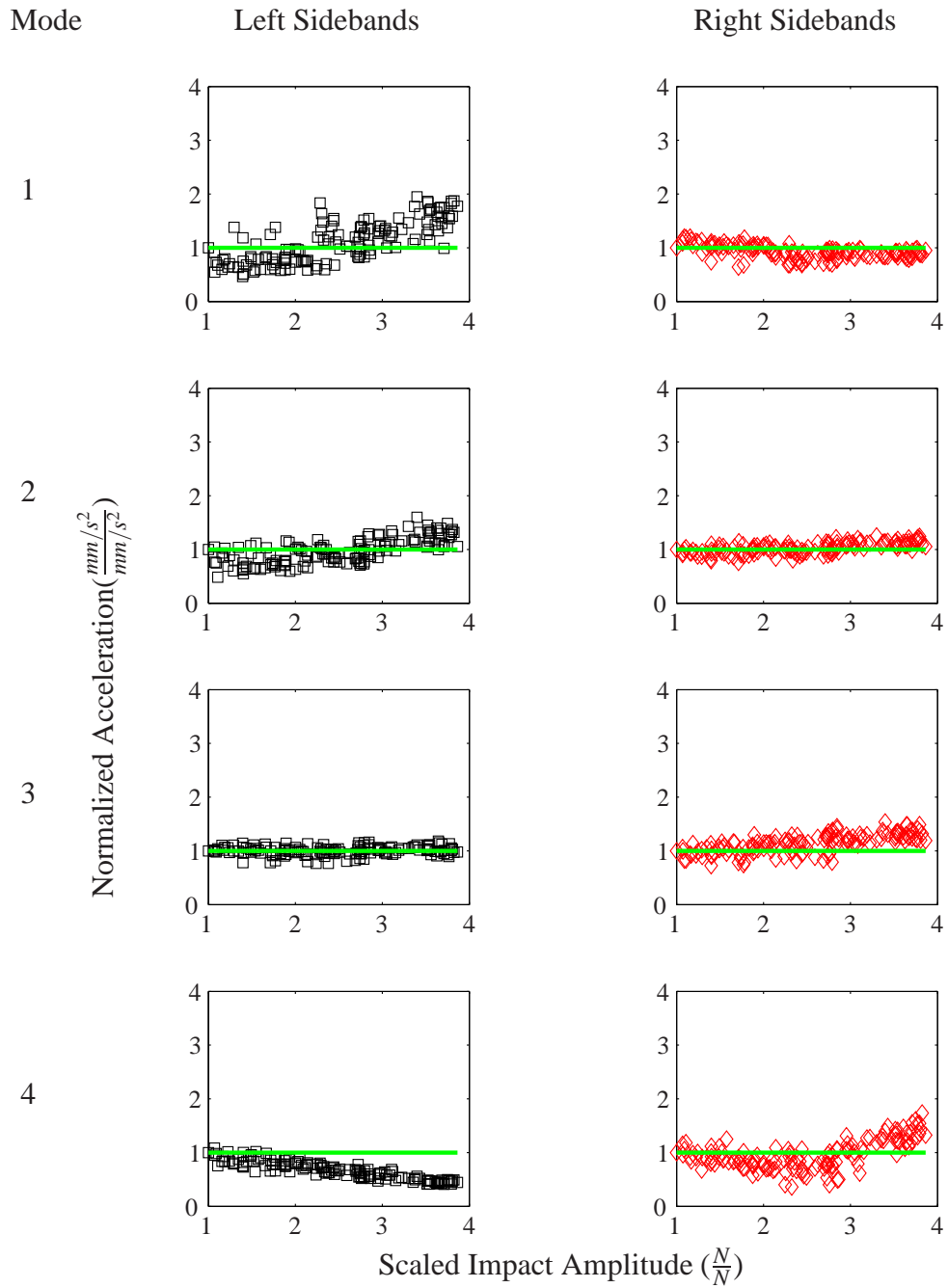


Figure 8: Normalized response amplitude versus scaled impact amplitude from IM testing for left ( $\square$ ) and right ( $\diamond$ ) sidebands. The green line ( $\text{---}$ ) indicates the ideal case.

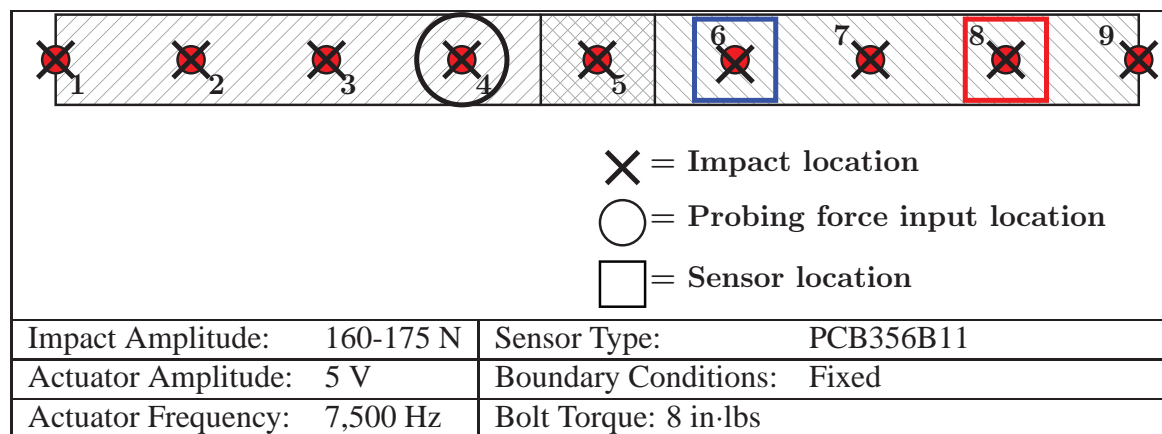


Figure 9: Setup and parameters for impact location testing.

impacted affects its response because certain impact locations excite the beam more effectively in certain modes of vibration than other locations. An impact at an anti-node of a modal deflection shape will certainly yield different results than an impact at a node of that mode shape. Similarly, the amplitudes of the sidebands produced from IM testing are affected by how well the impact was able to excite the corresponding modes of the structure. The more excited a certain mode is as a result of the impact, the greater the amplitude of the sideband will be. The sidebands corresponding to mode 1 seem to show less correlation with the modal deflection shape than the other modes. The deflections corresponding to impact locations 4, 5, and 6 are lower than expected. A possible explanation for these dips in the response is that the response at the first natural frequency also shows the same trend, but to a lesser extent. It can be observed from the first modal response plot in Figure 10 that the deflections corresponding to impact locations 4, 5 and 6 appear smaller than expected when compared to the first theoretical mode shape for a continuous beam.

In the previous section, a method for normalization was developed to account for differences in impact amplitude. No such normalization process will be developed for variation in impact location because, as mentioned earlier, impact location is easily controlled. It is important to note, however, that two data sets resulting from IM testing with different impact locations should not be compared without considering the underlying linear properties of the system that will affect the data. For all subsequent tests in the sensitivity study, the impact location will be held constant. Node 2 was chosen because none of the first four modes have a node at that point and because initial testing showed that the quality of impacts (based on range of frequency excited before roll-off, etc.) made at this point was consistently high.

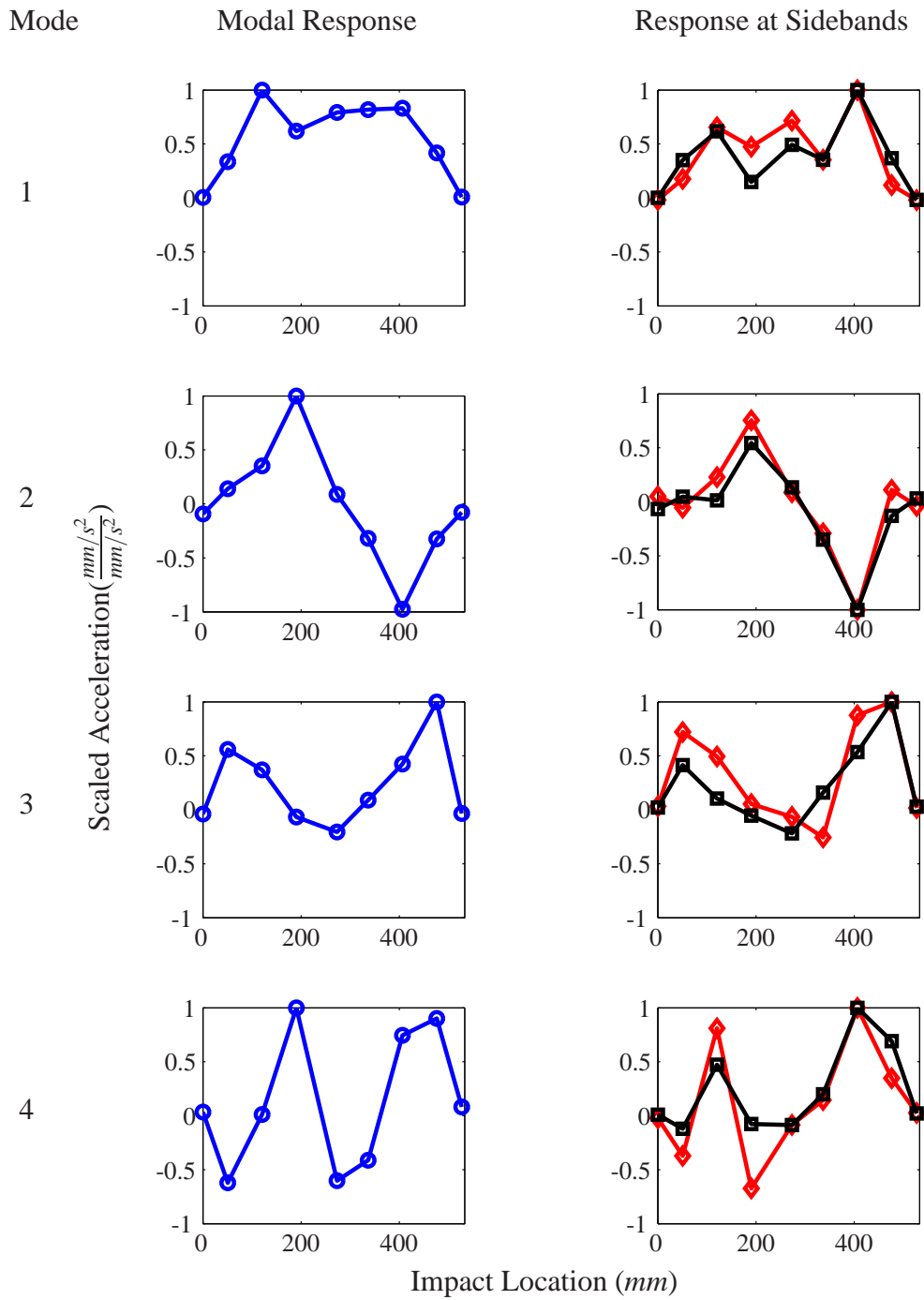


Figure 10: Scaled imaginary part of the response versus impact location as measured along the beam from IM testing for the modal response (—) and for the left (—) and right (—) sidebands.

## Sensor Location

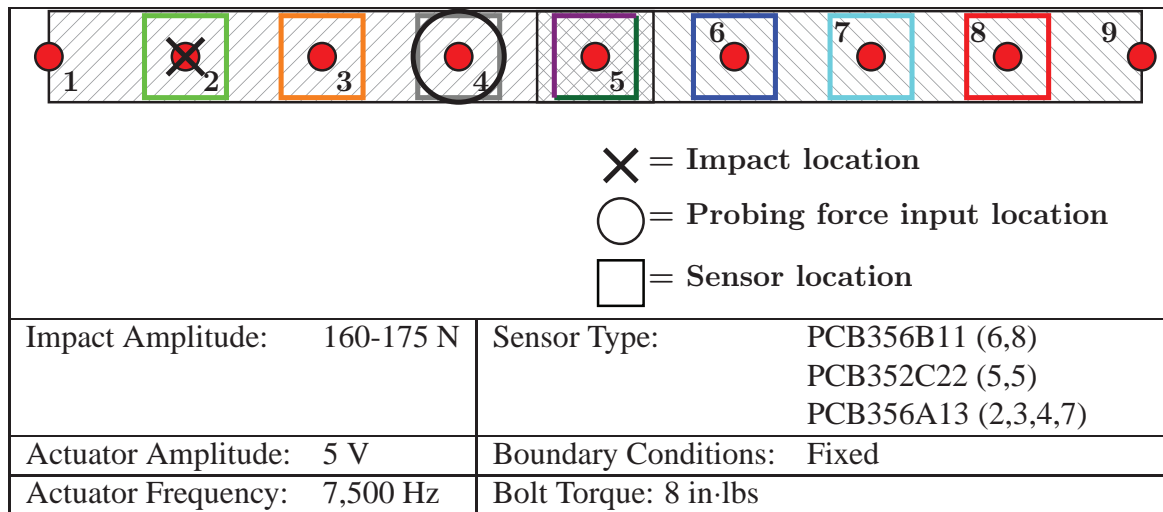


Figure 11: Setup and parameters for sensor location testing.



Figure 12: Two-beam, one-bolt setup with sensor array.

In the previous tests, two arbitrarily placed sensors were used to collect data. In an effort to understand how sensor placement affects IM results, the two-beam specimen was equipped

with an array of eight sensors at locations shown in Figure 11 and Figure 12. Two sensors were mounted at node 5, one sensor was mounted on the top side at the end of the first beam and one sensor was mounted on the bottom side on the second beam. IM testing consisting of five averages was performed, and the imaginary part of the response at each natural frequency and sideband frequency was plotted as a function of sensor location. It was predicted that the sideband shapes would reflect their corresponding modal deflection shapes as was the case with the impact location test, but as seen in Figure 13, that prediction was not correct. Instead, what is likely being shown in the plots of the sideband response versus sensor location is the operating deflection shape at each sideband frequency. Because these are high frequency deflection shapes, more sensors would be required to produce a smoother, more continuous plot of the shapes. In the next chapter, finite element modeling will be used to determine the mode shapes that contribute to these deflection shapes. From the experimental data presented here, it is difficult to draw any conclusions about the best place to position the sensors. In subsequent chapters, a sensor array will be used as a means to detect a loose bolt within a structure. The use of a sensor array diminishes the importance of sensor placement.

### **Actuator Amplitude**

The effect of actuator amplitude on IM results was explored by performing IM testing with actuator amplitudes ranging from one to nine volts in one volt increments and with five averages taken at each amplitude. Measurements from a force sensor mounted to the actuator showed that these voltages produce forces that range from approximately .02 N to .18 N in .02 N increments. Other test parameters were kept constant and are listed in Figure 14. The amplitude of the left and right sidebands, when scaled by the amplitude from the smallest actuator force, for the first four modes are plotted against the amplitude of the force produced by the actuator, when scaled by the smallest actuator force, in Figure 15. The response at the actuator frequency (7500 Hz) is also shown. Previously, it was shown that the growth in the response at the sideband frequencies mirrored the growth of the response at the natural frequencies as the impact amplitude was increased. Here a similar trend is seen with respect to the response at the actuator frequency. Both the response at the sideband frequencies and the response at the actuator frequency grow according to the same trend. Unlike the linear trend seen with increasing impact amplitudes, the growth of the sideband amplitudes and the magnitude of response at the actuator frequency is nonlinear with respect to actuator amplitude. This nonlinear trend manifests only during IM testing. Response data collected for increasing actuator amplitudes and no impact showed a linear trend. Therefore, it is clear that the dynamics that result from the impact excitation affect the response at the actuator frequency. In addition, these results may indicate that there is an ideal ratio between response amplitude at the natural frequency and the response amplitude at the probing force frequency, which would explain the sharp drop-off in sideband amplitude at the highest actuator amplitude.

As will be discussed in the next chapter on model development, theory suggests that the amplitude of the sidebands is proportional to the amplitude of response at the actuator frequency. In addition, researchers such as Johnson, et al. [52] and Donskoy, et al. [4] have shown that for cracked specimens, the normalization of the sideband amplitudes by the amplitude of response at the actuator frequency produces a constant provided that the impact amplitudes and level of damage in the specimen remain constant. To explore the effectiveness of this normalization process for specimens with bolted joints, the sideband amplitudes shown in Figure 15 were divided by the

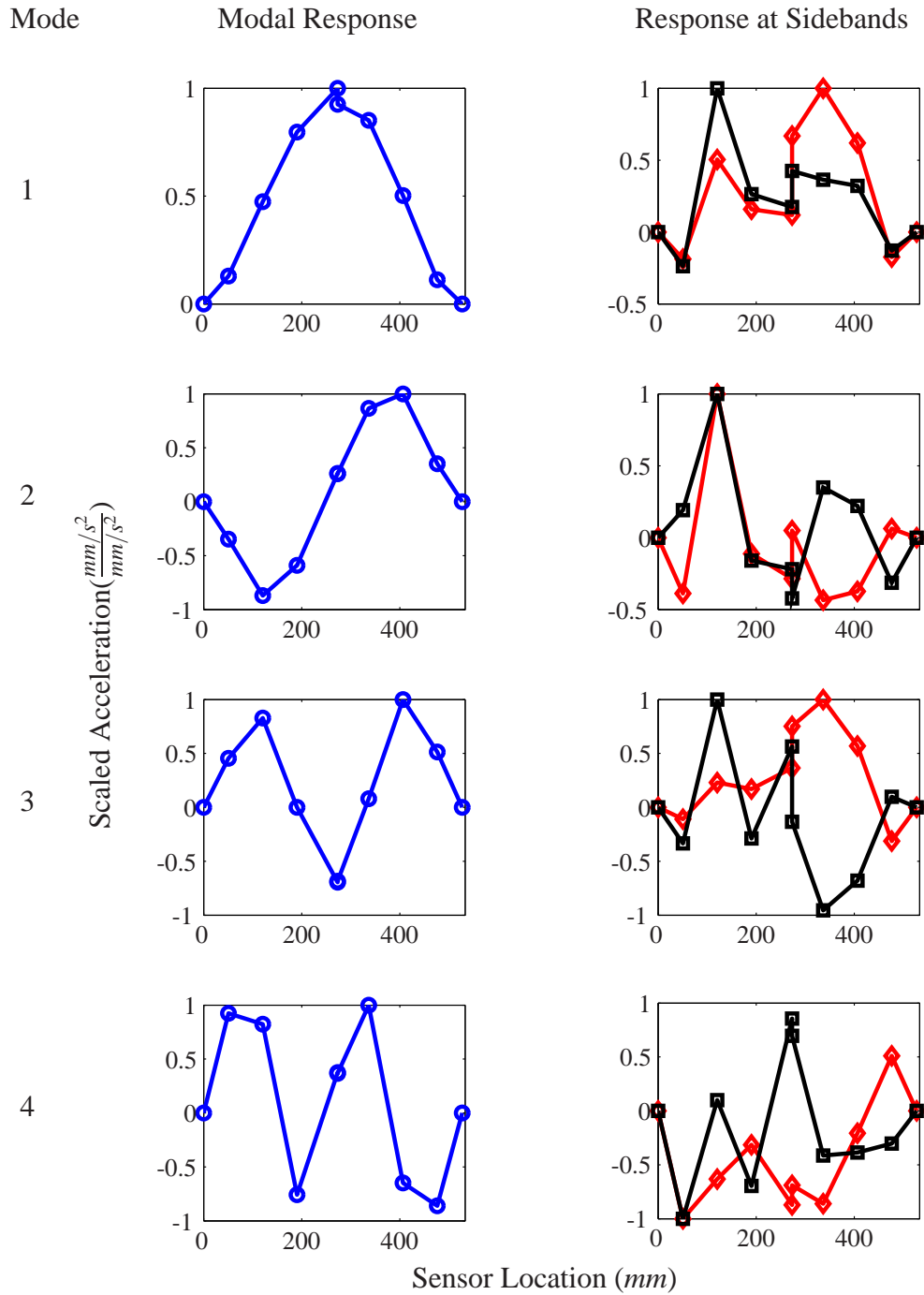


Figure 13: Scaled imaginary part of the response versus sensor location as measured along the beam from IM testing for the modal response (—) and for the left (—) and right (—) sidebands.



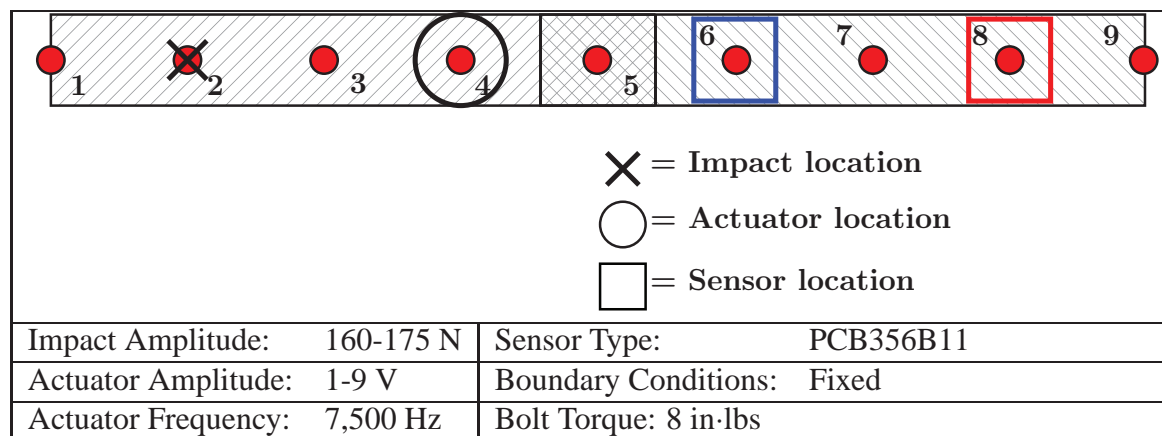


Figure 14: Setup and parameters for actuator amplitude testing.

amplitude of response at the actuator frequency seen in the same figure in blue. The results of this normalization are seen in Figure 16 and can be characterized as inconsistent. It is important to note that the researchers who found success using the response amplitude at the actuator frequency as a normalization parameter saw a linear trend in the growth of the sidebands with respect to actuator amplitude. The fact that bolted joints do not exhibit the same linear trend implies that the nonlinear interactions taking place within the bolted joint are of a different nature than those nonlinear interactions which take place in a cracked specimen. It may be unreasonable to expect the same analysis techniques to apply to both cracked specimens and bolted joints. To avoid inconsistencies associated with changes in the actuator amplitude, all future tests will use a set actuator amplitude.

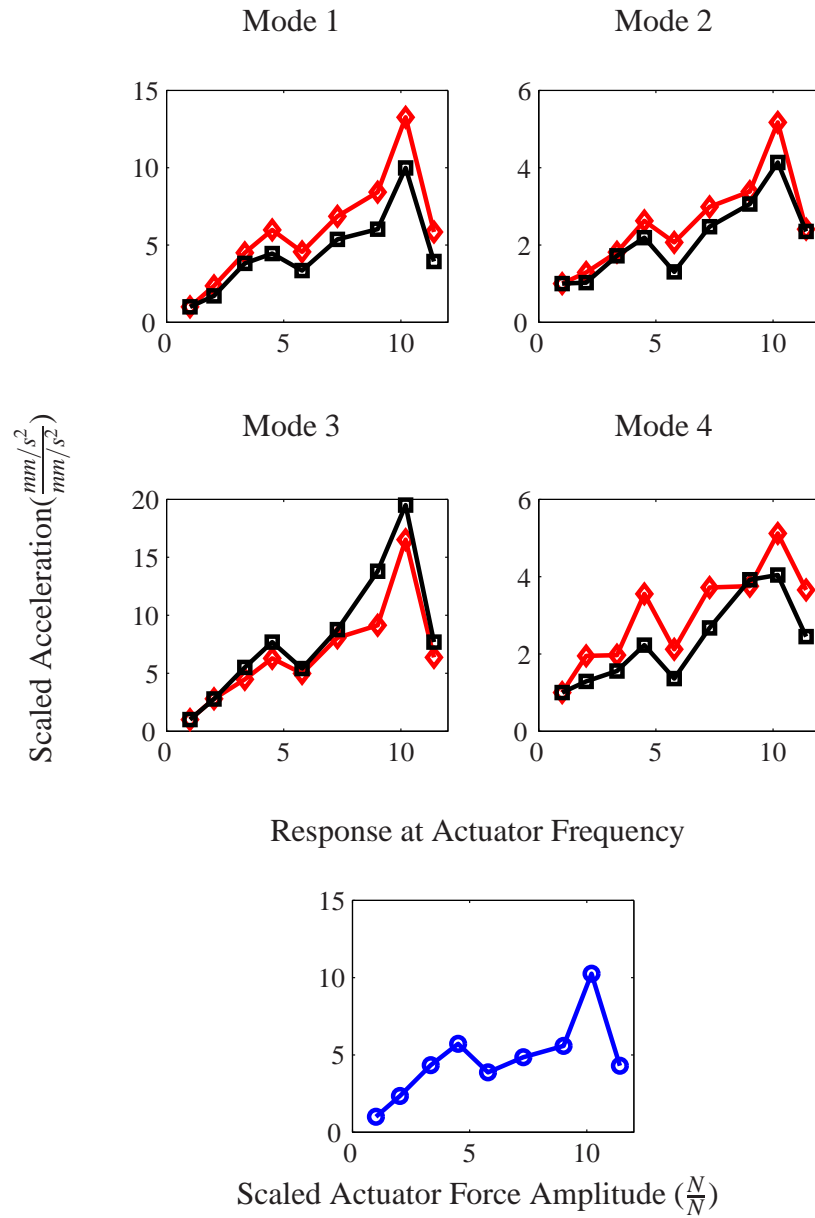


Figure 15: Scaled response amplitudes versus scaled actuator force amplitude from IM testing for left (—) and right (—) sidebands and for the response at the actuator frequency (—).

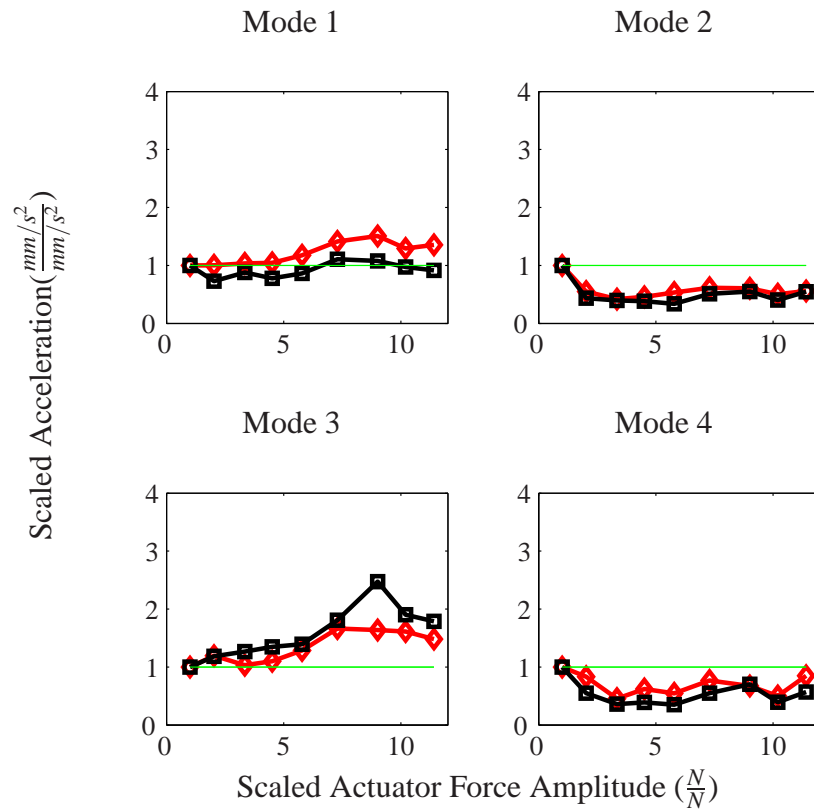


Figure 16: Normalized response amplitude versus scaled actuator amplitude from IM testing for left (—) and right (—) sidebands. The green line (—) indicates the ideal case.

## Actuator Frequency

Up to this point, results have been presented from IM tests which used an actuator frequency of

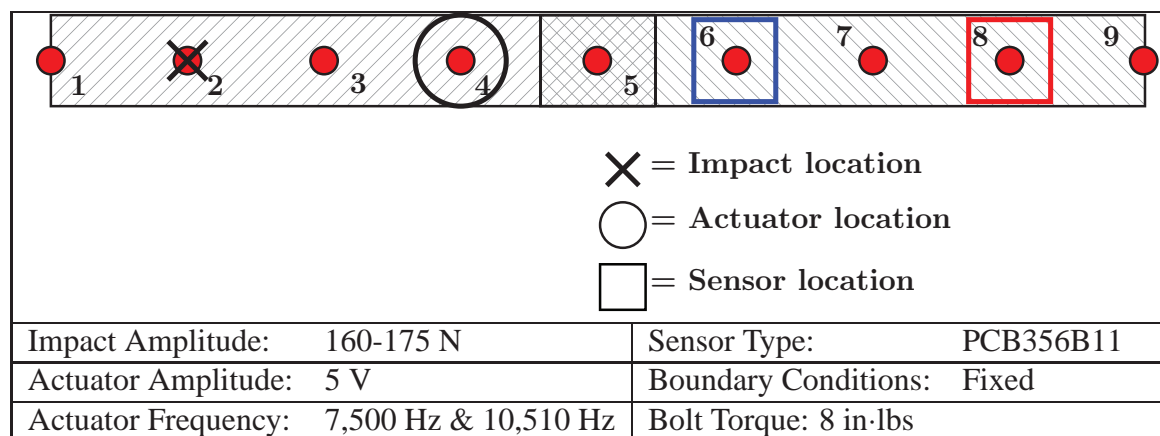


Figure 17: Setup and parameters for actuator frequency testing.

7,500 Hz. This frequency was chosen because the response spectrum of the beam assembly to a swept sine signal showed a fairly broad, flat region surrounding 7,500 Hz. It was assumed that the selection of a portion of the frequency range in which the system's response was relatively flat would prevent any underlying linear dynamics of the system from adding complexity to the IM results. However, because the interplay between the system's linear dynamics and the response to IM testing is not well understood, this assumption is, to this point, unjustified. To investigate the effect that changing the frequency of the actuated probing force has on IM results, IM tests were conducted with two different actuator frequencies: 7,500 Hz and 10,510 Hz. Five averages were taken per frequency. These frequencies were chosen because the response spectrum of the beam near 7,500 Hz exhibited a vastly different dynamics when compared to the response near 10,510 Hz, as will be shown below.

The amplitudes of the sidebands were identified for each of the two cases. Figure 18 shows these amplitudes plotted against frequency. It is clear that the magnitude of the sidebands when using 10,510 Hz for the actuator frequency are drastically larger than when using 7,500 Hz. To confirm that the linear modal vibration response of the structure helps explain the discrepancy between the amplitudes of the sidebands for different actuator frequencies, the response of the two-beam assembly to a swept sine signal was measured. The frequency response function (FRF) describing the response of the structure to the sine sweep is shown in Figure 19. The sideband amplitudes that were shown in Figure 18 are also shown for comparison. The larger amplitudes from the IM test using a 10,510 Hz actuator frequency can be explained by the fact that the underlying linear vibration response of the structure is much greater at the frequencies on either side of 10,510 Hz. Conversely, the structure has a relatively low response at frequencies near 7,500 Hz, which explains why the amplitudes of the sidebands which occurred in this frequency range were relatively small.

The results from these actuator frequency tests indicate that the linear vibration response of the structure should be taken into account when choosing the actuator frequency. In order to ensure distinct sidebands, an actuator frequency within a range in which the linear response of the structure is relatively high may be favorable. On the other hand, a frequency band in which the

linear response is relatively flat (non-dynamic) may ensure that the linear vibration response of the structure do not unduely affect the IM results. The results in the next section will explore further which of these two choices is more advantageous when performing IM testing.

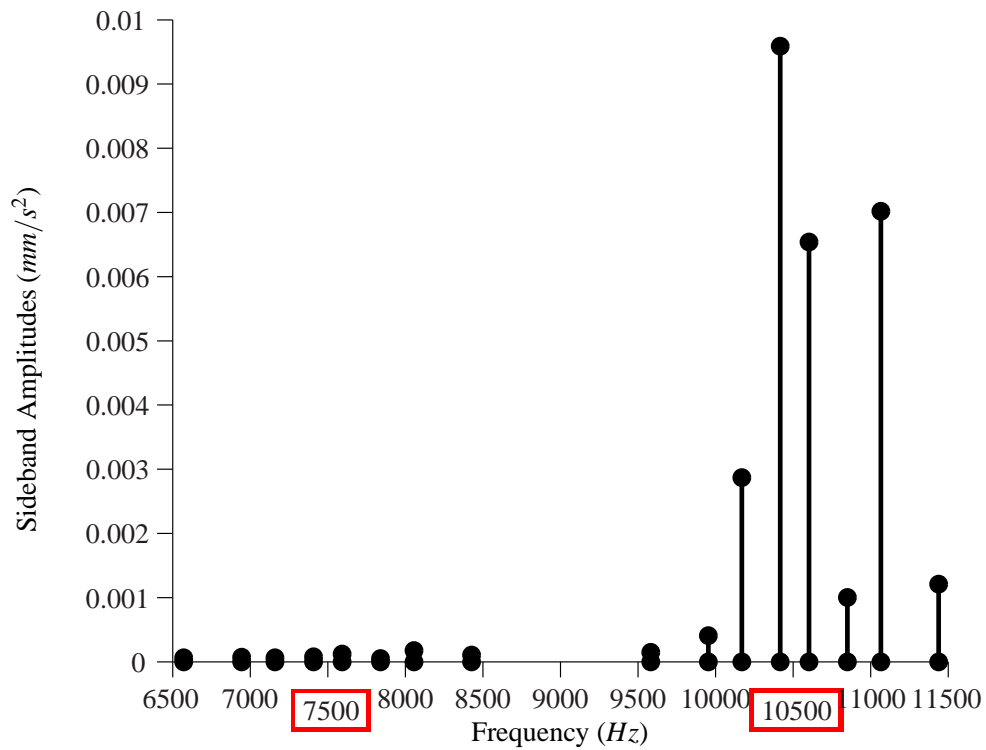


Figure 18: Sideband amplitudes from IM tests using an actuator frequency of 7,500 Hz and 10,510 Hz.

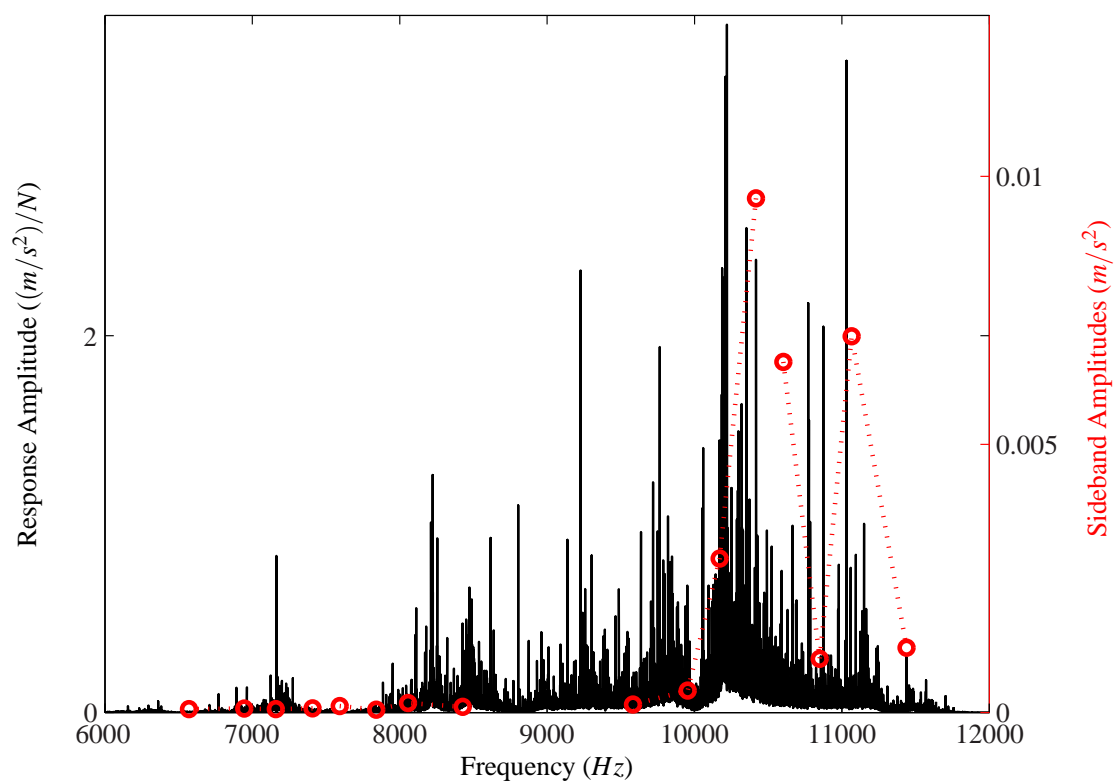


Figure 19: Amplitude of response of the two-beam assembly when subjected to a sine sweep (—) and sideband amplitudes from Figure 18 (○).

## Bolt Torque

As mentioned previously, IM has not been experimentally verified as a means to identify loose

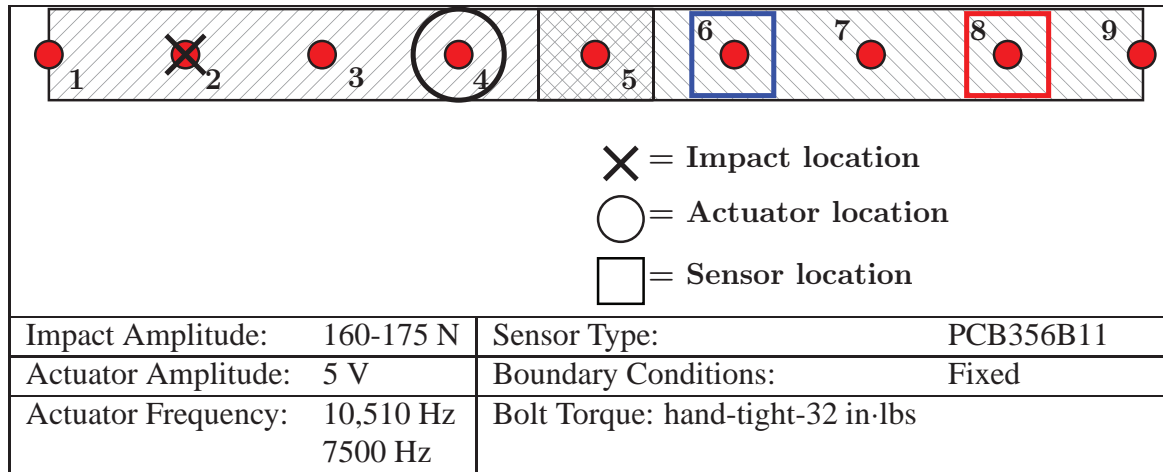


Figure 20: Setup and parameters for bolt torque sensitivity testing.

bolts. Therefore, it is essential to demonstrate that changes in bolt torque result in distinct changes in the structure's response to IM testing. Specifically, a relationship between bolt torque and the amplitudes of the sidebands is sought in order to justify the viability of using IM to detect loose bolts within a structure. To that end, IM testing was performed for bolt torques of 32 in·lbs, 16 in·lbs, 8 in·lbs, 4 in·lbs, 2 in·lbs, 1 in·lb, and hand-tight. This set of tests was first performed using an actuator frequency of 10,510 Hz and then repeated using a frequency of 7,500 Hz. Other testing parameters are shown in Figure 20. Five averages were taken per bolt torque level and during data analysis, the responses measured from the two sensors were averaged.

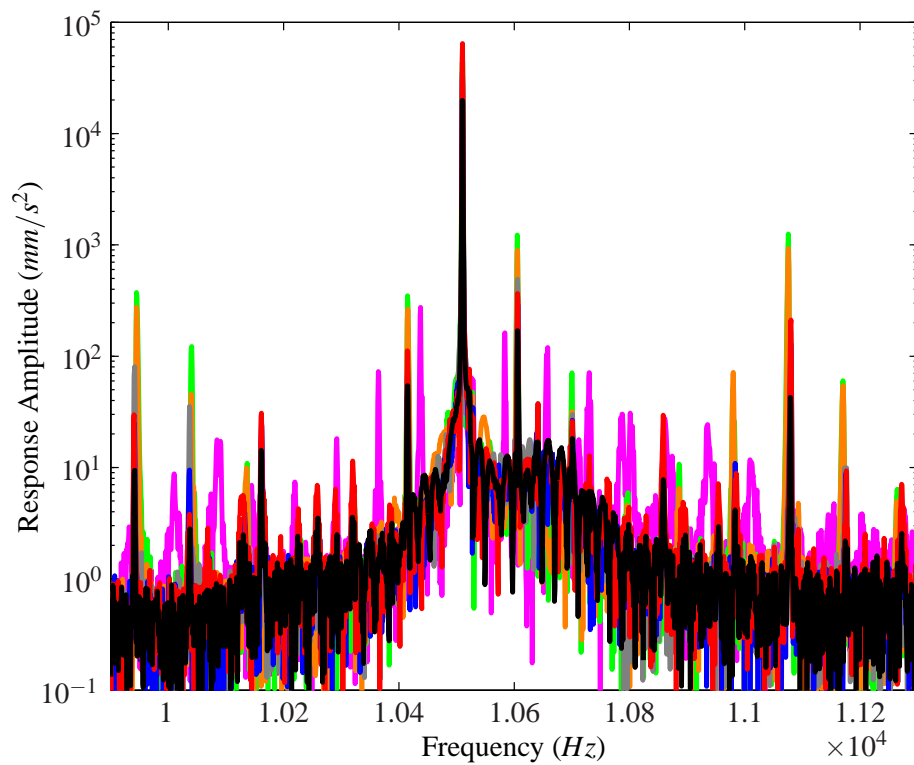


Figure 21: High frequency portion of the response spectra from IM testing for bolt torques of 32 in·lbs (—), 16 in·lbs (—), 8 in·lbs (—), 4 in·lbs (—), 2 in·lbs (—), 1 in·lb (—), and hand-tight (—).



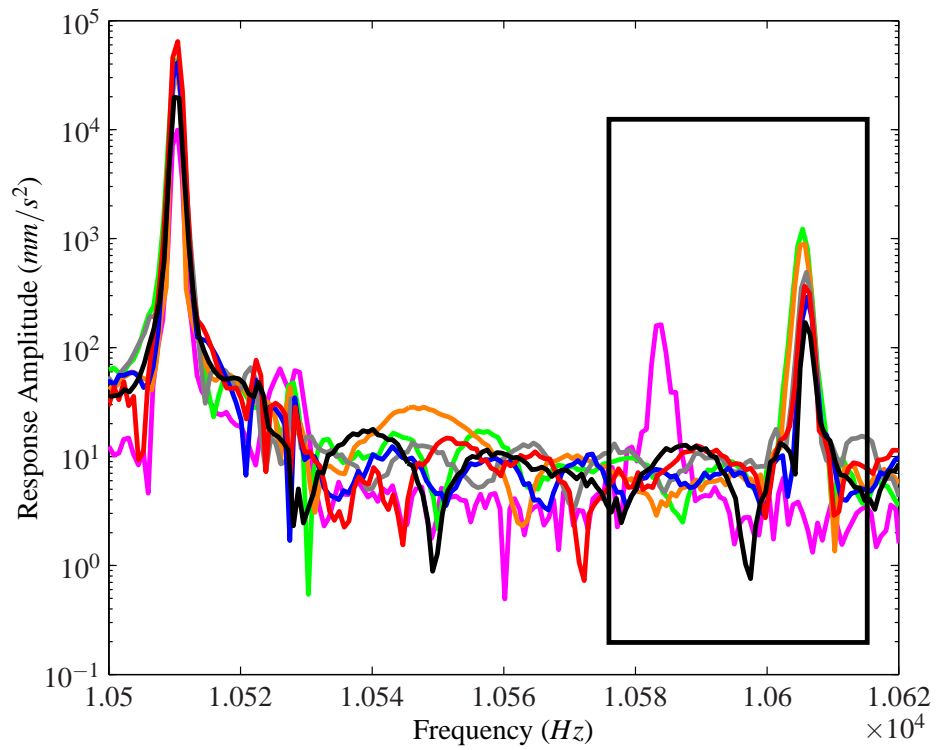


Figure 22: Response spectra (zoomed in near the actuator frequency, 10,510 Hz) from IM testing with first right sideband highlighted with a black box for bolt torques of 32 in·lbs (—), 16 in·lbs (—), 8 in·lbs (—), 4 in·lbs (—), 2 in·lbs (—), 1 in·lb (—), and hand-tight (—).

First, the data from using an actuator frequency of 10,510 Hz was analyzed. Figure 21 shows the high frequency portion of the response spectrum for IM tests at all seven torque levels. It is clear that the results from the 36 in-lb bolt torque test (shown in black) show the least amount of modulation and the results from the hand-tight bolt torque test (shown in pink) show the most modulation. Figure 22 shows a close up on the right sideband near 10,600 Hz corresponding to the first natural frequency. In general, the amplitude of the sideband increases as bolt torque decreases. This was the expected trend since it was assumed that as the torque on the bolt was lowered, the amount of nonlinearity present in the structure would increase, leading to higher-amplitude sidebands. In Figure 23, the left and right sideband amplitudes for the first four modes of vibration were plotted against bolt torque. The amplitudes of the sidebands corresponding to modes 1 and 3 tend to grow as the bolt is loosened to 1 in-lb, following the expected trend. However, when the bolt was hand-tightened, a drop in the sideband amplitudes was seen. Also, the amplitudes of the sidebands corresponding to modes 2 and 4 show a significant drop-off at the lower torque levels. These unexpected declines in sideband amplitudes can be explained by observing the low frequency portion of the response spectrum. Figure 25 shows that as the bolt torque decreases, the amplitude of response at mode 1 stays relatively constant, except at the hand-tight torque level, where a significant drop in amplitude and frequency is seen. In mode 3, the amplitudes of response also stay relatively constant when the bolt torque is 8 in-lbs or less, except at the hand-tight torque level where the response is almost undetectable. In modes 2 and 4, however, the amplitude of the modal vibration response experiences a steady decline as the bolt torque is reduced. It was assumed that these declines seen for modes 2 and 4, as well as the declines at the hand-tight torque level for modes 1 and 3, are the cause of the drop-off in sideband amplitudes seen in Figure 23. To confirm this assumption, the sideband amplitudes were normalized by the amplitude of response at the corresponding natural frequency and plotted again as a function of torque. Figure 24 shows that this normalization corrects for the decline in response amplitude at the natural frequency. Even though the impact amplitude was relatively constant across these tests, the response levels were not, resulting in the need for normalization. It is important to note that increasing the impact amplitude to keep the response levels the same would be an alternative to normalizing. However, increasing the impact amplitude changes the extent to which the nonlinearity is exercised and could, therefore, skew the results.

In order to combine the data from the different sidebands while taking into account the drop-off in sideband amplitude as the result of a drop-off in the modal vibration response, a synthesis procedure similar to the method presented in Johnson, et al. [52] was developed. This procedure calculates a modulation index,  $I$ , by computing the area under the response plot for the high frequency, or modulated, spectrum, and normalizing by the area under the response plot for the low frequency, or modal, spectrum. The modulation indices can then be plotted as a function of bolt torque to analyze trends in the data. The detailed procedure for calculating  $I$  is as follows:

1. Integrate under the response spectrum of the IM test results from the lowest to the highest natural frequency of interest. This range is determined by the frequency range that is excited by the impact. This value is called  $I_1$ .
2. Integrate under the response spectrum of the IM test results from the actuator frequency minus the highest natural frequency to the actuator frequency minus the first natural frequency. This value is called  $I_{2L}$ .

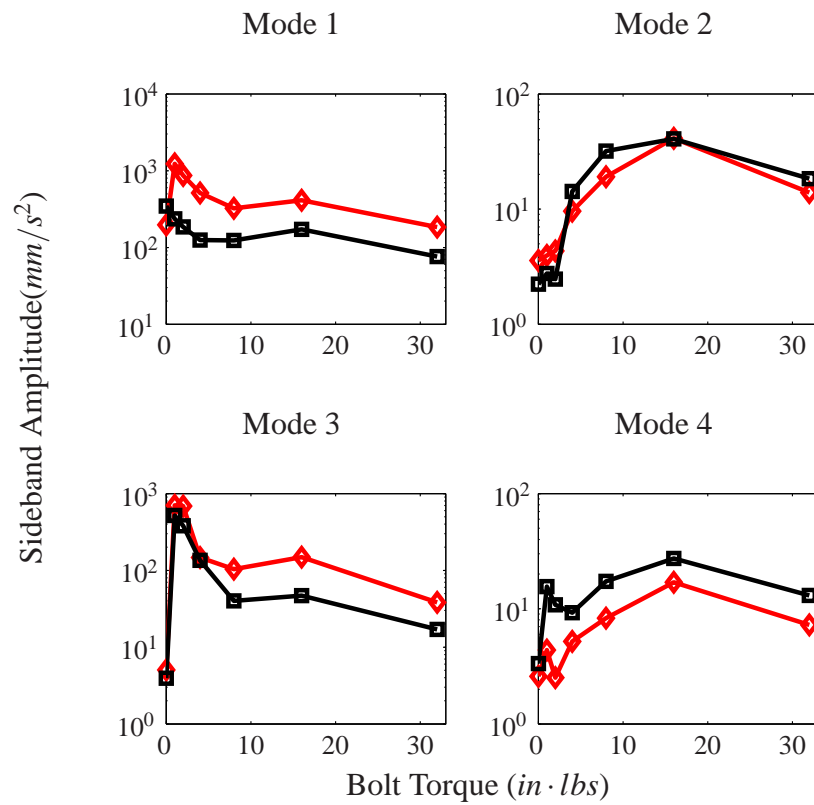


Figure 23: Left (—) and right (—) sideband amplitudes versus bolt torque for the first four modes from IM testing.

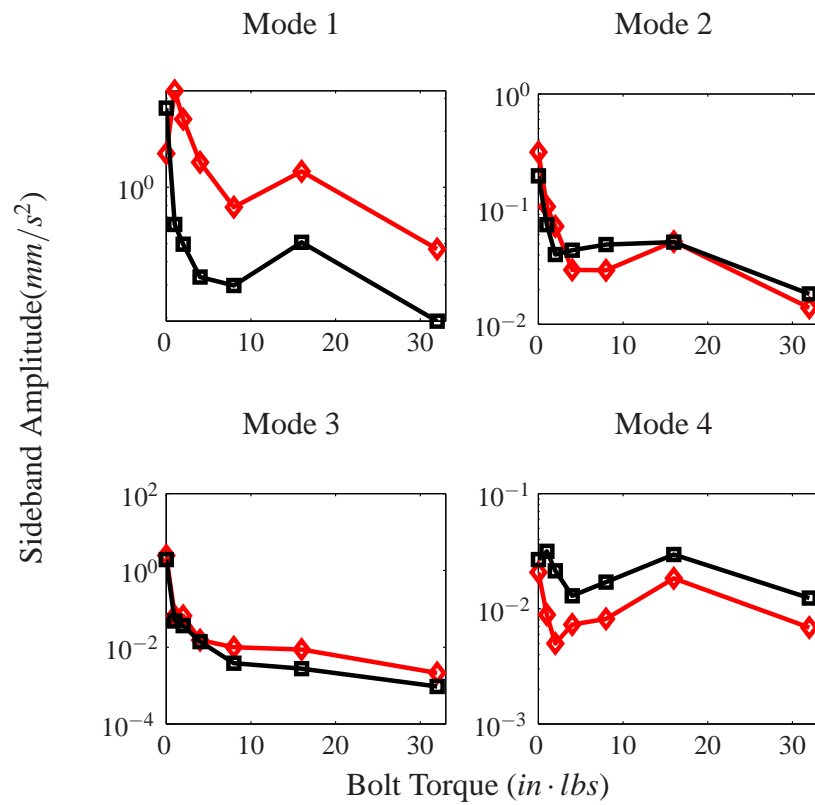


Figure 24: Left (—) and right (—) sideband amplitudes versus bolt torque for the first four modes from IM testing.

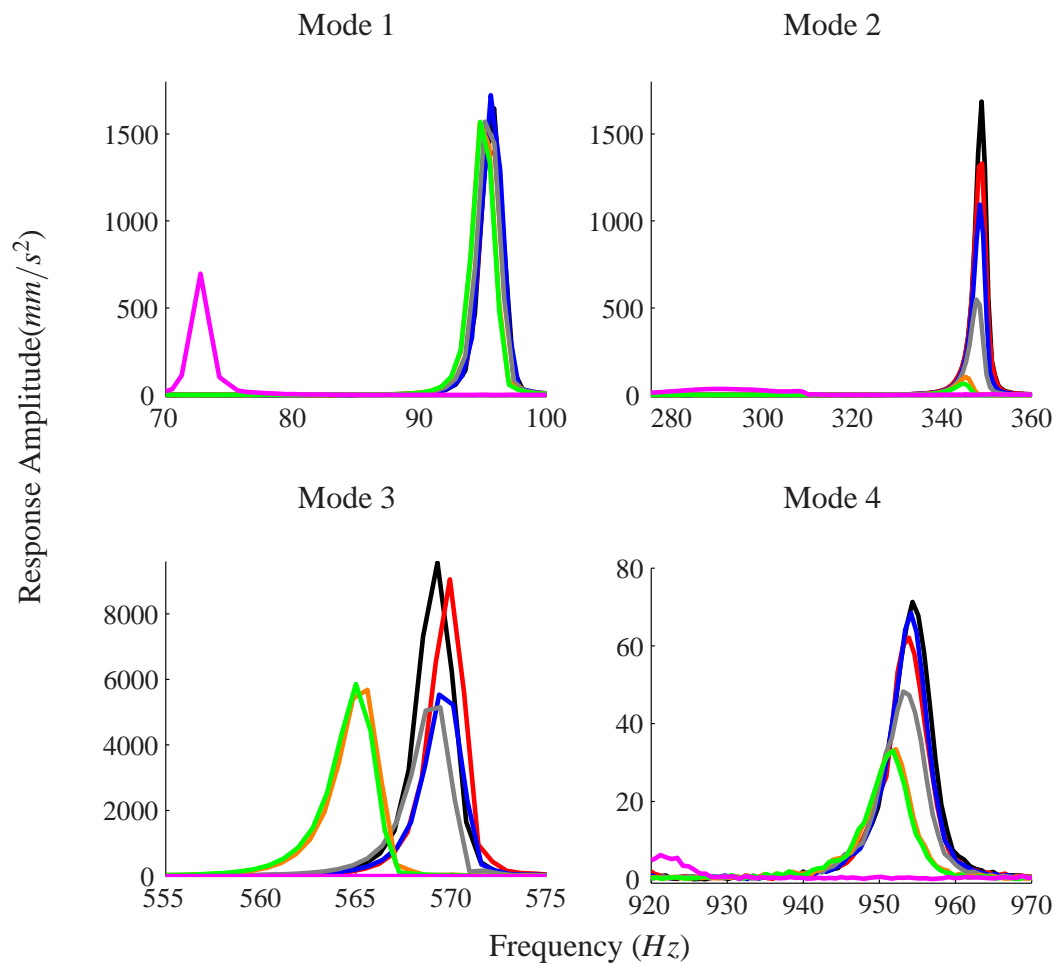


Figure 25: Response spectrum near the first four modes from IM testing for bolt torques of 32 in·lbs (—), 16 in·lbs (—), 8 in·lbs (—), 4 in·lbs (—), 2 in·lbs (—), 1 in·lbs (—), and hand-tight (—).

3. Integrate under the response spectrum of the IM test results from the actuator frequency plus the first natural frequency to the actuator frequency plus the highest natural frequency. This value is called  $I_{2R}$ .
4. Repeat steps 1 to 3 for each torque level. Scale the  $I_1$  values by the largest value to avoid numerical skewing.
5. Calculate the left and right modulation indices:  $I_{2L}/I_{1(scaled)}$  and  $I_{2R}/I_{1(scaled)}$ .
6. Plot the modulation indices versus bolt torque.

The result of this procedure for the above mentioned IM test on the two-beam specimen is shown in Figure 26. From these results, it appears that the synthesis method is able to account for the drop-off in the modal vibration response. The data follows the anticipated trend of higher sideband amplitudes for lower bolt torque.

Up to this point, only results from tests using an actuator frequency of 10,510 Hz have been presented. Recall that the underlying linear vibration response of the two-beam assembly near 10,510 Hz was quite dynamic. On the other hand, the underlying linear response of the system near 7,500 Hz was relatively flat. The above bolt torque tests were repeated using an actuator frequency of 7,500 Hz and analyzed using the synthesizing algorithm outlined above to determine how the results were affected. Figure 27 shows that the results from these tests showed a similar trend to the tests using the higher actuator frequency. The magnitude of the normalized area under the curve was smaller than that seen for the results from the tests using the 10,510 Hz actuator frequency, as expected. Qualitatively, the peaks from the tests using the 10,510 Hz actuator frequency were of higher amplitude and more easily distinguished from the noise floor than those from the tests using the 7,500 Hz frequency. Therefore, it is recommended that an actuator frequency be chosen at a frequency for which the underlying linear vibration response of the system is relatively high. However, according to the results presented in this section, IM is robust across actuator frequencies since in both cases, the results showed the anticipated trend of increasing sideband amplitudes with decreasing torques.

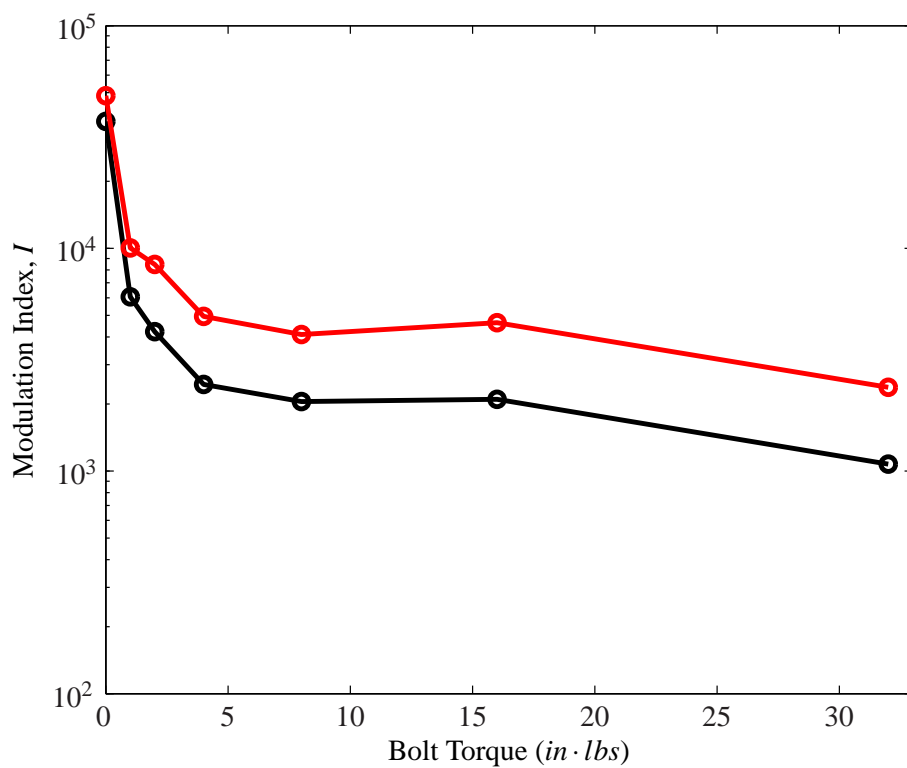


Figure 26: Normalized area under the the response spectrum over the left (—) and right (—) modulation spectra versus bolt torque for fixed boundary conditions using 10,510 Hz actuator frequency.

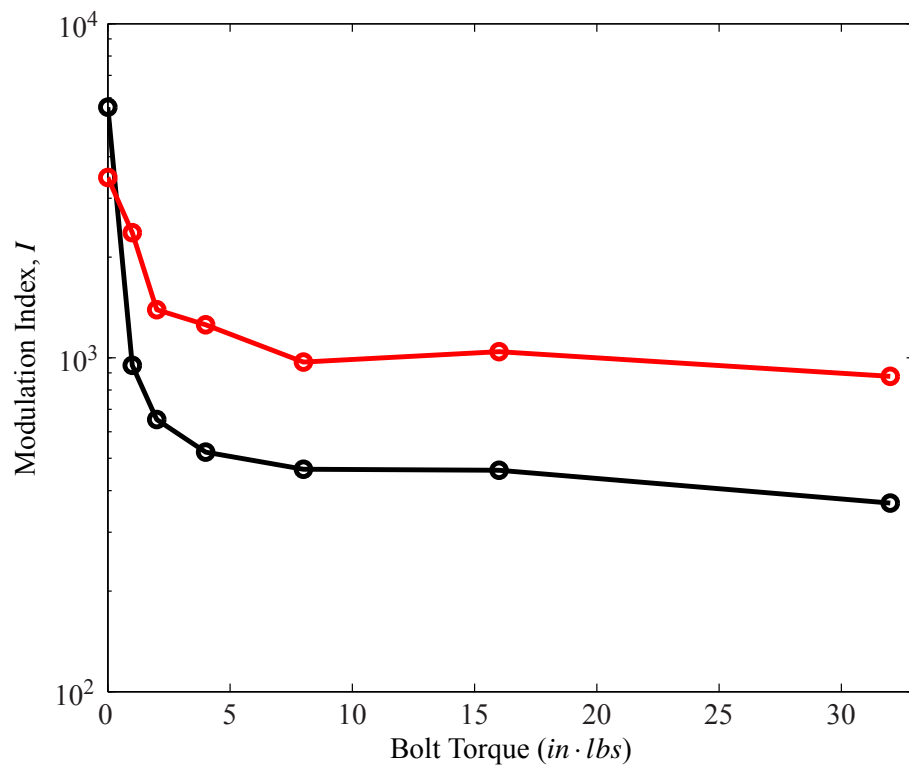


Figure 27: Normalized area under the response spectrum over the left ( — ) and right ( — ) modulation spectra versus bolt torque for fixed boundary conditions using 7,500 Hz actuator frequency.



## Boundary Conditions

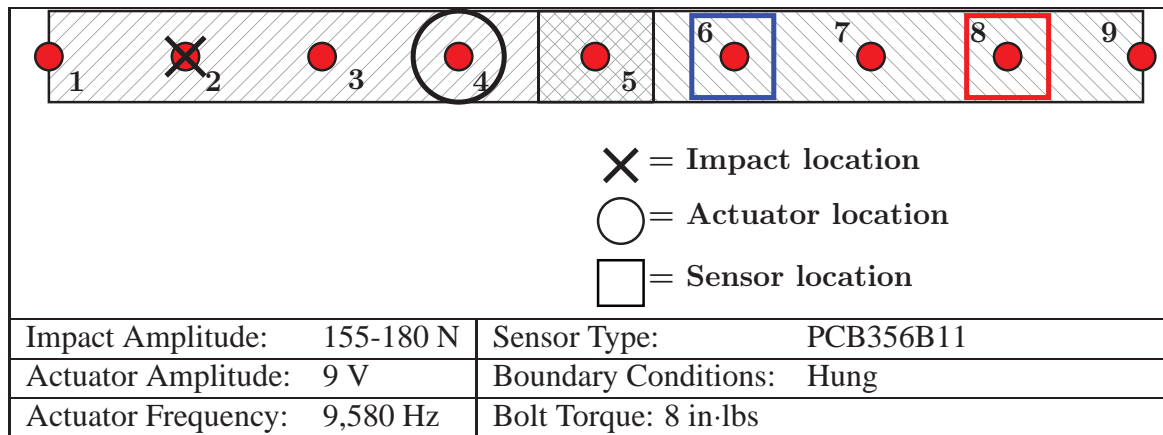


Figure 28: Setup and parameters for boundary condition sensitivity testing.

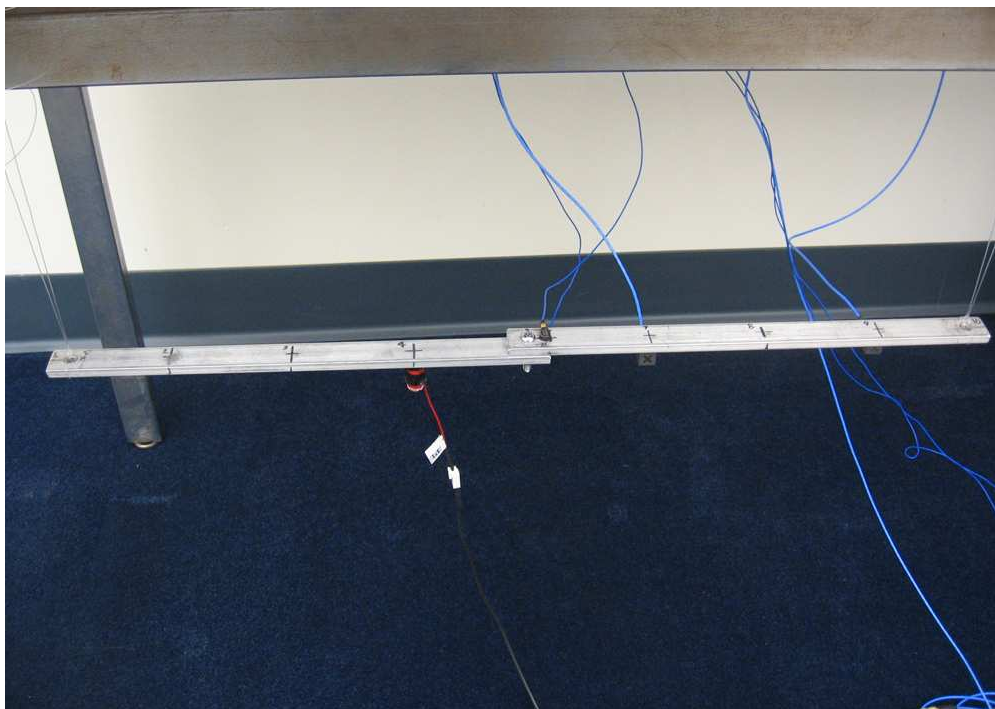


Figure 29: Two-beam, one-bolt setup with free boundary conditions.

The final parameter that was investigated was boundary condition type. All previous tests were performed with fixed boundary conditions. The bolt torque tests presented in the last section were repeated with free boundary conditions simulated by hanging the two-beam specimen from a fixed structure with fishing line to determine how the results change. As in the tests conducted for the fixed boundary conditions, IM testing was performed for bolt torques of 1 in·lb, 2 in·lbs,

4 in·lbs, 8 in·lbs, 16 in·lbs, and 32 in·lbs. The hand-tight torque test was omitted because at that torque level, the pre-load was not adequate to keep the beams from jackknifing. The actuator frequency (9,580 Hz) was chosen after the response of the system with free boundary conditions to a sine sweep was measured. The system showed a relatively high amplitude response near this frequency, more so for frequencies less than 9,580 Hz. The actuator amplitude was increased to 9 V in an effort to increase the magnitude of response after it was found that the response of the beam with free boundary conditions was of a much smaller magnitude relative to the system with fixed boundary conditions. Other test parameters are shown in Figure 28.

Figure 30 shows that the trends in modulation indices for the free boundary conditions are similar to the trends for the fixed conditions. For the free boundary conditions tests, however, the magnitudes of the modulation indices are much smaller than those for the tests using fixed conditions. This result is not surprising because the amplitude of response at the natural frequencies and the actuator frequencies for the system with free boundary conditions were up to an order of magnitude smaller than those from the tests with fixed conditions, even with the use of a higher amplitude actuator force for the free boundary condition tests. This overall lower level of response may help explain why the modulation indices for the free boundary condition tests stay relatively steady until the 1 in·lb, where there is a drastic increase. It is possible that increasing the impact amplitude would bring out the trend more clearly, because an increase in impact force would exercise the nonlinearities of the joint more strongly. Confirming this hypothesis with the free-free boundary conditions was not possible because it was difficult to perform quality impacts at higher force levels. This idea of increasing the impact force level to bring out the nonlinearities in the bolted joint will be explored again later in Chapter 4.1. In addition to these observations, it was also expected that the left modulation indices would be larger than the right indices because the underlying linear vibration response was greater for frequencies less than the actuator frequency, as mentioned above. Figure 30 confirms that prediction. The results presented in this section show that although the level of response during IM testing is affected by the boundary conditions, the trends seen in the results from different boundary conditions are similar. Therefore, it can be concluded that IM is robust across different boundary conditions.

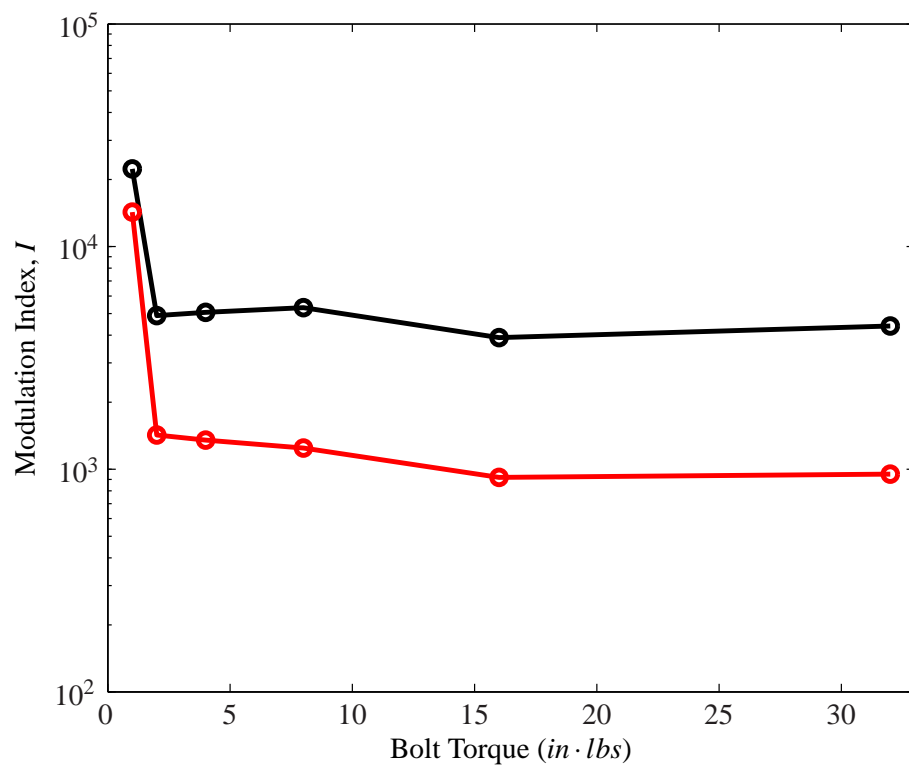


Figure 30: Normalized area under the the response spectrum over the left (—) and right (—) modulation spectra versus bolt torque for free boundary conditions.

**3.1.3 Conclusions.** The work presented in this chapter was aimed at establishing IM as a viable method for detecting loose bolts in a structure and at understanding how the test parameters associated with IM affect the diagnostic results. It was shown in Section 3.1.2 that there is a strong correlation between the amount of modulation measured during IM testing and the torque on the bolt. Therefore, it can be concluded that IM testing is a viable method for detecting loose bolts. This important conclusion motivates the remainder of this work.

In addition to establishing IM as a feasible method for identifying loose bolts, it was shown through a sensitivity study of test parameters that the underlying linear vibration response of the test specimen plays an important role in IM. For example, just as in linear modal analysis, the impact location and amplitude used in IM testing determine to what extent each mode is excited, which affects how strongly that mode is modulated. Also, the underlying linear vibration response near the actuator frequency affects how the modulated response is amplified. The linear properties of the structure must be understood in order to obtain optimum results from IM testing. Furthermore, these properties must be considered before comparing results of different IM tests. For example, if IM tests are conducted to observe the change in sideband amplitudes that result from a change in bolt torque, the same impact location should be used across all tests to avoid variation in the results due to factors other than the change in bolt torque. This conclusion will be important when a method for identifying changes in bolt torque over time is developed in Chapter 4.2.

Finally, the results presented in this chapter can be distilled to produce an optimum IM testing procedure. Recommendations for this procedure include choosing relatively high impact and actuator amplitudes to ensure the formation of distinct sidebands. The impact location should be chosen so as to avoid nodes of any modes of vibration that are of interest. The actuator frequency should be chosen in a range where the linear vibration response of the structure is relatively high to amplify the amplitudes of the sidebands and, if possible, relatively flat to avoid unwanted influence of the underlying linear vibration response on the IM results. Finally, fixed boundary conditions are preferred to free boundary conditions when the response of the structure is significantly stronger with the fixed conditions. This choice ensures the formation of distinct sidebands in the IM response.

## 3.2 Theoretical and Model Development

In the previous chapter, experimental data was analyzed to establish a correlation between the loss of torque on a bolt in a two-beam, one-bolt structure and the amount of modulation present in the structure's response during Impact Modulation (IM) testing. In this chapter, this correlation will be studied from a theoretical perspective using several analytical models. First, a single degree of freedom model will be used to derive a closed-form expression for the amplitude of the sidebands generated during IM testing. Next, a finite element model will be presented and its equations of motion will be analyzed to gain insight into which system parameters affect the amplitude of the sidebands. Finally, the sensitivity study presented in Chapter 3.1 will be repeated analytically using simulations in which the equations of motion of the finite element model are solved numerically.

The approach taken when developing the following models was to create a model that was capable of representing the phenomena observed experimentally during IM testing. As discussed in Section 2.3, much of the technical literature has been directed towards modeling bolts and bolted joints. The intent of this work is not to model the micro-scale geometry or dynamics of the bolt, such as thread angle or contact friction in the threads, but rather to model the macro-scale effect of the bolted joint on the system. Because of this more global perspective, this work presents models in which a bolted joint is modeled as a combination of linear springs, nonlinear springs, and linear dampers. Parameters associated with micro-scale phenomena such as slip-stick and micro-impacts are lumped into macro-scale stiffness and damping parameters. It is assumed that these parameters are sufficient to characterize the nonlinearities present at the local bolt level.

The form of the nonlinearity used in the models presented here were chosen based on the experimental results. As seen throughout the previous chapter, the sidebands occurred at frequencies equal to the actuator, or probing force, frequency plus and minus the natural frequency. This combination points to the use of a quadratic nonlinearity, which will be shown mathematically in the next section. A cubic nonlinearity would manifest as sidebands at frequencies equal to the probing force frequency plus and minus twice the natural frequency. Physically, a quadratic spring is a reasonable choice because its use results in a nonsymmetric force-deflection curve, as shown in Figure 31. In the case of the two-beam, one-bolt assembly, if the coefficient of the quadratic spring is negative, the nonlinear spring will have a softening effect when the relative displacement of the beams at the bolted joint is positive. This softening effect is physically reasonable because the beams would be pulling apart with only the bolt to resist the motion. On the other hand, when the beams are being compressed together, their motion is being opposed with greater force. For these negative values of relative displacement, the quadratic spring will have a stiffening effect. Based on this physical interpretation and on the experimental results, a quadratic spring will be used in the models presented in the following sections.

**3.2.1 Single Degree of Freedom Model.** For applications in which IM is used for crack detection, theoretical models involving changes in the material stresses and strains are typically presented. Because this work assumes that changes in bolt torque will be detected by measuring a response characteristic that is a result of a change in stiffness and damping parameters, a novel modeling approach is needed. Therefore, as a first step towards establishing a theoretical basis for applying IM to bolted joints, a single degree of freedom model was developed. Although the systems that were explored experimentally in this work cannot be fully described by a single degree of freedom model, the following derivation can provide insight into how certain system parameters affect the

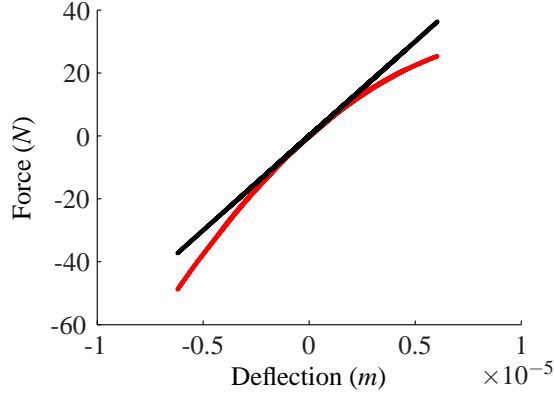


Figure 31: Force-deflection curve for the bolt stiffness used in the simulations (—). The linear force-deflection curve (—) is shown for reference.

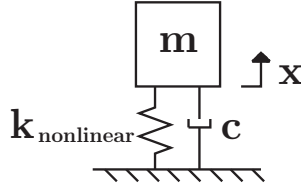


Figure 32: Schematic of the single degree of freedom system.

response of the system during IM testing.

Consider the single degree of freedom, nonlinear model shown in Figure 32, subject to a two term excitation. The equation of motion for this model is given by:

$$m\ddot{x} + c\dot{x} + kx + k_{sq}x^2 = F_1^* \cos(\Omega_1 t) + F_2^* \cos(\Omega_2 t) \quad (1)$$

where  $F_1^*$ ,  $F_2^*$ ,  $\Omega_1$ , and  $\Omega_2$  are constants. The two term excitation is selected because IM uses both an impact force and a high frequency probing force simultaneously. In order to simplify the computations, however, the impact force is replaced by a single-frequency input force. As mentioned previously, a quadratic spring nonlinearity is chosen because the experimental data, which was presented in the previous chapter, exhibited nonlinear characteristics that are indicative of a quadratic nonlinearity.

Next, define the following substitutions:

$$2\varepsilon\mu = \frac{c}{m} \quad \varepsilon\alpha = \frac{k_{sq}}{m} \quad F_1 = F_1^*/m \quad F_2 = F_2^*/m.$$

Equation (1) now becomes

$$\ddot{x} + \omega_o^2 x = -2\varepsilon\mu\dot{x} - \varepsilon\alpha x^2 + F_1 \cos(\Omega_1 t) + F_2 \cos(\Omega_2 t). \quad (2)$$

Assume that  $\Omega_1 \approx \omega_o$  and  $\Omega_2$  is away from  $\omega_o$ . Further,  $\Omega_1 = \omega_o + \varepsilon\sigma$ , where  $\sigma$  describes  $\Omega_1$ 's position relative to  $\omega_o$ . Finally,  $F_1 = \varepsilon f_1$  where the  $\varepsilon$  indicates that a small force will result in a large response. This assumption is valid because it was assumed that  $\Omega_1 \approx \omega_o$ .

The method of multiple time scales as presented in [53] can be used to solve Equation (2). The first step in the multiple time scales method is to assume the following solution for  $x$ :

$$x(t, \varepsilon) = x_o(T_o, T_1) + \varepsilon x_1(T_o, T_1) + \dots \quad (3)$$

where  $T_o = t$  and  $T_1 = \varepsilon t$ . The external forces in terms of  $T_o$  and  $T_1$  are now written as:

$$\begin{aligned} E_{ext}(t) &= \varepsilon f_1 \cos[(\omega_o + \varepsilon \alpha)t] + F_2 \cos(\Omega_2 t) \\ E_{ext}(T_o, T_1) &= \varepsilon f_1 \cos(\omega_o T_o + \alpha T_1) + F_2 \cos(\Omega_2 T_o). \end{aligned} \quad (4)$$

Substitute Equation (3) and (4) into Equation (2) noting that

$$\begin{aligned} \frac{d(\cdot)}{dt} &= \frac{dT_o}{dt} \frac{\delta(\cdot)}{\delta T_o} + \frac{dT_1}{dt} \frac{\delta(\cdot)}{\delta T_1} + \dots = D_o + \varepsilon D_1 + \dots \\ \frac{d^2(\cdot)}{dt^2} &= D_o^2 + 2\varepsilon D_o D_1 + \varepsilon^2 (D_1^2 + 2D_o D_2) + \dots \end{aligned}$$

and including only terms of order  $\varepsilon^0$  and  $\varepsilon^1$  to yield:

$$\begin{aligned} D_o^2 x_o + 2\varepsilon D_o D_1 x_o + \varepsilon D_o^2 x_1 + \omega_o^2 x_o + \omega_o^2 \varepsilon x_1 = \\ -2\varepsilon \mu D_o x_o - \varepsilon \alpha x_o^2 + \varepsilon f_1 \cos(\omega_o T_o + \sigma T_1) + F_2 \cos(\Omega_2 T_o). \end{aligned}$$

The coefficients of  $\varepsilon^0$  and  $\varepsilon^1$  are then equated to give:

$$\varepsilon^0 : \quad D_o^2 x_o + \omega_o^2 x_o = F_2 \cos(\Omega_2 T_o) \quad (5)$$

$$\varepsilon^1 : \quad D_o^2 x_1 + \omega_o^2 x_1 = -2D_o D_1 x_o - 2\mu D_o x_o - \alpha x_o^2 + f_1 \cos(\omega_o T_o + \sigma T_1). \quad (6)$$

The general solution of Equation (5) is

$$x_o = A(T_1) e^{i\omega_o T_o} + \Lambda e^{i\Omega_2 T_o} + c.c. \quad (7)$$

where c.c. stands for the complex conjugate of the previous terms. Next, substitute Equation (7) into Equation (6) writing the cosine term in its complex form to give:

$$-\omega_o^2 A e^{i\omega_o T_o} - \Omega_2^2 \Lambda e^{i\Omega_2 T_o} + \omega_o^2 A e^{i\omega_o T_o} + \omega_o^2 \Lambda e^{i\Omega_2 T_o} + c.c. = \frac{F_2}{2} e^{i\Omega_2 T_o} + c.c.$$

Therefore,

$$\Lambda = \frac{F_2}{2(\omega_o^2 - \Omega_2^2)}. \quad (8)$$

Equation (8) matches the forced response of a linear system.

Next substitute Equation (7) into Equation (6) noting that

$$\begin{aligned} D_o x_o &= \frac{\delta x_o}{\delta T_o} = i\omega_o A e^{i\omega_o T_o} + i\Omega_2 \Lambda e^{i\Omega_2 T_o} + c.c \\ D_o D_1 x_o &= \frac{\delta}{\delta T_o} \left( \frac{\delta x_o}{\delta T_1} \right) = i\omega_o A' e^{i\omega_o T_o} + c.c. \quad \text{where } A' = \frac{d}{dT_1}(A) \end{aligned}$$

and again writing the cosine term in its complex form:

$$\begin{aligned} D_o^2 x_1 + \omega_o^2 x_1 = & -(2i\omega_o A' + 2\mu i\omega_o A - \frac{f_1}{2} e^{\sigma T_1}) e^{i\omega_o T_o} - 2\mu i\Omega_2 \Lambda e^{i\Omega_2 T_o} \\ & - \alpha (A^2 e^{2i\omega_o T_o} + 2A\Lambda e^{(\omega_o + \Omega_2) iT_o} + 2A\bar{\Lambda} e^{(\omega_o - \Omega_2) iT_o} \\ & + \Lambda^2 e^{2i\Omega_2 T_o} + A\bar{A} + \Lambda\bar{\Lambda}) + c.c. \end{aligned} \quad (9)$$

Next, eliminate the terms of Equation (9) which would lead to secular terms in the solution  $x_1$ . Secular terms are terms which allow the solution to become non-periodic or to grow without bound as  $t$  increases. In the case of Equation (9), terms that contain  $e^{i\omega_o T_o}$  must be eliminated to prevent the secular terms  $T_o e^{i\omega_o T_o}$  from appearing in the solution for  $x_1$  and, thus making the overall solution,  $x$ , non-periodic. Therefore,

$$2i\omega_o A' + 2\mu i\omega_o A - \frac{f_1}{2} e^{\sigma T_1} = 0. \quad (10)$$

To solve Equation (10), first assume that

$$A = ae^{i\beta} \quad \text{where } a = a(T_1) \text{ and } \beta = \beta(T_1). \quad (11)$$

Then, substitute Equation (11) into Equation (10) noting that

$$\begin{aligned} A' = \frac{dA}{dT_1} = a\beta' ie^{i\beta} + a' e^{i\beta} \quad \text{where } a' = \frac{da}{dT_1} \text{ and } \beta' = \frac{d\beta}{dT_1} : \\ 2\omega_o(a'i + \mu ai - a\beta') e^{i\beta} = \frac{f_1}{2} e^{\sigma T_1}. \end{aligned} \quad (12)$$

Separate Equation (12) into real and imaginary parts to yield:

$$\begin{aligned} -2\omega_o a\beta' &= \frac{f_1}{2} \cos(\sigma T_1 - \beta) \\ \text{and} \quad 2\omega_o a' + 2\omega_o \mu a &= \frac{f_1}{2} \sin(\sigma T_1 - \beta). \end{aligned} \quad (13)$$

The equations in (13) can be transformed into an autonomous system, that is a system in which time does not explicitly appear, by introducing

$$\begin{aligned} \gamma &= \sigma T_1 - \beta \\ \text{and} \quad \gamma' &= \sigma - \beta'. \end{aligned} \quad (14)$$

To find the steady state response of the system, assume that  $a' = \gamma' = 0$ . Therefore, the equations in (13) are written as:

$$\begin{aligned} -2\omega_o a\sigma &= \frac{f_1}{2} \cos(\gamma) \\ \text{and} \quad 2\omega_o \mu a &= \frac{f_1}{2} \sin(\gamma). \end{aligned} \quad (15)$$

Square and add both sides of the equations in (15) to give the following equation for the steady state amplitude,  $A(T_1)$ , of the response at  $\omega_o$ :

$$a^2 = \frac{f_1^2}{\omega_o^2 (\mu^2 + \sigma^2)}. \quad (16)$$



Equation (16) is the same expression for the forced response of a linear system. In the case of a quadratic nonlinearity, the nonlinear spring coefficient,  $\alpha$ , does not affect the amplitude of response near  $\omega_o$ . Interestingly, the derivation for the response of a system with a cubic nonlinearity (not presented here) shows that the response at  $\omega_o$  does depend on the coefficient of cubic nonlinearity.

To determine an expression for the sideband amplitudes, assume the following solution for  $x_1$ :

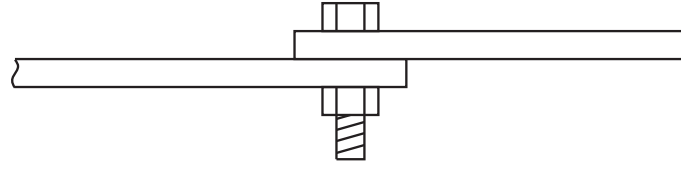
$$x_1 = \Psi_1 e^{i\Omega_2 T_o} + \Psi_2 e^{2i\omega_o T_o} + \Psi_3 e^{(\omega_o + \Omega_2)iT_o} + \Psi_4 e^{(\omega_o - \Omega_2)iT_o} + \Psi_5 e^{2i\Omega_2 T_o} + \Psi_6 A\bar{A} + \Psi_7 \Lambda\bar{\Lambda}. \quad (17)$$

Then, substitute Equation (17) into Equation (9) and equate coefficients of like terms. This yields the following expressions for the amplitude of the sidebands at  $\Omega_2 + \omega_o$  and  $\Omega_2 - \omega_o$ :

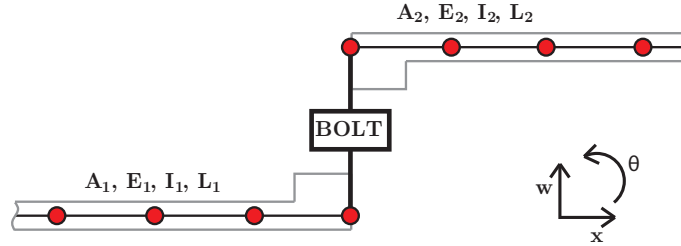
$$\begin{aligned} \Psi_3 &= \frac{2A\alpha\Lambda}{(\Omega_2 + \omega_o)^2 - \omega_o^2} \\ \text{and} \quad \Psi_4 &= \frac{2\bar{A}\alpha\Lambda}{(\Omega_2 - \omega_o)^2 - \omega_o^2}. \end{aligned} \quad (18)$$

These expressions give a theoretical relationship between the sideband amplitudes,  $\Psi_3$  and  $\Psi_4$ , and the characteristics of the system. They show that the amplitude of each sideband is linearly proportional to the coefficient of nonlinearity. Also, the amplitudes of the sidebands are dependent on the system's response at the excitation frequencies, an assertion that will be examined experimentally in the next chapter. Another interesting observation about Equation (18) is that it implies that the amplitudes of the sidebands will not be symmetric about  $\Lambda$ , the response at  $\Omega_2$ , because the denominators depend on the sideband frequency. The dependence of the sideband amplitudes on the sideband frequency suggests that this dependence will involve more complexity in a multi-degree of freedom system in which it is possible to have modes in the frequency range of the sidebands. To address this additional complexity and to continue to explore how the parameters of a nonlinear system affect its response to IM, a multi-degree of freedom model was developed. This model will be described in the next section.

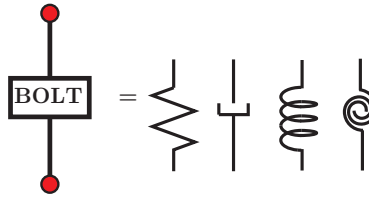
**3.2.2 Finite Element Model.** Although the single degree of freedom model presented above lends important insights into the relationship between certain system parameters and the generation of sidebands during IM testing, it is not sufficient for studying aspects of IM which pertain to its implementation, such as the effect of sensor or impact location. In addition, as mentioned in the previous section, a multi-degree of freedom model is needed to explore the relationship between the amplitudes of the sidebands generated during IM testing and the frequency at which those sidebands occur. Therefore, a multi-degree of freedom system was devised and modeled. The system chosen was comprised of two beams connected by a single bolt in a lap joint configuration. (See Figure 33a.) This system was chosen to match the specimen used in the experimental work. To model the bolted assembly, the system was first divided into two sections along the line of the bolt. Each section was broken down into finite element beams. The beam elements which represent the lapped portion of the bolted joint were assigned double thickness. The two sections were connected by a linear translational spring, a quadratic translational spring, a linear rotational spring, a quadratic rotational spring, a linear translational damper, and a linear rotational damper between the last node of the first section and the first node of the second section. (See Figure 33b.) Material and geometric properties of the system were chosen to match the experimental specimen.



(a) Beam with lap joint.



(b) Finite element model.



(c) Bolt model: The bolt model is comprised of a linear translational spring, a quadratic translational spring, a linear rotational spring, a quadratic rotational spring, a linear translational damper, and a linear rotational damper.

Figure 33: Schematic of the two-beam, one-bolt assembly used in the finite element model simulations.

The choices for stiffness and damping coefficients are discussed below. The resulting equations of motion for the system are:

$$[M]_{2N \times 2N} \{\ddot{q}\}_{2N \times 1} + [C]_{2N \times 2N} \{\dot{q}\}_{2N \times 1} + [K]_{2N \times 2N} \{q\}_{2N \times 1} = \{F_{external}\}_{2N \times 1} + \{F_{bolt}\}_{2N \times 1} \quad (19)$$

where N is the number of finite element nodes and the 2N degrees of freedom can be expressed as

$$\{q\}_{2N \times 1} = \begin{Bmatrix} w_1 \\ \theta_1 \\ w_2 \\ \theta_2 \\ \vdots \\ w_N \\ \theta_N \end{Bmatrix}$$

where  $w_n$  represents the transverse deflection of node  $n$  and  $\theta_n$  represents the rotation of node  $n$  measured from horizontal.

There are  $\frac{N}{2}$  nodes per section,  $M$ ,  $C$ , and  $K$  are the linear assembled mass, damping, and stiffness matrices for the finite elements of the beams, and  $F_{external}$  is the vector of applied forces. The vector  $F_{bolt}$  contains the terms which couple the two beams together.  $F_{bolt}$  is comprised of both linear and nonlinear terms. As previously mentioned, the bolt was modeled with a nonlinear translational spring with both linear and quadratic stiffness, a nonlinear rotational spring with both linear and quadratic stiffness, a linear damper, and a rotational damper. If  $k_{lin}$  is the linear spring stiffness,  $k_{quad}$  is the quadratic spring stiffness,  $k_{\theta}$  is the linear rotational spring stiffness,  $k_{\theta quad}$  is the quadratic rotational spring stiffness,  $c$  is the linear damping coefficient, and  $c_{\theta}$  is the linear rotational damping coefficient, then

$$\{F_{bolt}\}_{N \times 1} = \begin{Bmatrix} 0 \\ \vdots \\ k_{lin}(w_{\frac{N}{2}} - w_{\frac{N}{2}-1}) + c(\dot{w}_{\frac{N}{2}} - \dot{w}_{\frac{N}{2}-1}) + k_{quad}(w_{\frac{N}{2}} - w_{\frac{N}{2}-1})^2 \\ k_{\theta}(\theta_{\frac{N}{2}} - \theta_{\frac{N}{2}-1}) + c_{\theta}(\dot{\theta}_{\frac{N}{2}} - \dot{\theta}_{\frac{N}{2}-1}) + k_{\theta quad}(\theta_{\frac{N}{2}} - \theta_{\frac{N}{2}-1})^2 \\ -k_{lin}(w_{\frac{N}{2}} - w_{\frac{N}{2}-1}) - c(\dot{w}_{\frac{N}{2}} - \dot{w}_{\frac{N}{2}-1}) - k_{quad}(w_{\frac{N}{2}} - w_{\frac{N}{2}-1})^2 \\ -k_{\theta}(\theta_{\frac{N}{2}} - \theta_{\frac{N}{2}-1}) - c_{\theta}(\dot{\theta}_{\frac{N}{2}} - \dot{\theta}_{\frac{N}{2}-1}) - k_{\theta quad}(\theta_{\frac{N}{2}} - \theta_{\frac{N}{2}-1})^2 \\ 0 \\ \vdots \end{Bmatrix}. \quad (20)$$

The analysis of the single degree of freedom system in Section 3.2.1 concluded with a closed-form expression for the amplitude of the sidebands generated by applying two forces that simulated IM testing. (See Equation (18).) In the more complex case of a multi-degree of freedom, finite element model, no such expression can be derived. However, insight into which parameters have a significant effect on the sidebands can be gained through manipulating and analyzing the equations of motion and through a basic sensitivity study in which parameters are varied and changes in the sidebands are measured. The following sections will explore the relationship between the sidebands and the system parameters using the multi-degree of freedom, finite element model described in this section.

### Analysis of the Equations of Motion

In order to gain insight into which parameters affect the generation of the sidebands during IM testing, the terms in the equations of motion presented in Equation (19) can be rearranged so that all the nonlinearities appear on the right side. This is advantageous because the equations now describe a linear system being perturbed by a combination of linear and nonlinear forces, as seen

in the following:

$$\begin{bmatrix} M \end{bmatrix} \{\ddot{q}\} + \begin{bmatrix} C^* \end{bmatrix} \{\dot{q}\} + \begin{bmatrix} K^* \end{bmatrix} \{q\} = \begin{Bmatrix} 0 \\ \vdots \\ f_{j,pump} \\ 0 \\ \vdots \\ f_{k,probe} \\ 0 \\ \vdots \end{Bmatrix} + \begin{Bmatrix} 0 \\ \vdots \\ k_d q_d^2 \\ 0 \\ \vdots \end{Bmatrix}. \quad (21)$$

Note that the  $K^*$  matrix is the addition of the material stiffness matrix  $K$  from Equation (19) and the linear stiffness coefficients from Equation (20). Similarly, the  $C^*$  matrix is a combination of the material damping and the linear damping from the expression for  $F_{bolt}$ . Also, to simplify the initial analysis, assume that the nonlinearity, which is now being considered as an applied force, is only present at a single node, node  $d$ , as seen in the last term of the above equation. This assumption will later be relaxed so that the nonlinearity is present at more than one node, as is the case when applying Equation (20). Finally, choose the forces to represent the forces used during IM testing. As in the previous section, replace the impact force with a single-frequency input force, called the pumping force.  $f_{j,pump}$  is the pumping force applied at node  $j$  and  $f_{k,probe}$  is the probing force applied at node  $k$ .

Next, transform the above system into modal coordinates. Let

$$q = [\Psi]p \quad (22)$$

where  $[\Psi] = [\Psi_1 \Psi_2 \dots \Psi_{2N}]$  and  $\Psi_n$  = the  $n^{th}$  modal vector. Substitute this expression for  $q$  into Equation (21), and assume proportional damping to yield:

$$\begin{bmatrix} M_{diagonal} \end{bmatrix} \{\ddot{p}\} + \begin{bmatrix} C_{diagonal} \end{bmatrix} \{\dot{p}\} + \begin{bmatrix} K_{diagonal} \end{bmatrix} \{p\} = \begin{bmatrix} \Psi \end{bmatrix}^T \begin{Bmatrix} 0 \\ \vdots \\ f_{j,pump} \\ 0 \\ \vdots \\ f_{k,probe} \\ 0 \\ \vdots \end{Bmatrix} + \begin{bmatrix} \Psi \end{bmatrix}^T \begin{Bmatrix} 0 \\ \vdots \\ k_d q_d^2 \\ 0 \\ \vdots \end{Bmatrix}. \quad (23)$$

Let  $f_{j,pump} = F_{pump} \cos(\omega_{pump} t)$  and  $f_{k,probe} = F_{probe} \cos(\omega_{probe} t)$  where  $\omega_{pump}$  and  $\omega_{probe}$  are natural frequencies.

Because the system is being considered as a linear system, the principle of superposition can be used to examine the response to each excitation force separately. First, consider only the response

to the pumping force. Because  $\omega_{pump}$  was assumed to be a natural frequency of the system, the steady state response will contain only the mode at  $\omega_{pump}$ ,  $\Psi_{pump}$ . Similarly, the response to the probing signal will only contain the mode at  $\omega_{probe}$ ,  $\Psi_{probe}$ . Therefore, the steady-state response to just the pumping and probing signals can be expressed as:

$$\{p\} = \alpha [\Psi_{pump}] \cos(\omega_{pump}t) + \beta [\Psi_{probe}] \cos(\omega_{probe}t). \quad (24)$$

It is important to note that  $\alpha[\Psi_{pump}]$  and  $\beta[\Psi_{probe}]$  are functions of the node at which the pumping and probing forces are applied. For example, if  $f_{pump}$  is applied at a node which is also a node of the mode at  $\omega_{pump}$ ,  $\alpha[\Psi_{pump}]$  will be a vector of zeros. Conversely, if  $f_{pump}$  is applied at a non-node of the mode at  $\omega_{pump}$ ,  $\alpha[\Psi_{pump}]$  will be non-zero. Further, each different force location will scale the  $\Psi$  vector differently. This dependence of the response on the input force node will be important later when a relationship between sideband amplitude and the location of the input force is sought.

Next, consider the response of the system to the nonlinear force. Taking into account the response to the pumping and probing forces found in Equation (24), the form of the nonlinear force can be expanded as follows:

$$\begin{aligned} k_d q_d^2 &= k_d [\alpha^2 \Psi_{pump,d}^2 \cos^2(\omega_{pump}t) + \beta^2 \Psi_{probe,d}^2 \cos^2(\omega_{probe}t) \\ &\quad + 2\alpha\beta \Psi_{pump,d} \Psi_{probe,d} \cos(\omega_{pump}t) \cos(\omega_{probe}t)] \\ &= k_d \left\{ \frac{1}{2} \alpha^2 \Psi_{pump,d}^2 [1 + \cos(2\omega_{pump}t)] + \frac{1}{2} \beta^2 \Psi_{probe,d}^2 [1 + \cos(2\omega_{probe}t)] \right. \\ &\quad \left. + \alpha\beta \Psi_{pump,d} \Psi_{probe,d} [\cos((\omega_{pump} + \omega_{probe})t) + \cos((\omega_{pump} - \omega_{probe})t)] \right\} \end{aligned} \quad (25)$$

$$(26)$$

where  $\Psi_{pump,d}$  is the  $d^{th}$  entry in the  $\Psi_{pump}$  vector. Recall that  $d$  is the node at which the nonlinearity is located. Similarly  $\Psi_{probe,d}$  is the  $d^{th}$  entry in the  $\Psi_{probe}$  vector.

Equation (26) shows the genesis of the response at the harmonic and sideband frequencies. The following will focus on only the response at the right sideband frequency,  $\omega_{pump} + \omega_{probe}$ . To understand the response at this frequency, substitute Equation (26) into Equation (23). After separating out the terms that correspond to the right sideband, the last term in Equation (23) becomes:

$$\left[ \begin{array}{c} \Psi \end{array} \right]^T \left\{ \begin{array}{c} 0 \\ \vdots \\ k_d q_d^2 \\ 0 \\ \vdots \end{array} \right\} = [\text{row } d \text{ of } \Psi] (2\alpha\beta k_d \Psi_{pump,d} \Psi_{probe,d}) \cos(\omega_{pump} + \omega_{probe}). \quad (27)$$

Therefore, the response,  $q$ , at the right sideband frequency is:

$$q = \gamma \Psi_{(\omega_{pump} + \omega_{probe}),d} \cos(\omega_{pump} + \omega_{probe}). \quad (28)$$

In Equation (28),  $\gamma$  is a scalar which depends on  $k_d$ , the coefficient of nonlinearity;  $\alpha$ , the magnitude of response at the pumping frequency;  $\beta$ , the magnitude of response at the probing frequency;

$\Psi_{pump,d}$ , how well the pumping force can excite the system at the node where the nonlinearity is;  $\Psi_{probe,d}$ , how well the probing force can excite the system at the node where the nonlinearity is; and the magnitude of response at the sideband frequency.  $\Psi_{(\omega_{pump}+\omega_{probe}),d}$  is the deflection shape at the sideband frequency due to an input force at node  $d$ . Equation (28) shows that the magnitude of the sideband is proportional to the magnitude of the input forces, to the magnitude of response to the input forces, and to the amount of nonlinearity present in the system. It also highlights the importance of the system's linear response at the sideband frequency. In fact, the deflection shape at the sideband frequency when the nonlinearity is present is the same as the deflection shape of the linear system if it was forced at the sideband frequency.

Some of the assumptions made to derive Equation (28) can be relaxed to broaden its interpretation. It was assumed that  $\omega_{pump}$  and  $\omega_{probe}$  were natural frequencies of the system so that it was clear that the response in Equation (24) could be written in terms of the modal vectors. If  $\omega_{pump}$  and  $\omega_{probe}$  are not natural frequencies, the same derivation holds noting that  $\Psi_{pump}$  and  $\Psi_{probe}$  are no longer modal vectors, but deflection shapes which could be decomposed into a linear combination of the modal vectors of the system. The amplitude of the sideband will have the same dependencies as listed above. It was also assumed that nonlinearity was present at only one node. If the nonlinearity is present across several nodes, Equation (27) includes all the rows of  $\Psi$  at which the nonlinearity is present. Equation (28) expands to include the linear combination of deflection shapes due to input forces at all the damaged nodes:

$$q = [\gamma_1 \Psi_{(\omega_{pump}+\omega_{probe}),d_1} + \gamma_2 \Psi_{(\omega_{pump}+\omega_{probe}),d_2} + \dots] \cos(\omega_{pump} + \omega_{probe}). \quad (29)$$

Equation (29) summarizes how changing many of the testing parameters of IM testing affects the sidebands in the response of the system. The amplitude of the sideband depends on the amplitude of the response at the pumping and probing frequencies, on the magnitude and input location of the pumping and probing forces, on the magnitude and location of the nonlinearity, and on the ability of the linear system to respond at the sideband frequency. The deflection shape of the sideband is a linear combination of the deflection shapes at the sideband frequency of the linear system due to input forces at each of the nodes at which a nonlinearity is present.

## Sensitivity Analysis

In the previous section, the equations of motion of the two-beam, one-bolt assembly were manipulated to gain insight into the relationship between different system parameters and the response of the system at the sideband frequencies. In this section, this relationship is further examined by simulating the response of the system, as described in the equations in (19), to IM tests. Like the experimental sensitivity study presented in Chapter 3.1, seven sets of simulations were performed to study how the sidebands in the system response were affected by the amplitude of the impact force, the input location of the impact force, the sensor location, the amplitude of the probing force, the frequency of the probing force, the coefficient of nonlinearity, and the boundary conditions of the system.

Table 1 lists many of the parameters used in the initial simulations. (For a complete list of simulation parameters, see Appendix 5.2.) Some of these parameters were varied during the sensitivity analysis as will be detailed in the following sections. The material and geometric parameters that were used in the simulations were chosen to match the properties of the experimental specimen. Also listed are the values chosen for the bolt parameters. The choice of these values was guided

by [35]. Values for damping and stiffness parameters used to model the boundary conditions are shown. These parameters were chosen by matching the natural frequencies of the model to those found experimentally. Finally, the magnitude and frequencies of the input forces are shown. The probing force used was a single frequency sinusoid with magnitude and frequency as listed. The impact was modeled by interpolating the time history of an impact force measured from a modal impact hammer.

After the system parameters and input forces were defined, Equation (19) was solved using Newmark's method as presented in [54]. The advantages of Newmark's method include its unconditional stability for appropriate choice of parameters and its one step implementation. The discrete Fourier transform was used to convert the solution of Equation (20) into the frequency domain for analysis. As is the case throughout this work, the focus of the analysis is on the generation of the sidebands, which are a result of the nonlinearity in the system.

For each simulation, the following analysis procedure was followed:

1. System parameters were defined as in Table 1. Changes were made as needed based on sensitivity analysis requirements.
2. Input force locations were chosen. One node was selected for the impact location. One node was selected for the probing force input location. These nodes were allowed to coincide.
3. Equations of motion listed in (19) were solved using Newmark's method. (See Appendix 5.2 for full details.)
4. Time data was windowed using a Hanning window and was then transformed into the frequency domain using the Discrete Fourier Transform algorithm in MATLAB.
5. The magnitude or the imaginary part of the acceleration response versus frequency was plotted.
  - Acceleration was used because that is the quantity that was measured experimentally.
  - The magnitude of the transverse response was used for most analyses.
  - In the case where mode shapes were of interest, the imaginary part of the response was used. Shapes were generated using cubic spline interpolation on the transverse acceleration using the rotational acceleration as the slopes at the nodes.
  - Response data was plotted for either all or select nodes depending on the goal of the analysis. The selected nodes for which data was analyzed are the analytical equivalent of the sensor location in the experimental setup.
6. The first four natural frequencies, the magnitude of the response at those four frequencies, the magnitude and frequency of the first four right sidebands, and the magnitude and frequency of the first four left sidebands were identified.

Using the parameters listed in Table 1, the results of the simulation with  $N=10$  (5 nodes per beam) were generated. The impact, probing force input, and sensor locations (i.e. the nodes from which data was analyzed) used for this simulation are shown in Figure 34. The results are shown in Figure 35, and are referred to henceforth as the nominal results. The low frequency data (b)



Table 1: Simulation parameters.

PARAMETER DESCRIPTION	VALUE
<u>Beam Properties</u>	
Length of one beam	.266 m
Young's modulus	69e9 Pa
Cross sectional area	1.2e-4 m
Density	2691 kg/m <sup>3</sup>
<u>Boundary Condition Parameters</u>	
End spring stiffness	3e7 N/m
End damping coefficient	.04 Ns/m
End rotational stiffness	3e7 N/rad
End rotational damping coefficient	.4 Ns/rad
<u>Bolted Joint Parameters</u>	
Linear joint stiffness, $k_{lin}$	6e6 N/m
Joint damping, $c$	.2 Ns/m
Joint rotational stiffness, $k_{\theta}$	6e6 N/rad
Joint rotational damping, $c_{/theta}$	.4 Ns/rad
Nonlinear joint stiffness, $k_{quad}$	-3e6 N/m <sup>2</sup>
Nonlinear joint rotational stiffness, $k_{\theta quad}$	-8e10 N/rad <sup>2</sup>
<u>Input Force Parameters</u>	
Impact force amplitude	200 N
Probing force amplitude	2 N
Probing force frequency	7,500 Hz

shows the peak at the first four natural frequencies: 98 Hz, 318 Hz, 563 Hz, and 1,023 Hz. As was the case for the experimental sensitivity study, only the first four modes of the system will be analyzed here. The high frequency spectrum (c) shows the appearance of sidebands at 7,402 Hz and 7,598 Hz; 7,182 Hz and 7,818 Hz; 6,937 Hz and 8,063 Hz; and at 6,477 Hz and 8,523 Hz. These frequencies correspond to 7,500 Hz, the frequency of the probing signal, plus and minus



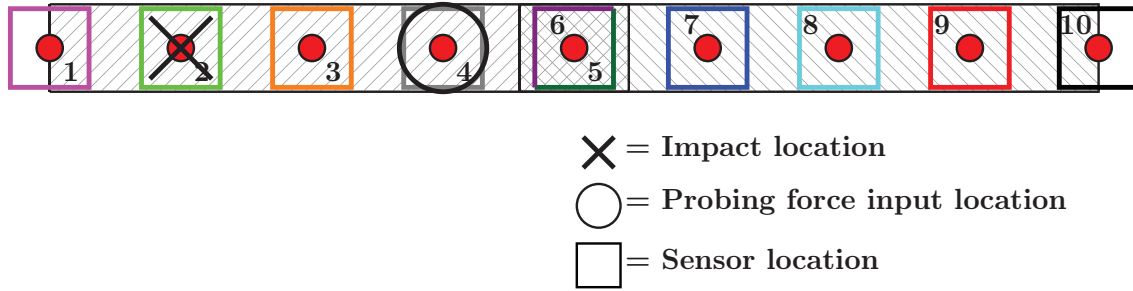


Figure 34: Two-bar schematic showing impact, probing force input, and sensor locations for the nominal case. The color of each square indicates the color that will be used when plotting results from that sensor location.

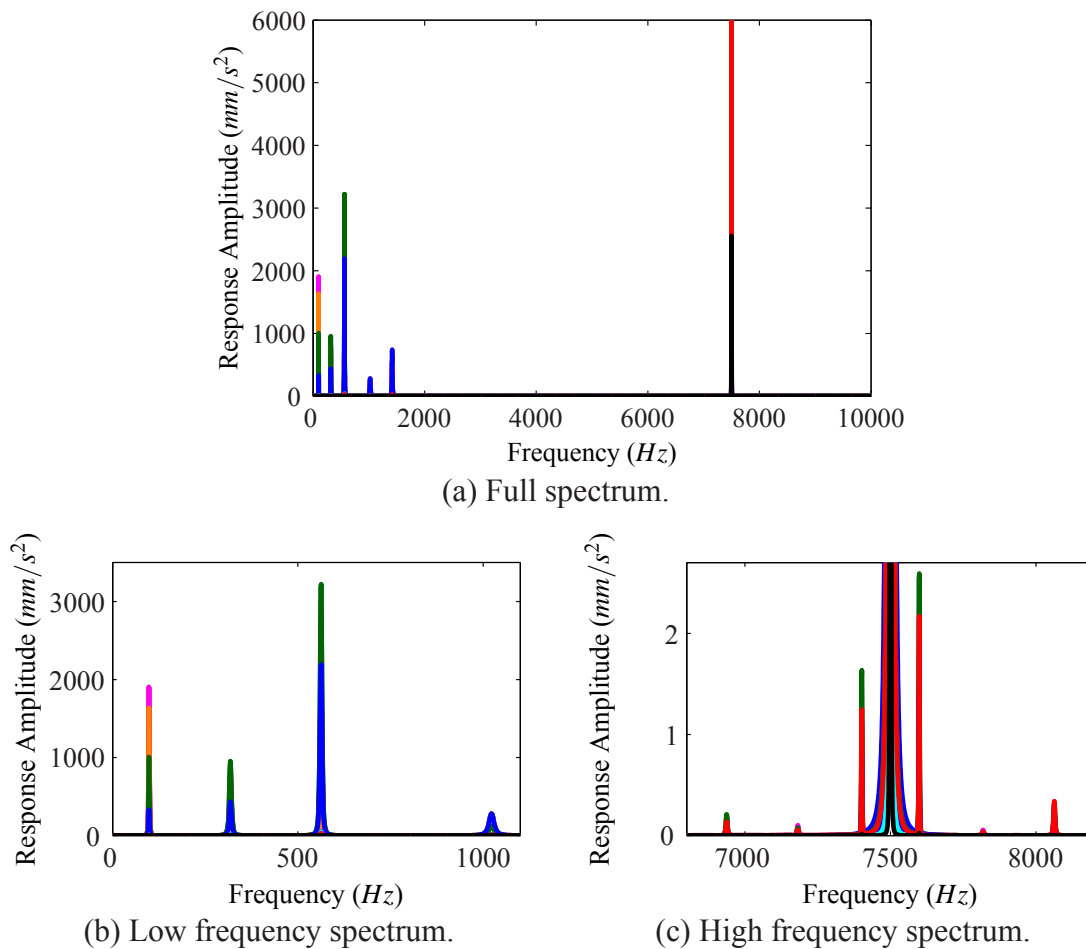


Figure 35: Response spectra from the simulation of an IM test for N=10 (nominal results). Line colors correspond to different sensor locations as indicated in Figure 34.

each natural frequency. Table 2 shows a comparison between the nominal results and the experimental results. The simulated amplitudes used for the comparison were taken from the node that corresponded to the location of the sensor which measured the experimental data. The amplitudes were tuned by adjusting the damping levels using non-proportional damping.

It should also be noted that the frequencies at which the sidebands occurred in the simulation matched those observed in the experimental data. This agreement confirms the use of the quadratic springs to model the nonlinearity in the bolted joint. It was also found that both the nonlinear translational spring and the nonlinear rotational spring were necessary to capture all the nonlinear dynamics observed experimentally. When only a linear quadratic spring was applied in the simulation, only the even modes were modulated in the high frequency range. Conversely, when only a rotational quadratic spring was applied, only the odd modes were modulated. This likely indicates that linear deflections dominate at the joint location for the even modes and rotational deflections dominate at the joint location for the odd modes.

Table 2: Comparison of experimental and simulated results.

Mode	Frequency ( $Hz$ )			Amplitudes ( $mm/s^2$ )		
	EXP	SIM	% Difference	EXP	SIM	% Difference
1	98	98	0.0	3,531	3,648	-3.2
2	366	318	-13.1	2,756	2,733	0.8
3	576	563	-2.2	960	612	56.9
4	958	1,023	6.8	1,096	2,204	-50.3

### Impact Amplitude

The purpose of the first set of simulations performed was to study the relationship between the amplitude of the impact force and the amplitude of the sidebands. It was shown experimentally that the amplitude of the sidebands varies linearly with the amplitude of the impact force used during IM testing. In addition, the theoretical single degree of freedom model presented above also affirms this linear relationship. To further confirm these findings, simulations were performed for eleven impact magnitudes which were equal to a scale factor times the nominal impact force amplitude value that was listed in Table 1. The scale factors used were .1, .25, .5, .75, 1, 2, 4, 6, 8, 10, and 20. The impact, probing force input, and sensor locations were the same as were used in the nominal case. (See Figure 34.) After each simulation, the magnitudes of the left and right sideband which corresponded to each of the first four modes were recorded. These magnitudes were scaled by the magnitude of the sidebands for the nominal case and then plotted as a function of the scale factor of the nominal impact force amplitude, as seen in Figure 36. Clearly, the sideband amplitudes grow linearly with the amplitude of the impact force in agreement with the experimental data presented in Section 3.1.2 and with the previous analytical findings.

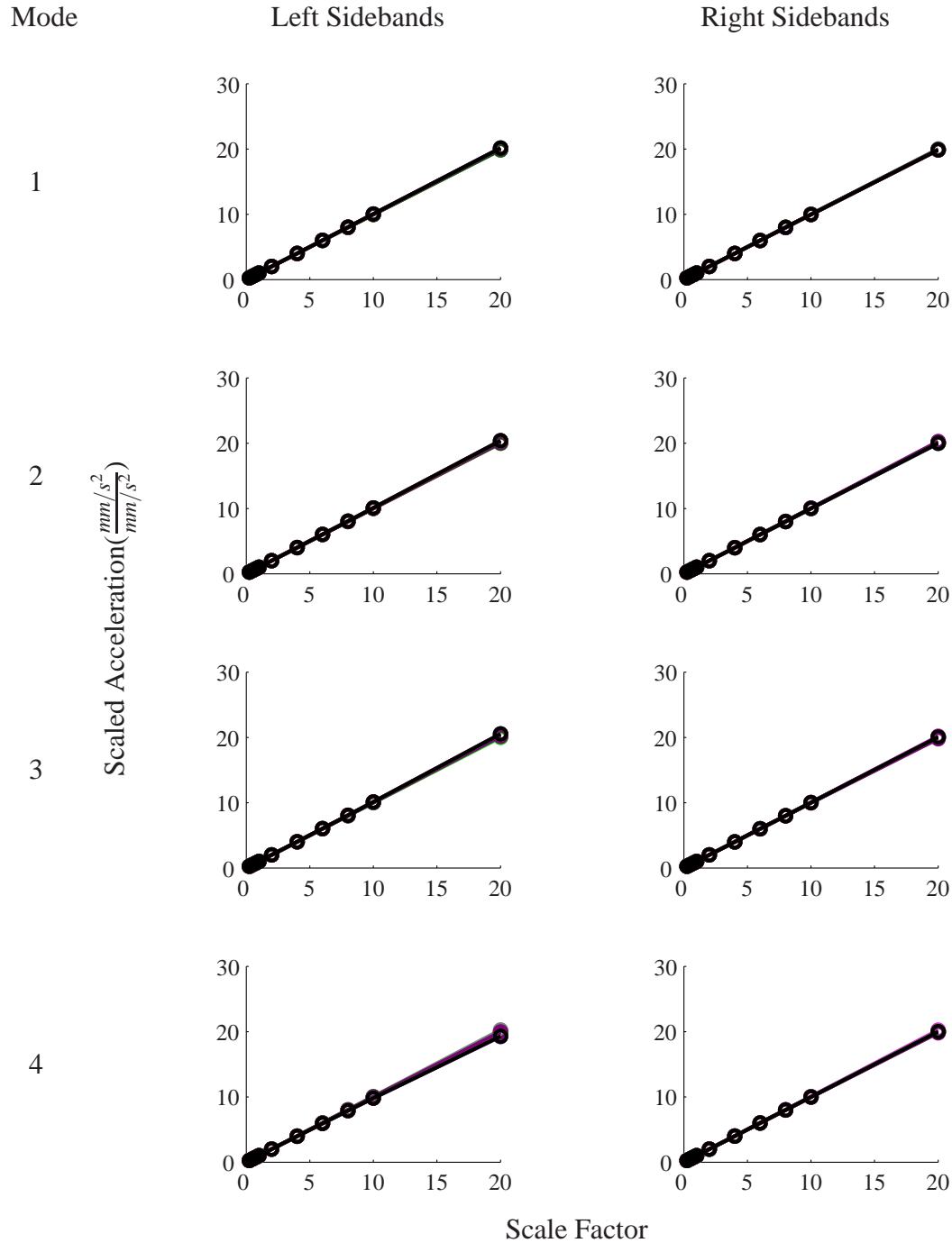


Figure 36: Scaled left and right sideband amplitudes corresponding to the first four modes versus scale factor of impact amplitude from IM simulations. Line colors correspond to different sensor locations as indicated in Figure 34.

### Impact Location

The second set of simulations addressed the effect of the impact force location on the sideband amplitudes. Ten simulations were performed each with a different node chosen as the impact force input location. Figure 37 shows the impact, probing force input, and sensor locations. The

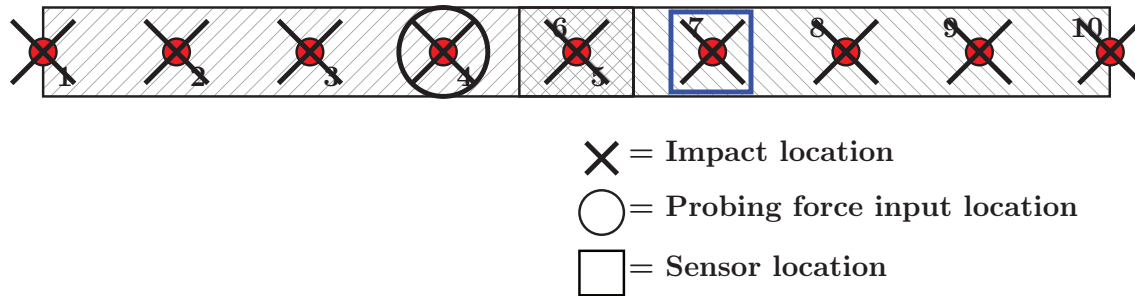


Figure 37: Two-bar schematic showing impact, probing force input, and sensor locations for the impact location study.

experimental impact location tests as well as the analytical analyses presented in the previous sections showed that the change in the amplitude of the sidebands due to a change in the impact location should mirror the change in amplitude of the response at the natural frequency. Figure 38 shows the modal response and the amplitude of the imaginary part of the response at the right and left sideband frequencies for each of the ten impact locations for data measured at node (i.e. sensor location) 7. The amplitudes of the imaginary part of the modal and sideband responses for each mode were normalized by the length of the vector which contained the respective response amplitudes for all impact locations. Node 7 was chosen because that was the location of the sensor used in the experimental work. The results from node 7 are also representative of the results from the other nodes. As in the experimental results presented in Section 3.1.2, the shape generated by plotting the imaginary part of the sideband responses versus the impact location along the beam mirrors the mode shape at the corresponding natural frequency. This relationship will be important to the work presented in the next chapter regarding the detection of the loose bolt without a prior knowledge.

### Sensor Location

The experiments conducted to investigate sensor location presented in Section 3.1.2 did not result in any definitive conclusions about the relationship between sensor location and the amplitudes of the sidebands measured by those sensors. Therefore, the results of the simulations which studied sensor location are of particular interest. Only one simulation was required for this investigation, and the parameters used in that simulation are the same as those used to generate the nominal results, seen in Figure 34. The imaginary part of the left and right sideband responses for each of the first four modes was recorded for each of the ten nodes of the finite element model. Those amplitudes are plotted as a function of node (sensor) location as measured along the beam in Figure 39. These plots represent the deflection shapes of the beams at the sideband frequencies. The deflection shapes at the first four natural frequencies are also shown for reference. Just as in the experimental data, the simulated data show that there is no obvious correlation between the deflection shapes at the sideband frequencies and the corresponding mode shape.

In the analysis of the equations of motion presented in Section 3.2.2, it was shown that the deflection shape of the beam at a given sideband frequency is not the same as the mode shape but is the deflection shape the beam would experience when subjected to an excitation at the sideband frequency. For example, the first right sideband in the simulated data occurs at 7,598 Hz. The

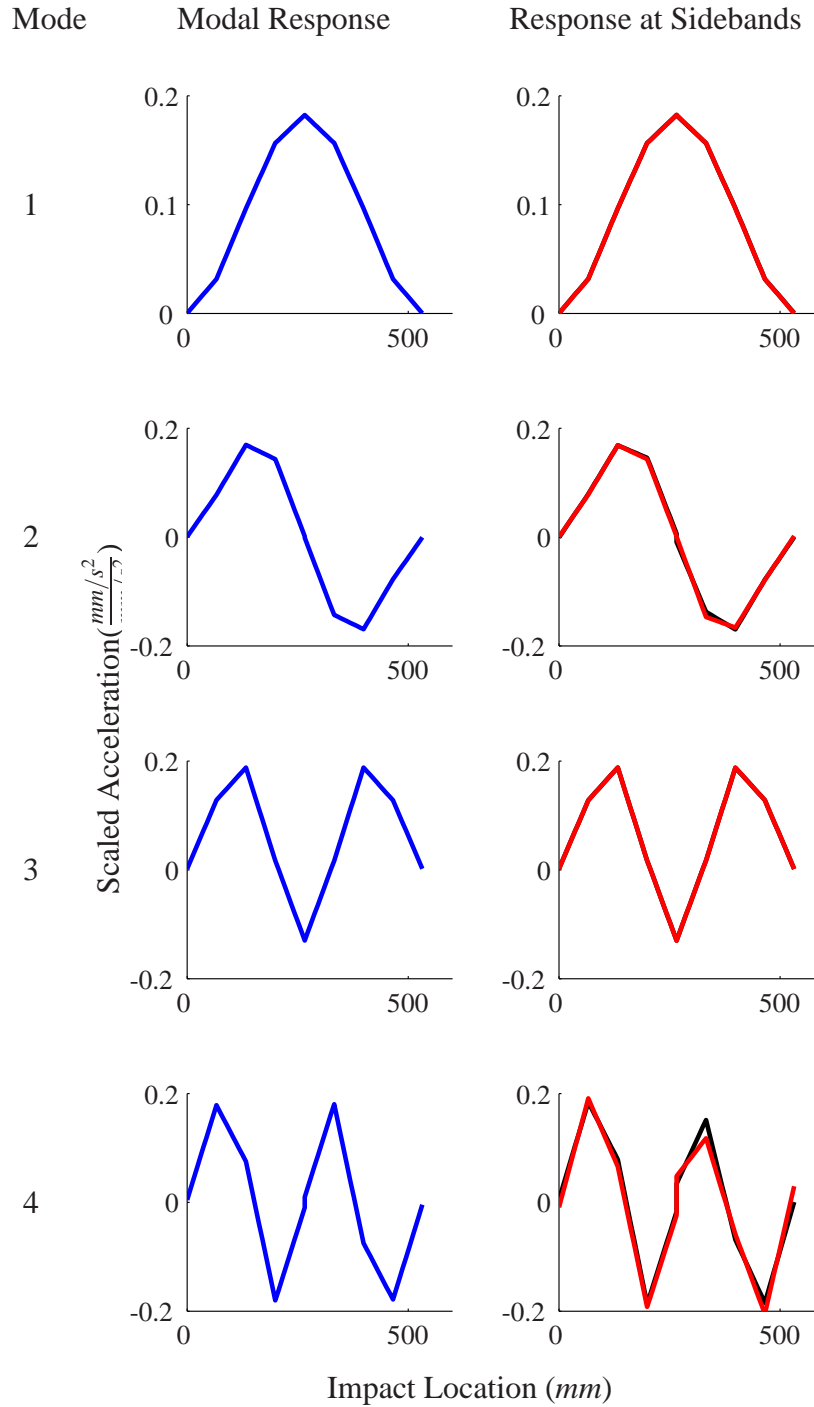


Figure 38: Scaled imaginary part of the response versus impact location as measured along the beam from IM simulations measured at sensor location 7 for the modal response (—) and for the left (—) and right (—) sidebands.

deflection shape for the sideband at 7,598 Hz is shown in Figure 40(a). (This shape is also shown in Figure 39 but is repeated here for clarity.) The equations of motion indicate that this shape

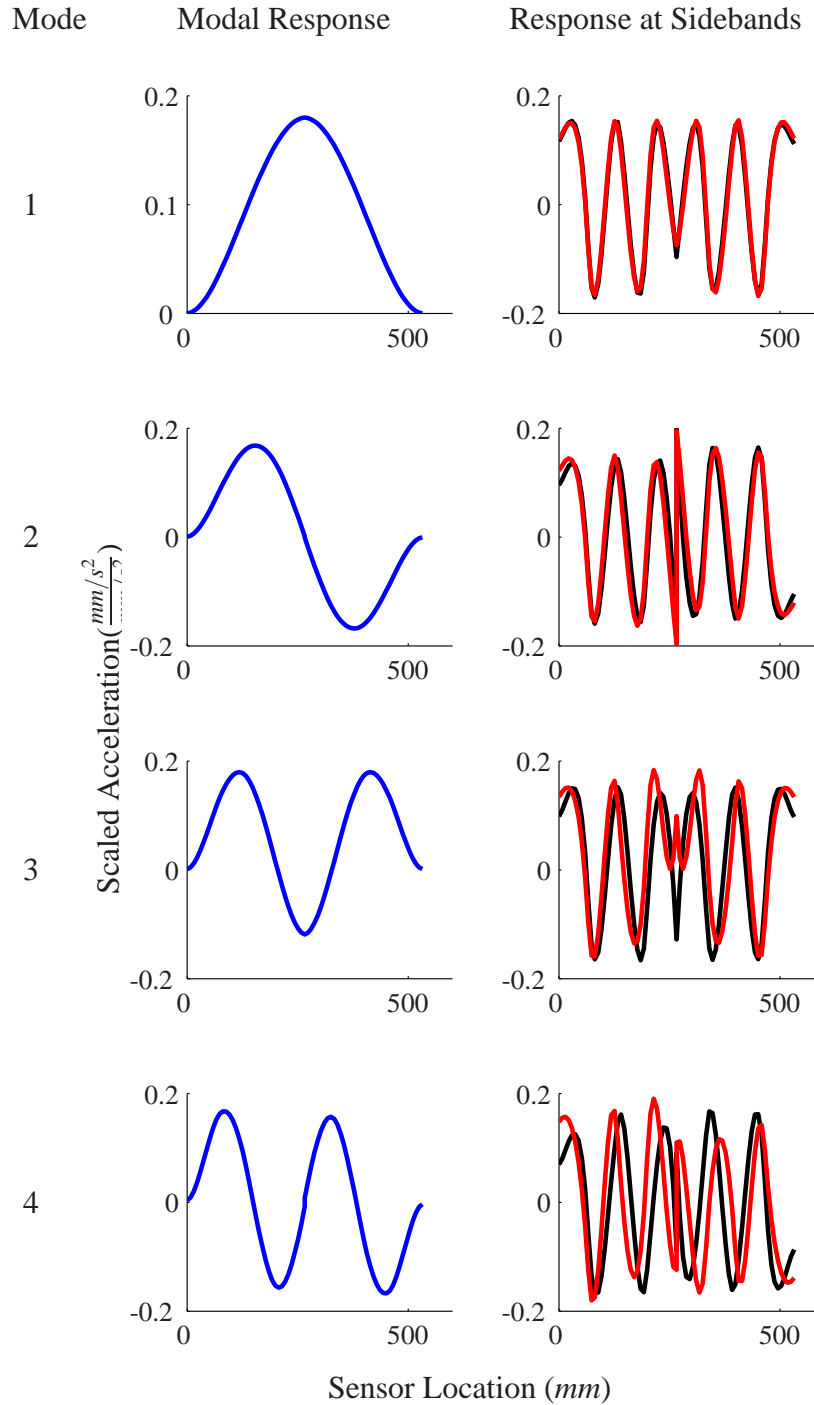


Figure 39: Scaled imaginary part of the response versus sensor location as measured along the beam from IM simulations as measured at sensor location 7 for the modal response (—) and for the left (—) and right (—) sidebands.

should match the deflection shape of the beams when excited by a single-frequency excitation at 7,598 Hz. This shape, henceforth referred to as the underlying deflection shape at the sideband

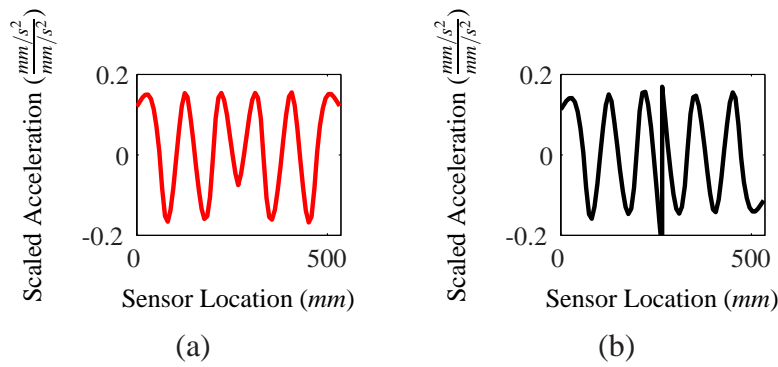


Figure 40: (a) First right sideband deflection shape (7,598 Hz) and (b) underlying deflection shape at 7,598 Hz.

frequency, was generated by running the simulation using a 7,598 Hz sinusoidal excitation with no impact and is shown in Figure 40(b). Although there appears to be some correlation between these shapes, they are not an exact match. Therefore, to this point, it is still unclear which modes are contributing to the operating shape at the sideband frequencies in the beam's response to IM testing.

In [51], Yoder and Adams used a dot product analysis to try to identify which modes contributed to the deflection shape of at the sideband frequencies in the response of a cracked beam to Vibro-Acoustic Modulation (VM) testing. The procedure they used for the dot product analysis was to find the dot product between the deflection shape at the sideband frequency and the deflection shapes at other relevant frequencies such as the natural frequency and the actuator frequency. The dot products were normalized by the lengths of each of the deflection shape vectors so that the result was a number between zero and one. Dot products close to one indicated a greater degree of correlation between the two shapes than a dot product near zero. This procedure was applied to the simulation data in an effort to identify which modes were most contributing to the deflection shape of the bolted beams at the sideband frequencies generated from IM testing. In Figure 41, the dot products between the deflection shapes at the sideband frequencies,  $SB_R$  and  $SB_L$ , with the mode shape,  $M$ , the deflection shape at the probing force frequency,  $A$ , the pointwise multiplication of  $M$  and  $A$ , the underlying deflection shapes at the sideband frequencies,  $U_L$  and  $U_R$ , and the deflection shapes at the sidebands themselves for the first four modes are shown. The dot product will take on a value of one when  $SB_L$  is dotted with itself and when  $SB_R$  is dotted with itself. The pointwise multiplication of  $M$  and  $A$  was included in the analysis because Yoder and Adams found that this shape correlated well with their sideband deflection shapes.

Clearly, the results are not consistent across the four modes. In all cases, the correlation between the sideband deflection shapes and both the mode shapes,  $M$ , and the pointwise multiplication between  $M$  and  $A$  are low, and, except for the left sideband deflection shape for mode 4, the left and right sidebands show strong correlation with each other. In addition, the results from mode 1 show some correlation between the sideband deflection shapes and the underlying deflection shape at the left sideband frequency. Mode 2 shows the sideband deflection shapes correlate well with the underlying deflections shapes and the shape at the probing force frequency. Mode 3 only shows weak correlation with the underlying shape at the right sideband frequency. Finally, mode 4 shows that the sideband deflection shapes have strong correlation to the underlying deflec-

tion shapes. Overall, the results are not consistent enough to make a definitive conclusion about which modes contribute to the deflection shapes at the sideband frequencies. There is evidence that the underlying deflection shapes at the sideband frequencies do have an affect. The results do show conclusively that the mode shape and the pointwise multiplication between the mode shape and the deflection shape at the probing force frequency to not correlate well with the sideband deflection shapes.

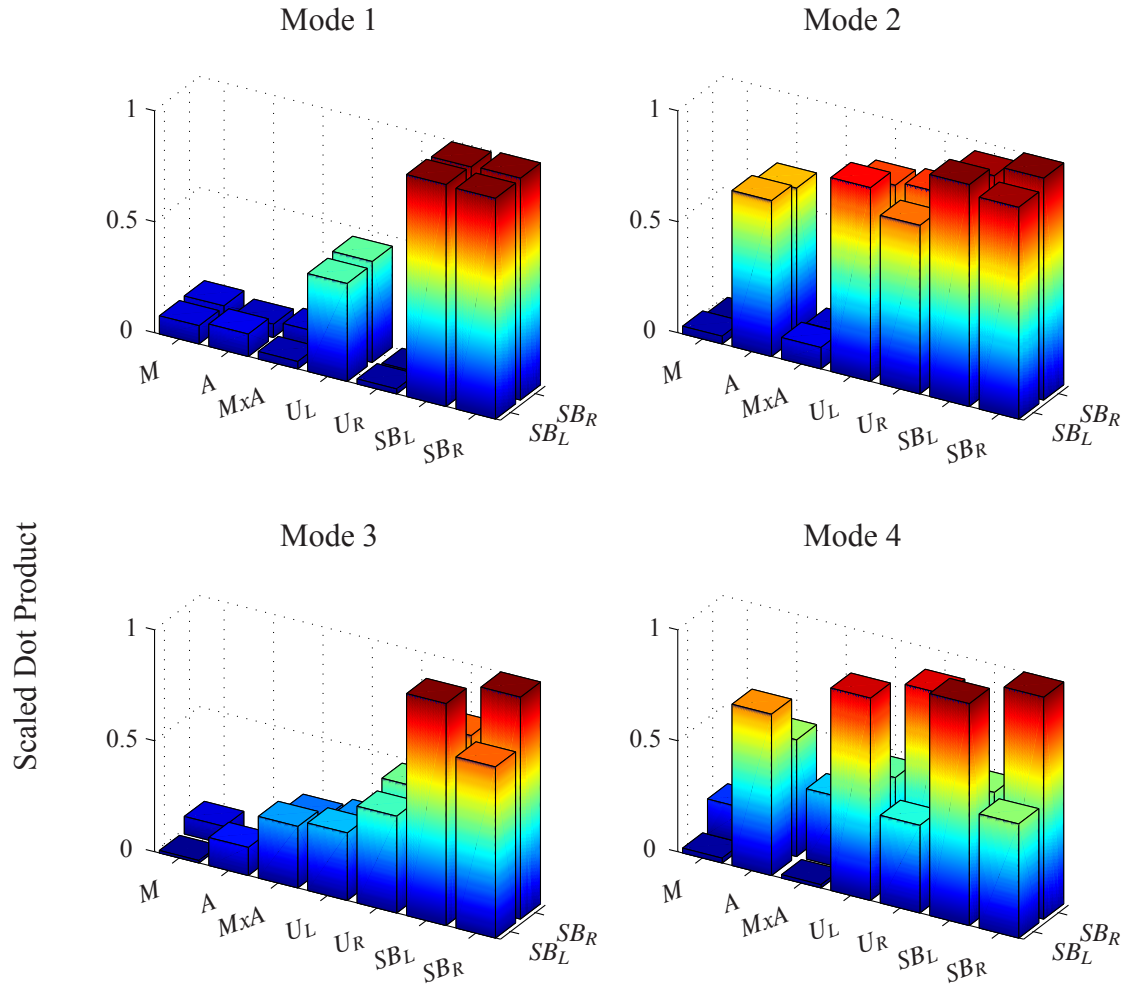


Figure 41: Scaled dot product between the left ( $S_{BL}$ ) and right ( $S_{BR}$ ) sidebands and the mode shape ( $M$ ), the deflection shape at the probing force frequency ( $A$ ), the pointwise multiplication of  $M$  and  $A$  ( $M \times A$ ), and the underlying deflection shapes ( $U_L$  and  $U_R$ ) for each of the first four modes.

### Probing Force Amplitude

The next set of simulations was aimed at studying the relationship between the amplitude of the probing force and the magnitude of the sidebands. The single degree of freedom model analysis and the finite element model analysis predict that this relationship is linear. The experimental results showed a nonlinear trend in the data. (See Figure 15.) Eleven simulations were performed



using different probing force magnitudes which were equal to a scale factor times the nominal probing force amplitude value that was listed in Table 1. The scale factors used were .1, .25, .5, .75, 1, 2, 4, 6, 8, 10, 20. The value of all other parameters were the same as in the nominal case. After each simulation, the magnitudes of the left and right sideband which corresponded to each of the first four modes were recorded. These magnitudes are shown in Figure 42 as a function of the scale factor of the nominal impact force amplitude. It is clear that the sideband amplitudes grow linearly with the amplitude of the probing force. Because the theoretical models presented in this chapter all point to the sideband amplitudes varying linearly with the amplitude of the probing force, it is likely that either some other variation is causing the experimental results not to exhibit the same behavior or that the analytical models have made a simplifying assumption, such as using linear damping, that is breaking down. This investigation will be left for future work.

### **Probing Force Frequency**

As in the experimental sensitivity study, two different probing force frequencies were investigated to study what effect a change in this frequency would have on the amplitudes of the sidebands. Two simulations were performed, one using a probing force frequency of 7,500 Hz and one using a frequency of 10,510 Hz. These frequencies were chosen to match the frequencies used in the experimental work presented in Section 3.1.2. The amplitudes of the first four left and right sidebands were identified for each of the two tests. Figure 43 shows these amplitudes as a function of frequency. As was the case with the experimental data, the simulation data shows that the amplitudes of the sidebands associated with the 7,500 Hz probing force frequency are much smaller than those associated with the 10,510 Hz frequency. It was concluded from the experimental data that the reason for this discrepancy was that the linear response of the two-beam assembly was of greater magnitude at the frequencies surrounding 10,510 Hz than near 7,500 Hz. To verify this conclusion, the response of the finite element model to a sine sweep from 6,000 Hz to 12,000 Hz was performed. That response, shown in black, is shown in Figure 44 along with the sideband amplitudes from Figure 43, shown as red circles. The larger sideband amplitudes from the test using a probing force frequency of 10,510 Hz can be explained by the increase in the magnitude of the underlying linear response. The simulated results match very well with the experimental results.

### **Coefficient of Nonlinearity**

In the experimental sensitivity study, a change in bolt torque simply meant loosening or tightening the bolt. Modeling a change in bolt torque in the finite element model was a bit more complicated. The experimental results presented in Section 3.1.2 confirmed the assumption that is maintained throughout this work that a decrease in the torque on the bolt leads to an increase in nonlinearity in the structure which manifests as an increase in the sideband amplitudes measured during IM testing. Guided by that assumption, modeling a decrease in bolt torque was assumed to be equivalent to increasing the amount of nonlinearity present in the system. There are two ways to achieve an increase in nonlinearity in the finite element model. The first is to simply increase the magnitude of the coefficient of the nonlinear spring at the bolted interface. The second is to decrease the coefficient of the linear spring at the bolted interface. By decreasing the linear stiffness but keeping the nonlinear stiffness the same, the portion of the total stiffness attributed to the nonlinear stiffness increases.

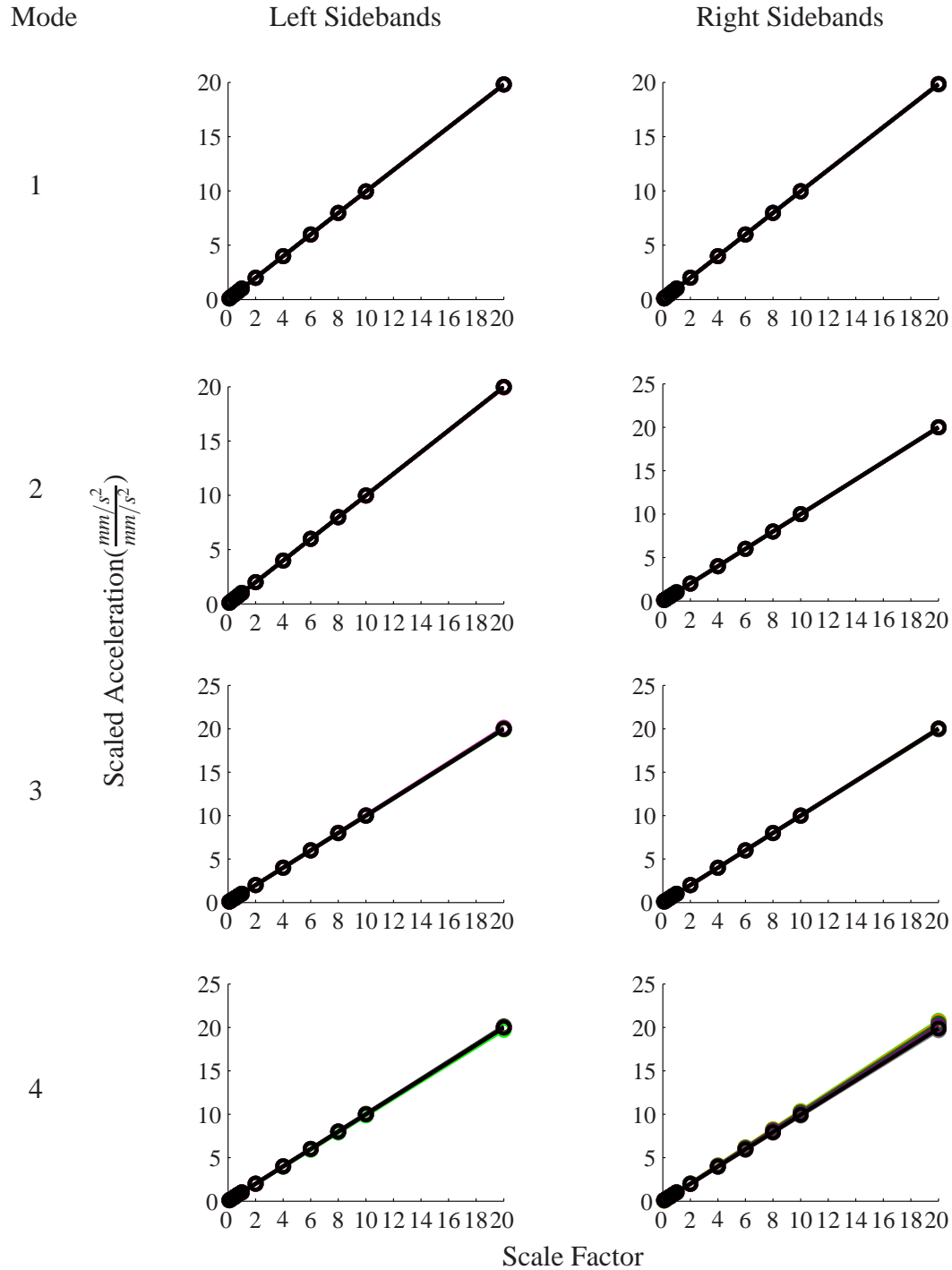


Figure 42: Scaled left and right sideband amplitudes corresponding to the first four modes versus scale factor of probing force amplitude from IM simulations. Line colors correspond to different sensor locations as indicated in Figure 34.

In order to determine which of these two modeling approaches best matched the experimental results, two sets of simulations were performed. For the first set, the simulation was repeated eleven times using a coefficient of the quadratic spring ( $k_{quad}$ ) and the coefficient of the quadratic

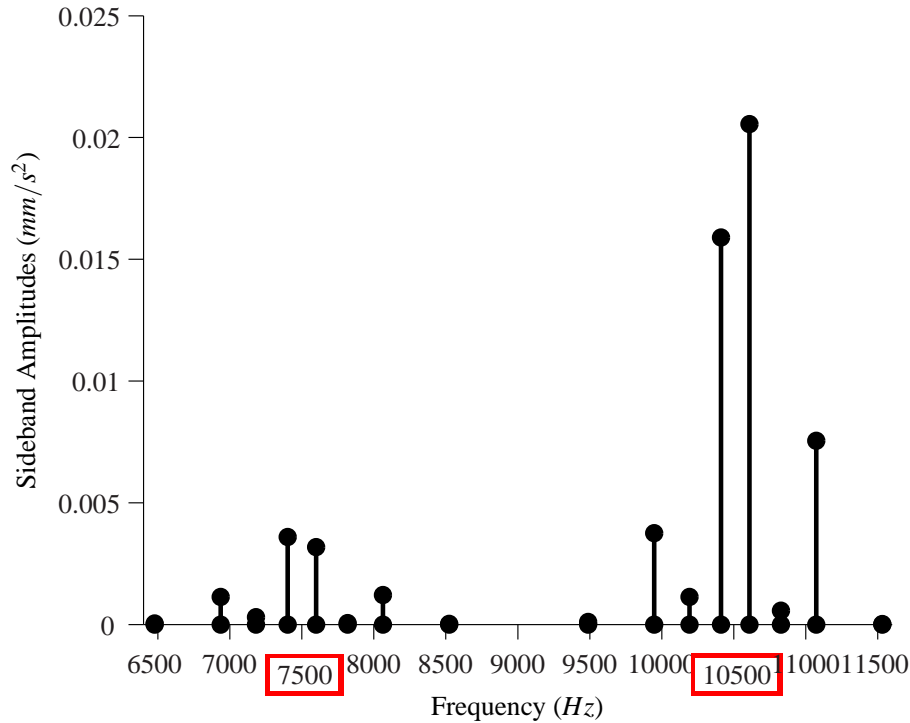


Figure 43: Sideband amplitudes from simulated IM tests using an actuator frequency of 7,500 Hz and 10,510 Hz.

rotational spring ( $k_{\theta quad}$ ) equal to a scale factor times the nominal quadratic spring coefficient value that was listed in Table 1. The scale factors used were .1, .25, .5, .75, 1, 2, 4, 6, 8, 10, 20. The magnitudes of the first four left and right sidebands were recorded after each simulation. Figure 45 shows these amplitudes, after scaling by the respective sideband amplitudes from the nominal results, as a function of the scale factor. The increase in the sideband amplitudes due to an increase in the magnitude of the coefficient of the quadratic spring clearly exhibits a linear trend. This is unlike the trend seen in the experimental results, which was nonlinear. (See Figure 23.)

Next, a second set of simulations was performed in which the coefficient of the linear spring at the bolted joint was varied. Note that the coefficients of the nonlinear springs were held constant. Like the previous set of simulations, eleven simulations were performed using a linear spring coefficient ( $k_{lin}$ ) and the linear rotational spring coefficient ( $k_{\theta lin}$ ) equal to a scale factor times the nominal linear spring coefficient value that was listed in Table 1. The scale factors used were the same as above: .1, .25, .5, .75, 1, 2, 4, 6, 8, 10, 20. Figure 46 shows that varying the linear spring coefficient has a drastically different effect than varying the nonlinear spring coefficient. In addition, these trends more closely match those seen experimentally in Figure 23. Modes 2 and 4 show the same flattening out of the response as seen in experimental data. It is also important to note that the decrease in linear stiffness at the bolted interface had little effect on the natural frequencies of the system. This is consistent with the experimental results.

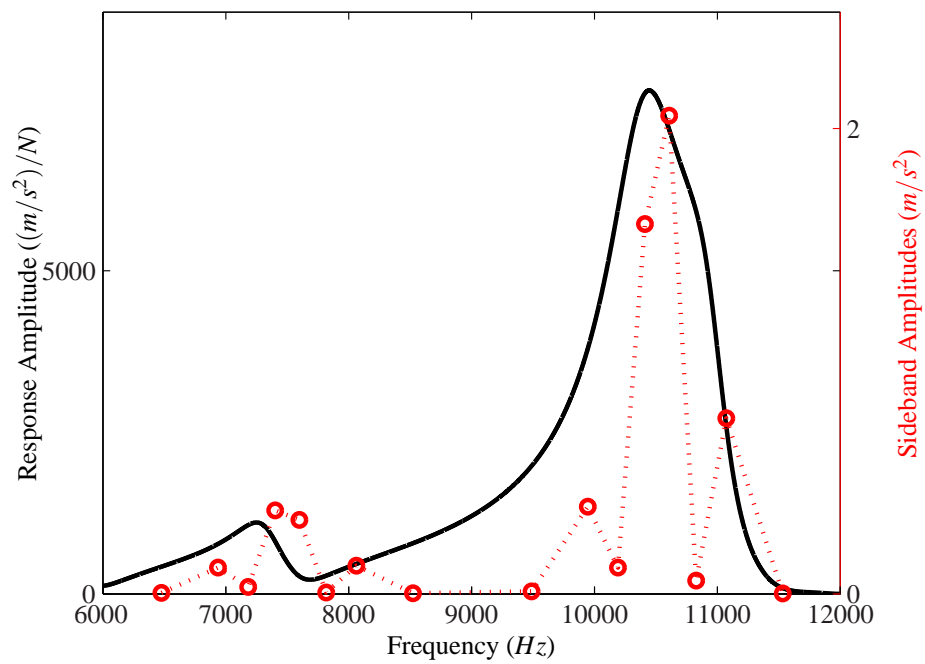


Figure 44: Frequency response function of the two-beam assembly when subjected to a simulated sine sweep (—) and sideband amplitudes from Figure 43 (○).

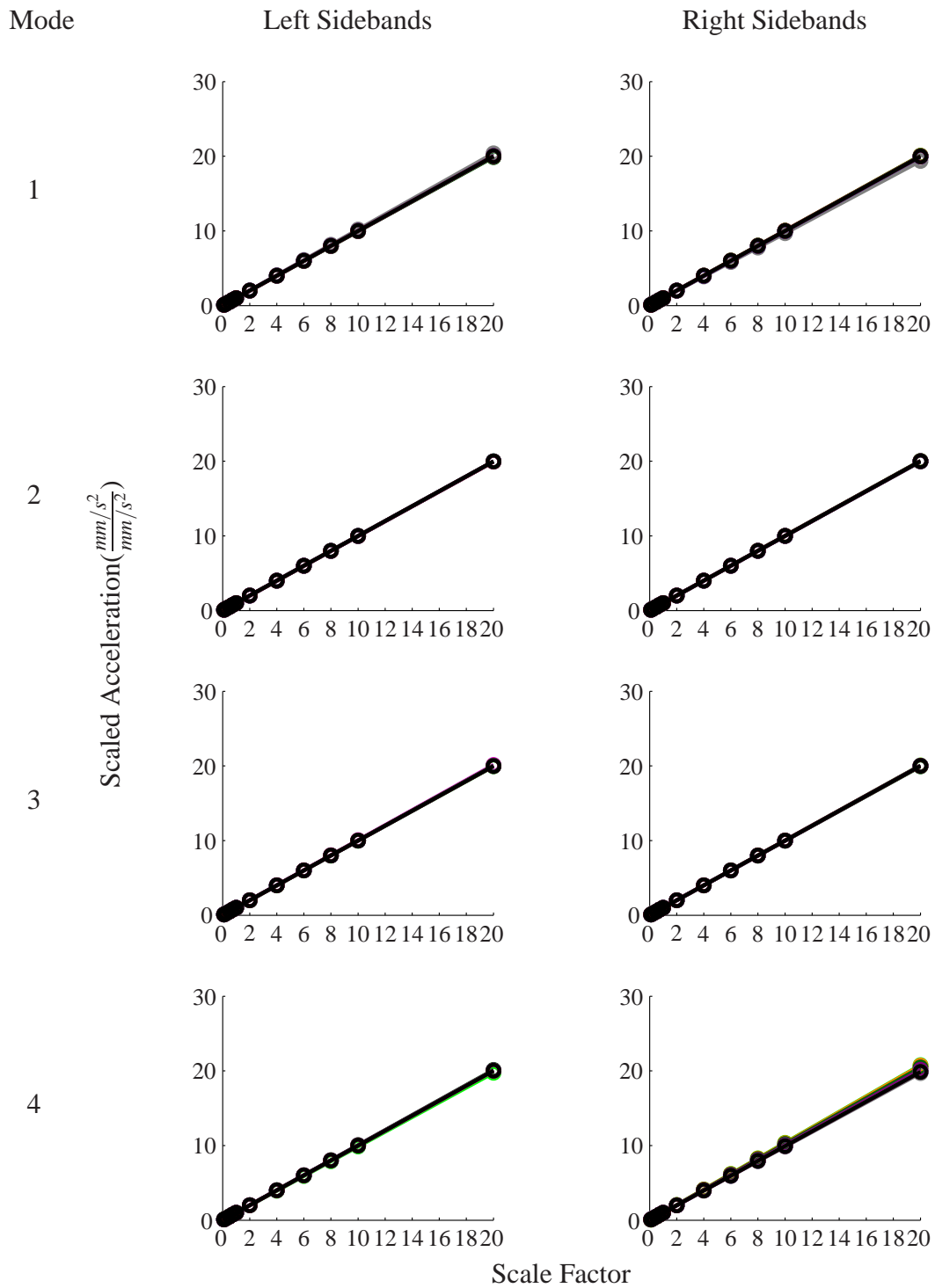


Figure 45: Scaled left and right sideband amplitudes corresponding to the first four modes versus scale factor of coefficients of nonlinear springs at the bolted joint from IM simulations. Line colors correspond to different sensor locations as indicated in Figure 34.

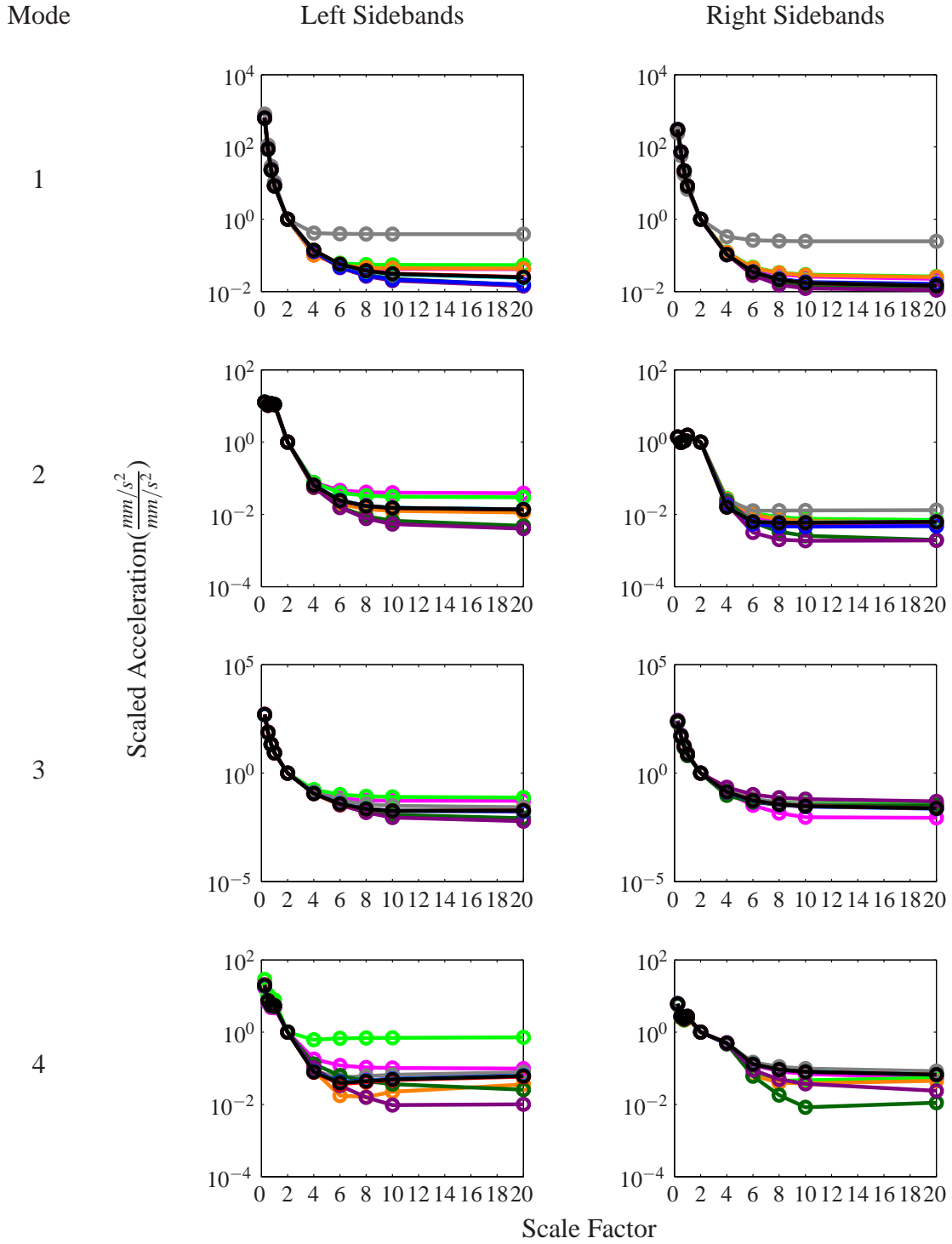


Figure 46: Scaled left and right sideband amplitudes corresponding to the first four modes versus scale factor of the coefficients of the linear springs at the bolted joint from IM simulations. Line colors correspond to different sensor locations as indicated in Figure 34.

During the experimental analysis, the next step was to synthesize the data from each of the four modes into one modulation index using an integration technique that calculates a normalized area under the response spectrum over the sideband frequency ranges. This technique, which was outlined in Section 3.1.2, was applied to the second set of simulation results described above in which the coefficient of the linear spring was varied. Figure 47 shows the modulation indices as a function of the scale factor which varied the linear spring stiffness. The trend seen in this plot matches very well with the trend seen experimentally in Figures 26 and 27.

The results presented in this section indicate that changes in IM results seen experimentally due to a change in bolt torque are best modeled as changes in the linear stiffness at the bolted interface. This conclusion will be important in the next chapter where the techniques for detecting the loose bolt will be analytically modeled.

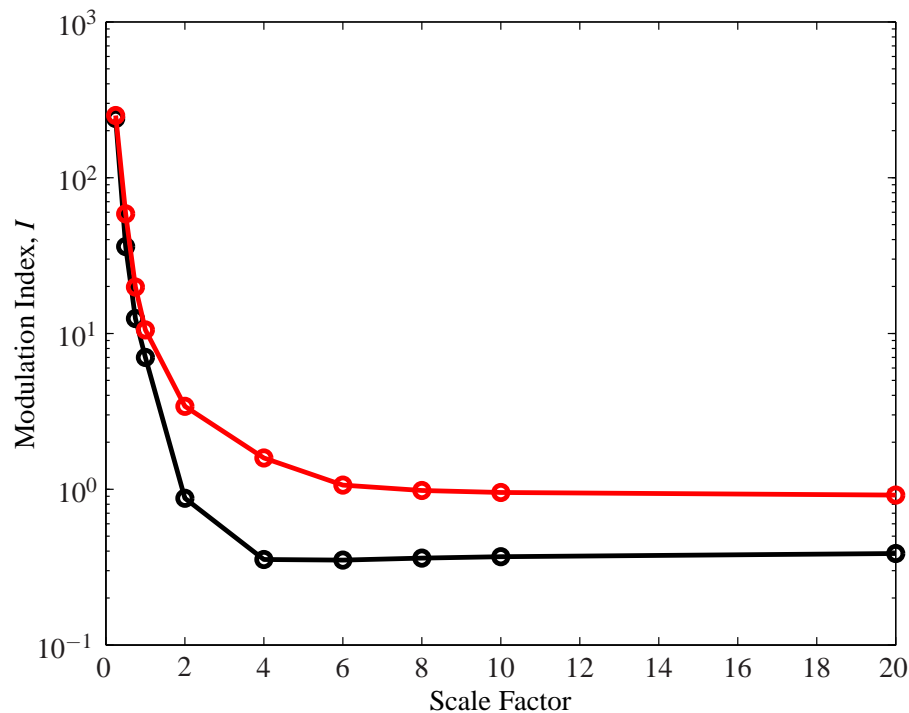


Figure 47: Normalized area under the the response spectrum over the left (—) and right (—) modulation spectra versus scale factor of the coefficients of the linear springs at the bolted joint for IM simulations with fixed boundary conditions.

### Boundary Conditions

The final set of simulations that was performed addressed the effects of changing the boundary conditions. Up to this point, fixed boundary conditions have been modeled by choosing relatively high spring coefficients for the end springs at the first and last nodes. To model the free boundary conditions used in the experimental work, which were achieved by hanging the two-beam assembly from fishing line, the end spring coefficients were lowered until the natural frequencies matched. Both translational end spring coefficients were changed to 30 N/m and both rotational end spring coefficient were changed to 30 N/rad. Then the same set of eleven simulations, described in detail

in the previous section, in which the coefficient of the linear spring at the bolted interface was varied was performed. Again, the integration technique described in Section 3.1.2 was applied to the data, and Figure 48 shows the results. The same trend seen with the simulated fixed boundary conditions is evident in the results for the data generated using free boundary conditions. In addition, the trend matched that seen experimentally, as was shown in Figure 30.

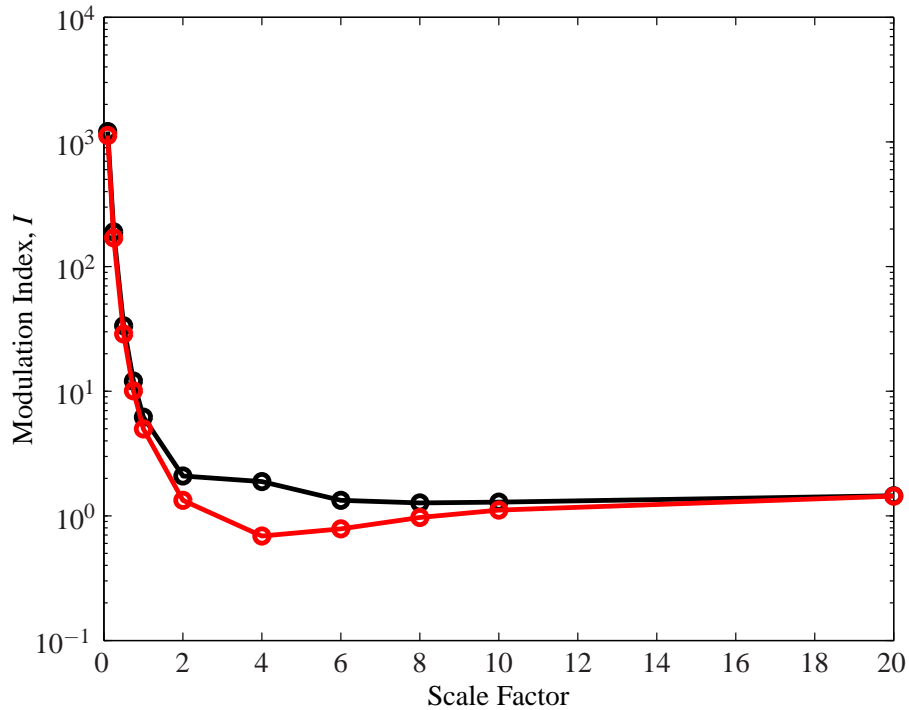


Figure 48: Normalized area under the the response spectrum over the left (—) and right (—) modulation spectra versus scale factor of the coefficients of the linear springs at the bolted joint for IM simulations with free boundary conditions.

### 3.3 Conclusions

The goal of this chapter was to explore IM testing from an analytical perspective. A single degree of freedom model was used to develop a theoretical basis for the application of IM to structures with bolted joints. In addition, the equations of motion for a finite element model of the two-beam, one-bolt structure were analyzed. Both of these models showed the amplitude of the sidebands in each respective solution are proportional to the amplitude of the impact force, the amplitude of the probing force, and the amount of nonlinearity present in the system. The analysis of the equations of motion of the finite element model also highlighted the dependence of the sideband amplitudes on the impact location, the sensor location, and on the underlying linear dynamics of the system at the sideband frequencies.

To further illustrate these dependencies, results from a sensitivity study, which paralleled the experimental study presented in Chapter 3.1, were presented. It was found that the effects of the impact amplitude, impact location, probing force frequency, and boundary conditions on the



simulation data matched those seen experimentally. Further work is needed to understand the factors which contribute to the operating shape at the sideband frequencies, which was highlighted in the analysis of sensor placement. By comparing the simulation results with the experimental data, it was found that modeling a change in bolt torque is best achieved by reducing the linear bolt stiffness at the joint. This conclusion will be important in the next chapter, where an analysis method for detecting loose bolts without a priori knowledge is modeled.

At this point, IM has been shown by both experimental and analytical data to be a viable method to detect loose bolts in a structure. The remainder of this work will now focus on developing an analysis method, rooted in the conclusions drawn above, to use the amplitudes of the sidebands produced during IM testing to diagnose the condition of the bolts within a structure.

## 4.0 RESULTS AND DISCUSSION

### 4.1 Using Impact Modulation for the History-Free Detection of Loose Bolts

In the previous chapters, the foundation for using Impact Modulation (IM) to detect loose bolts was established. Data from both the analytical models and the experimental sensitivity study showed trends which correlate well with changes in the torque on the bolt within the structure. As mentioned in 2.3.3, literature shows that finding trends in data from IM or the similar method of Vibro-Acoustic Modulation, VM, which correlate to increasing levels of damage due to cracks in various materials has been repeatedly accomplished in works such as [42], [45], [16], and [4]. However, few researchers have been able to solve the inverse problem: detecting damage without a priori knowledge. The goal of the work presented in this chapter is to establish a history-free analysis method that can detect a loose bolt without access to any previously collected results or baseline data. The development of this analysis method will be explained in detail and the results for a three-beam, two-bolt structure; a four-beam, three-bolt structure; and a complex satellite structure will be presented.

**4.1.1 Method for Loose Bolt Detection.** Because the final application of the method to detect loose bolts is to be used on quickly-built, modular satellites, several criteria for the method must be met including not having to rely on baseline data from experimental or analytical analysis. Therefore methods like those presented by Duffour et al. [50] and Johnson et al. [52] which derive a damage index that is a comparison of the amount of modulation present in the response of a damaged specimen to the amount present in the response of a healthy specimen were not considered. Other methods for detecting damage using IM or VM were reviewed for possible application to detecting bolted joints. In [51], Yoder et al. used extreme value statistics to evaluate when sidebands were present which, for that particular application, was an indication that damage was present. The underlying assumption for that method was that the healthy structure was nearly linear and, therefore, its response did not exhibit strong sidebands when subject to IM testing. Because bolted joints, even with proper bolt torque, are nonlinear, this assumption cannot be made and, therefore, this method was not effective. Another method found in the literature to detect damage without the use of baseline data is to compare the results of tests that use different input force amplitudes. Both Van Den Abeele et al. [55] and Underwood et al. [56] performed vibration-based tests at two distinct levels of input force amplitudes and then compared the results. The assumption made during the analysis was that if the structure was linear (not damaged) the increase in the response due to the increase in excitation amplitude would be linearly related. If the structure was damaged, that linear relationship would break down. This approach was applied to the IM testing of the bolted structure by performing IM using two distinct impact levels and tracking the change in sideband amplitudes, but was not effective. As was shown in Section 3.1.2, the amplitudes of the sidebands grow linearly with increasing impact amplitude. This relationship held even for very loose bolts.

One of the most prominent techniques found in the literature for detecting damage using IM or VM is to define a damage index based on a relationship between the sideband amplitudes and the amplitude of response at the actuator frequency. Amerini and Meo [16] defined a damage index as the difference between the response at the actuator frequency and the average amplitudes of the first right and left sidebands. Although the method was effective, in order to establish a threshold for when the index indicates a loose bolt, they had to repeat the tests for multiple torque levels.

Donskoy [4] used the ratio of the sideband amplitude to the amplitude of response at the actuator frequency. But, like many of the results presented in the literature, the evaluation of whether the structure was healthy or damaged was "mostly qualitative" [4].

In [57], Pandey et al. were able to detect cracks in both a cantilever beam and a simply supported beam by comparing the curvature mode shapes from the damaged beam with those of a healthy beam. Pandey et al. defines a curvature mode shape as the derivative of the mode shape. To avoid confusion, the more mathematically appropriate term "slope" will be used in place of "curvature" in this work. This method cannot be applied directly to detecting loose bolts because, as stated above, data from a healthy specimen, i.e. a structure whose bolts are all torqued correctly, will not be available. However, as presented in Section 3.1.2, by making impacts along the length of the beam, the amplitude of the imaginary part of the sidebands mirrored the shape of the corresponding linear mode shape. Therefore, for each IM test, the linear mode shape can be approximated in two ways. First, as is the standard procedure for modal analysis, the amplitude of the imaginary part of the response at the natural frequency can be measured for each of the impacts made along the beam. The mode shape is approximated by plotting these amplitudes as a function of impact location. Second, the amplitude of the imaginary part of the sidebands can be plotted as a function of impact location to give another approximation of the mode shape. This phenomenon was illustrated in Figure 10. The ability to approximate the same mode shape from two features of the same data set presents the possibility that the correlation between the slope of the two approximated mode shapes could be used as a damage index.

Initial tests were performed on a three-beam, two-bolt structure, which will be described in detail later, to investigate the effectiveness of using this correlation as an indication that loose bolts were present in structure. It was found that picking the peaks of the imaginary part of the response at the sideband frequencies with the proper sign across impact locations was difficult from a data processing standpoint. Therefore, to ease the data processing, the magnitude of the response was analyzed instead. It is important to note that using the magnitude of the response means that the mode shapes are no longer being analyzed, rather the change in the amplitude of response across impact locations is being analyzed. During this initial testing, it was qualitatively noted that when the bolts were tight, the amplitude of the response at the natural frequency across impact locations correlated very well with the amplitude of response at the sideband frequencies across the impact locations. However, while the shape of the response at the natural frequency showed little change when one of the bolts was loose, the shape of the response at the sideband frequencies changed dramatically. An example of this phenomenon is shown in Figure 49.

In order to develop an index to identify the presence of a loose bolt, this breakdown in correlation between the response amplitudes at the natural frequencies and the amplitudes at the sideband frequencies had to be quantified. According to the work by Pandey mentioned above, the best approach to accentuate changes in mode shapes due to damage is to compare the slopes of the mode shapes. With this in mind, an index was formulated using a normalized dot product, similar to the index presented in [58] and [51], between the slope, or derivative, of the magnitude of response at the natural frequency across the impact locations, henceforth referred to as  $M_{slope}$ , and the slope of the magnitude of the response at the left and right sideband frequencies across impact locations, henceforth referred to as  $SBL_{slope}$  and  $SBR_{slope}$ , respectively. A torque index ( $TI$ ) based on the

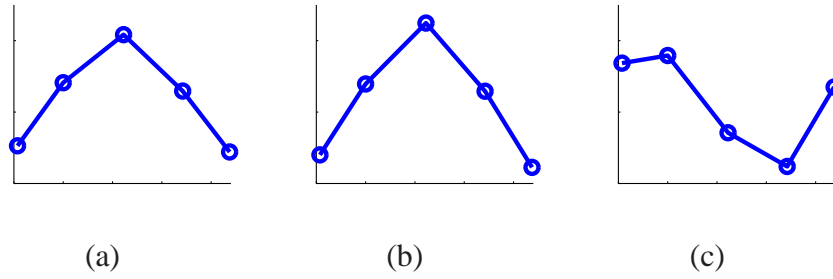


Figure 49: (a) Normalized amplitudes of response at the natural frequency versus impact location. (b) Normalized sideband amplitudes versus impact location for a structure with tight bolts. (c) Normalized sideband amplitudes versus impact location for a structure with a loose bolt.

normalized dot product between  $M_{slope}$  and  $SBL_{slope}$  was defined as:

$$TI_L = \frac{M_{slope} \bullet SBL_{slope}}{\|M_{slope}\| \|SBL_{slope}\|} \quad (30)$$

where  $\|\cdot\|$  is the length of the vector. Similarly,  $TI_R$  can be calculated by replacing  $SBL_{slope}$  with  $SBR_{slope}$  in the above expression. The normalized dot product is a measure of the orthogonality of the two vectors and can take on a value between 0 and 1. A value of 1 indicates that the vectors are very well correlated. A value of 0 indicates that the vectors have no correlation. The torque index that will be used for the remainder of this work is the average of  $TI_L$  and  $TI_R$ :

$$TI = \frac{TI_L + TI_R}{2}. \quad (31)$$

A  $TI$  value near 1 indicates that  $M_{slope}$  and  $SBL_{slope}$  and  $SBR_{slope}$  are nearly identical, indicating that all the bolts in the structure are tight. A lower value would indicate that one or more of the bolts is loose. In the following sections, the effectiveness of  $TI$  to indicate the presence of loose bolts will be studied using an analytical model, a three-beam, two-bolt structure, a four-beam, three-bolt structure, and a satellite panel.

**4.1.2 Finite Element Model Analysis.** A finite element model of a three-beam, two-bolt structure was used to validate initial experimental findings that in the case where loose bolts are present in a structure, the shape of the response amplitudes across different impact locations measured at a natural frequency is significantly different than the shape measured at the corresponding sideband frequencies. The model used for the analysis was the same as the one presented in Section 3.2.2 except that an additional beam and an additional bolt element was added. Figure 50 shows a schematic of the model including node locations, actuator location, and impact locations.

The simulation parameters were chosen to model the case when the bolt at node 5/6, bolt 1, is loose and the bolt at node 10/11, bolt 2, is tight. Therefore, only linear stiffness and damping were included for the model of bolt 2. The nonlinear spring coefficients were set to zero, and the linear parameters were kept at the values listed in Table 1. To simulate torque loss on bolt 1, both the linear and nonlinear parameters associated with bolt 1 were decreased using a scale factor of  $\frac{1}{1000}$

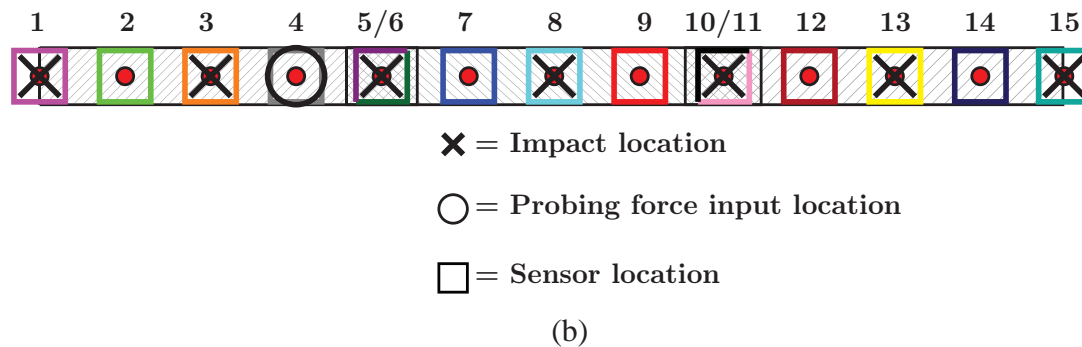
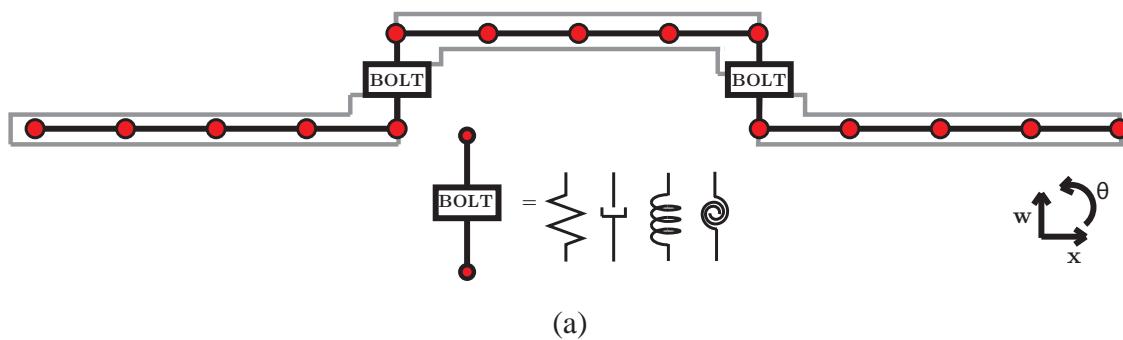


Figure 50: Three-beam, two-bolt setup.

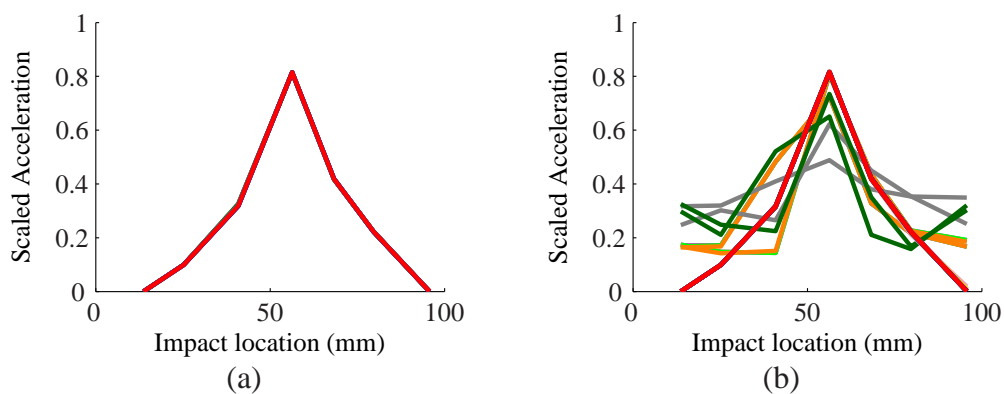


Figure 51: Scaled response amplitudes versus impact location from IM simulation results. (Line colors correspond to the sensor locations as indicated in Figure 50b.)

relative to the values listed in Table 1. The choice of these scale factors will be further discussed below.

Figure 51 shows the normalized amplitudes of response at the first natural frequency and at the first right and left sideband frequencies as a function of impact location for IM simulations performed using impact locations at nodes 1, 3, 5, 8, 11, 13, and 15. These locations were chosen to match the locations that will be used experimentally. The difference in the response shapes is clear. While this result correlates well with the initial results observed experimentally, a few distinctions must be made. First, the breakdown in response shape for the simulation data, observed in Figure 51b only occurs for sensor locations on the first beam. The effect of the nonlinearity does not propagate through the entire structure. This is contrary to the results observed experimentally, where sensors across the entire three-beam structure measured the change in response shape. Also, a large change in the linear spring coefficients associated with bolt 1 was required in order for this phenomenon to be observable. It is likely that for higher stiffnesses, the nonlinearity at the bolted joint was not being sufficiently exercised. This same phenomenon was observed experimentally, as will be presented below. Decreases in bolt torque as well as increases in the impact amplitude increase the observability of the breakdown in response shape at the sideband frequencies.

The discrepancies between the simulation results and the results observed experimentally are likely due to the model chosen for the bolted joints. In this work, nonlinear translational and rotational springs were used in combination with linear translational and rotational springs and dampers. The choice to omit any form of nonlinear damping was based on [59], which concludes that preloaded, flat metallic joints do not lose significant energy when subjected to normal forcing. However, it is likely that as the pre-load diminishes, there is coupling between tangential and normal modes. If this is the case, damping in the tangential direction would need to be considered. Because the emphasis of this work is on the experimental development of IM, this model development is left for future work.

#### **4.1.3 Three-Beam, Two-Bolt Assembly.**

**Experimental Setup and Test Procedure** The two-beam, one-bolt structure used in the previous chapters was expanded to a three-beam, two-bolt structure. Figure 52 shows the setup with seven sensors, one actuator, and fixed end conditions. Figure 53 shows the placement locations of the sensors and actuator along with the impact locations, bolt locations, and other test parameters. The actuator frequency (7,918 Hz) was chosen because a sine sweep performed on the structure showed that the response of the structure near 7,918 Hz was relatively constant. The sensors used were a combination of PCB365B11 (one channel only), PCB352C22, and PCB352C23. There were not enough of each type of sensor available to be able to use one model exclusively. Other equipment, the data acquisition system, and the analysis software were the same as described in Chapter 3.1. Finally, three bolt torque cases were studied. For Case 32-32, both bolts were tightened to 32 in-lbs. For Case 2-32, the first bolt was loosened to 2 in-lbs while the second bolt remained at 32 in-lbs. Two in-lbs was chosen as the torque for the loose bolt because it was the lowest torque for which self-loosening was not a problem for the tests, which involved multiple impacts. Case 32-2 is the inverse of Case 2-32.

The testing procedure was guided by the analysis method, which requires taking IM data using an array of impact locations. Three sets of IM tests were performed, one for each of the three torque cases. After the bolts were tightened to the prescribed levels as described in Figure 53, the



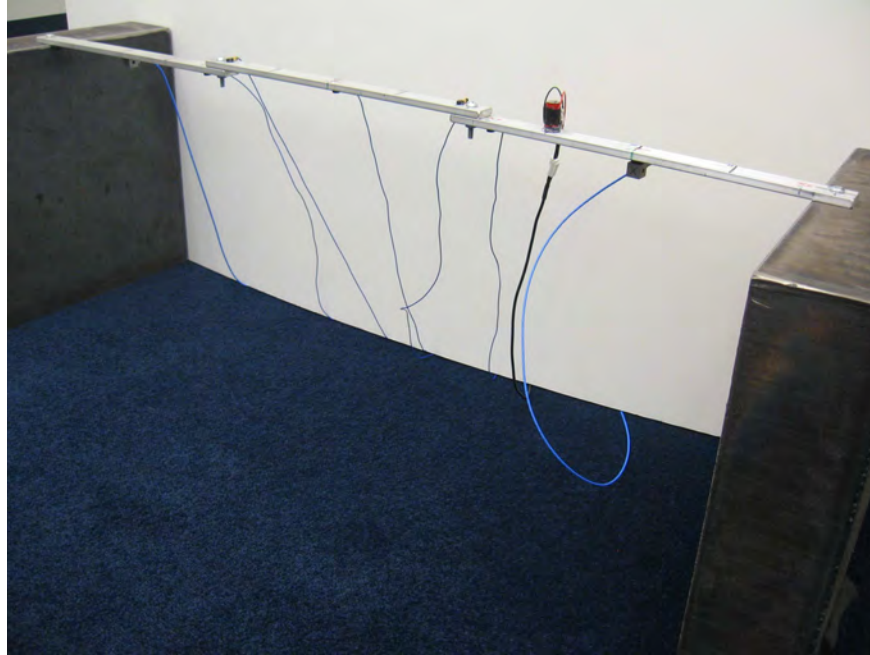


Figure 52: Three-beam, two-bolt setup.

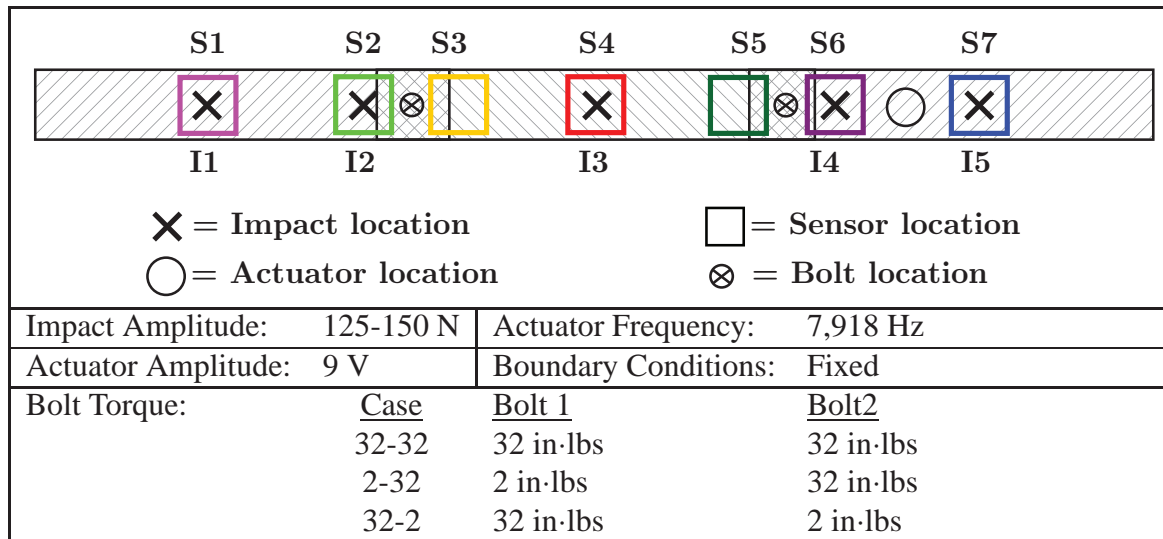


Figure 53: Setup and parameters for the three-beam, two-bolt IM testing. The color of each square indicates the color that will be used when plotting results from that sensor location.

following procedure was followed:

1. The beam was impacted at impact location I1 (as shown in Figure 53). Simultaneously, the actuator supplied an sinusoidal input force at 7,918 Hz with an amplitude of 9 V.
2. The acceleration response of the beam was measured by the seven sensors (S1-S7).

3. If the impact force was between 125-150 N, the frequency content of the impact showed acceptable roll-off characteristics, and the response at the actuator frequency fell within a pre-specified range, the data was accepted. Otherwise, it was discarded and the previous steps were repeated.
4. Once a successful impact was performed, the process was repeated for each of the other impact locations I2-I5.

The reason that the amplitude of response at the actuator frequency was monitored during testing was that there was occasionally significant variation in the response amplitude from impact to impact. At this point it is unclear if the source of the variation was the actuator itself or if the response at the actuator frequency was affected by the response to the impact. In order to minimize the effects of this variation, the amplitude of response was kept within a  $2 \text{ m/s}^2$  range.

## Results

Following the procedure outlined in Section 4.1.3, IM was performed on the three-beam, two-bolt structure. The first natural frequency was identified as 44 Hz. Figure 54 shows the high frequency portion of a typical response spectra from the IM testing. Sidebands are present at the actuator frequency (7,918 Hz) plus and minus the 44 Hz natural frequency (7,874 Hz and 7,962 Hz). Figure 55 shows the response amplitudes at the first natural frequency and at the first left and the right sidebands plotted as a function of impact location for all sensors. Qualitatively, the breakdown in the approximated mode shapes for Case 2-32 and Case 32-2 is obvious. To quantify the breakdown,  $TI$  was calculated for each sensor, as shown in Figure 56. There is a clear difference between Case 32-32 and the other cases. To synthesize this data, the average  $TI$  over all the sensors was calculated and is shown in Figure 57. The value of the average  $TI$  was 0.971 for Case 32-32, 0.494 for Case 2-32, and 0.697 for Case 32-2.

The green line in Figure 57 indicates a  $TI$  value of 0.937, which was set as the threshold value which defines a tight bolt. This value represents a 95% confidence threshold which was calculated from the results of repeating Case 32-32 ten times. The mean for these results was 0.97 with a standard deviation of 0.0166. The results of the tests with the tight bolts were very consistent, even after loosening and re-tightening the bolts. On the other hand, the results for Cases 2-32 and 32-2 showed more variation. For example, after repeating Case 2-32 ten times, the standard deviation was 0.0847. Although these results showed a higher degree of variation than that observed for Case 32-32, the value for  $TI$  was always distinct from the 0.937 threshold value.

It is not unexpected that the  $TI$  values for Case 2-32 and Case 32-2 are not identical. Although the bolt positions and torque values are symmetric for these two cases, factors such as the mass loading of the actuator can cause differences in the responses. High frequency modes such as those near the actuator frequency and in the modulation range are quite sensitive to these types of small changes. Therefore, it is likely that these factors are contributing to the difference in  $TI$  values for these two cases.

The results represented in Figure 57 are important because they indicate that IM testing can be used to identify the presence of a loose bolt in the three-beam, two-bolt structure without a historical reference data. Although the green threshold line was used for a basis for comparison above, its value is close to one, the absolute upper limit on the magnitude of  $TI$ . Therefore, because of this proximity to one for the case in which both bolts were tight and because the values of  $TI$



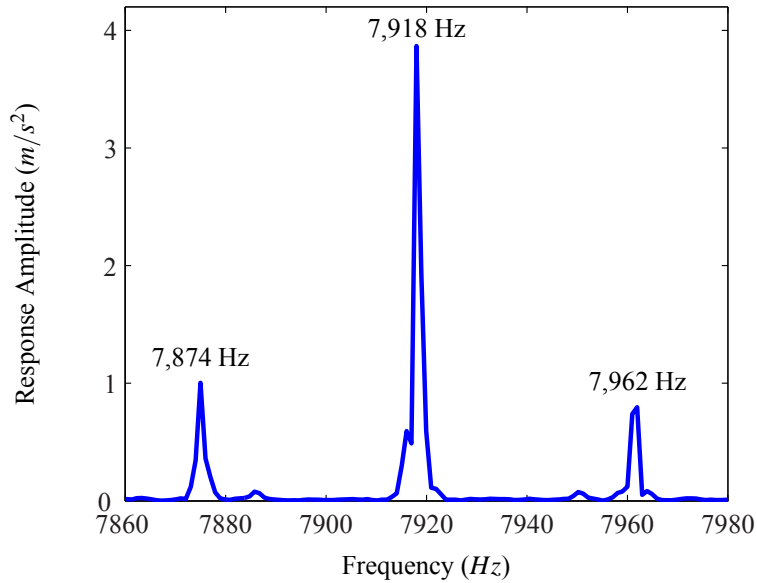


Figure 54: High frequency portion of the response spectra of the three-beam, two-bolt structure to an IM test from sensor S4 and impact location I3.

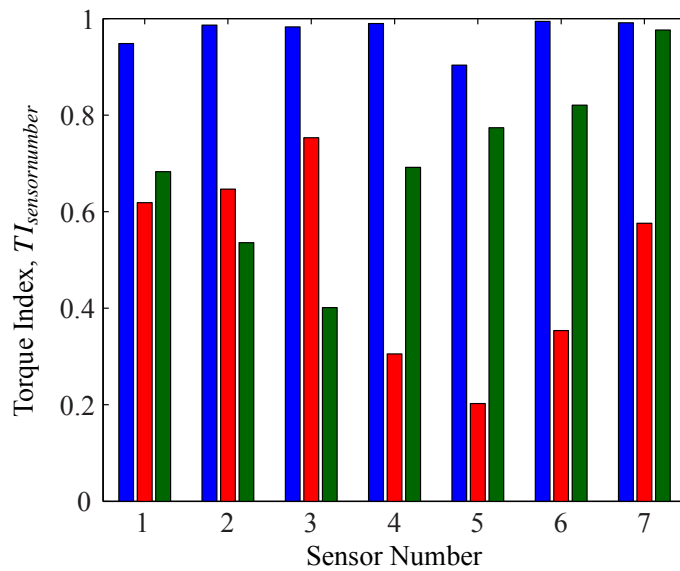


Figure 55: Torque index versus sensor number for each sensor for Case 32-32 (—), Case 2-32 (—), and Case 32-2 (—).

for the tests in which loose bolts were present were easily distinguishable from one, it can be concluded that a  $TI$  value significantly less than one indicates that a loose bolt is present within the structure.

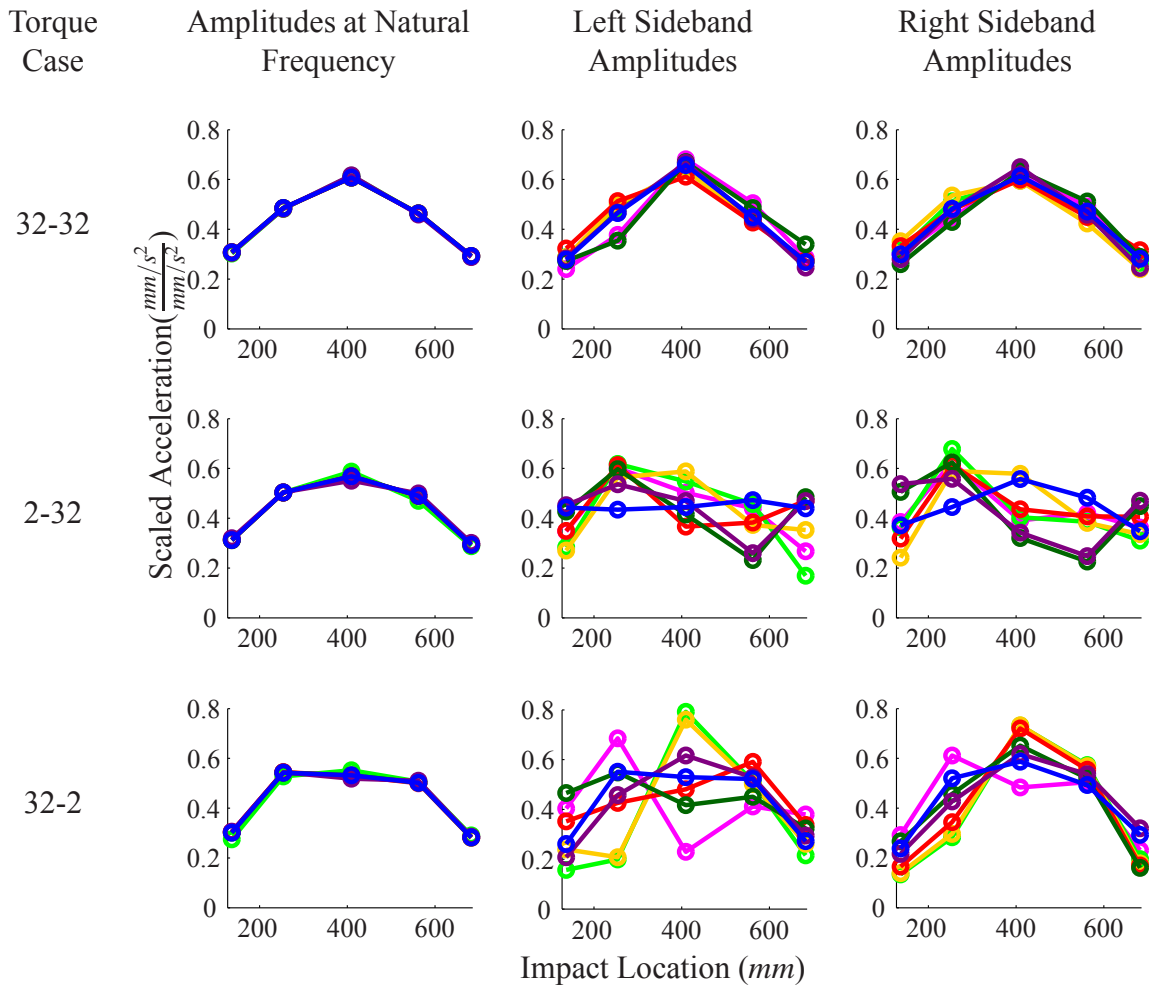


Figure 56: Scaled response amplitudes versus impact location for the three different bolt torque cases as measured from the seven different sensors. (Line colors correspond to the sensor locations as indicated in Figure 53.)

### Sensitivity

Up to this point, a loose bolt has been defined to be a bolt at 2 in·lbs. To study the sensitivity of IM results to the torque on the loose bolt, IM tests were performed for four more cases: Case 4-32, Case 32-4, Case 8-32, and Case 32-8, where the first number indicates the torque (in in·lbs) on the first bolt and the second number indicates the torque on the second bolt. All other test parameters discussed in the previous section were kept the same. As indicated by the results shown in Figure 58, the  $TI$  values clearly distinguish Case 4-32 ( $TI=0.71$ ) and Case 32-4 ( $TI=0.732$ ) from Case 32-32 ( $TI=0.971$ ). However, Figure 59, which shows results from Case 32-32, Case 8-32 ( $TI=0.972$ ), and Case 32-8 ( $TI=0.874$ ), indicates that bolts at 8 in·lbs were not as clearly detected. The most likely cause of this insensitivity to the loose bolts at 8 in·lbs is that the bolted interface, and therefore the nonlinearity, was not being sufficiently excited. To verify this hypothesis, Case 32-32, Case 8-32, and Case 32-8 were repeated using a higher impact amplitude range. The impact amplitude range was raised from 125-150 N to 200-225 N. Figure 60 shows that increasing the impact amplitude resulted in  $TI$  values (0.801 and 0.816) which identify the presence of the

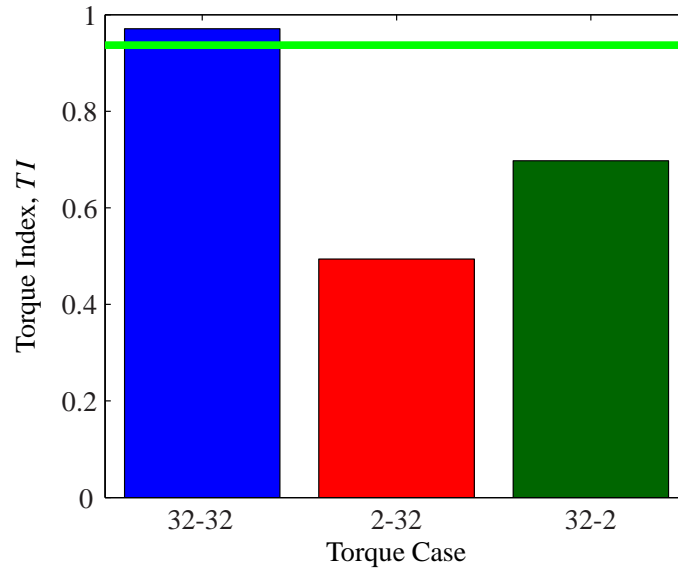


Figure 57: Torque index for Case 32-32 (—), Case 2-32 (—), and Case 32-2 (—). The green line indicates the damage threshold.

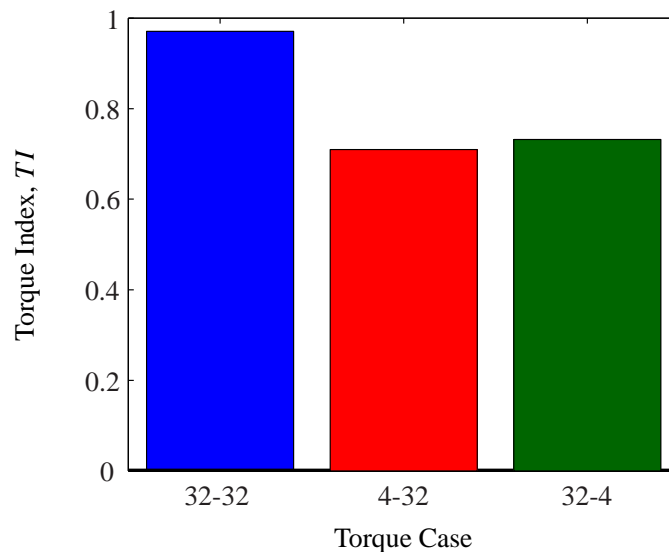


Figure 58: Average torque index for Case 32-32 (—), Case 4-32 (—), and Case 32-4 (—).

8 in·lb loose bolts. Although  $TI$  was not sensitive to the 8in·lb loose bolts at the lower impact amplitude range, increasing the range allowed for their detection. Therefore, in this case, increasing the impact amplitude leads to an increase in sensitivity of  $TI$ . This conclusion will be studied further in upcoming sections.

In order to determine the sensitivity of  $TI$  for higher torque levels, four additional IM tests were performed at the higher impact amplitude range (200-225 N). In addition to Case 32-32 and Case 8-32 presented above, results for Case 2-32, Case 4-32, Case 16-32, and Case 24-32 were

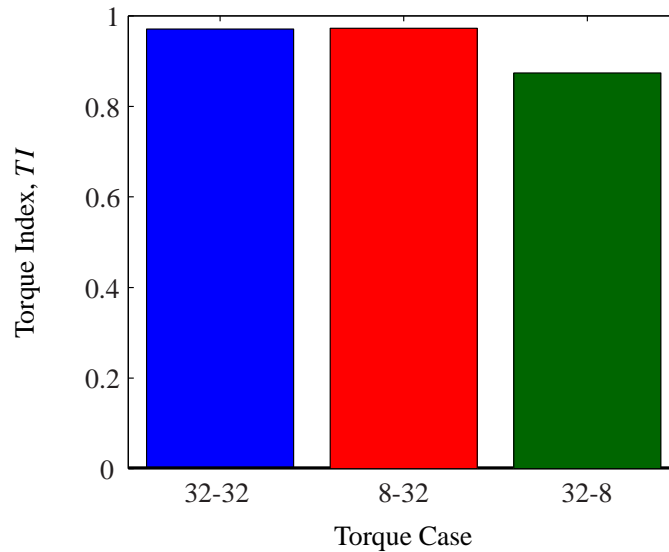


Figure 59: Average torque index for Case 32-32 (—), Case 8-32 (—), and Case 32-8 (—).

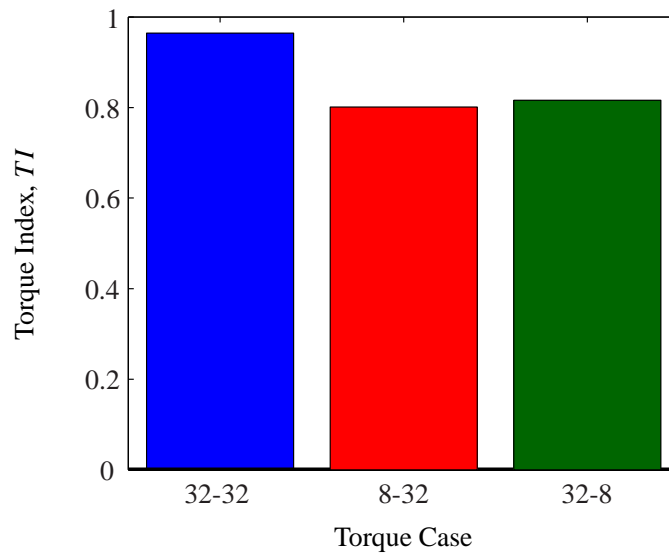


Figure 60: Average torque index for Case 32-32 (—), Case 8-32 (—), and Case 32-8 (—) with higher impact amplitude force.

collected. Figure 61 shows that at a lower torque level, the value of  $TI$  is also quite low and easily identifies the presence of the loose bolt. However, in general, as the torque on the loose bolt is increased, so too does the value of  $TI$ . It is important to note that this sensitivity curve is dependent on the magnitude of the impact force. As mentioned above, tests using the lower impact force range (125-150 N) were unable to identify the 8 in-lb loose bolts. In addition, this curve is unique to each bolt torque case. Recall that the  $TI$  values for Case 2-32 and Case 32-2 were different, even though they both were tightened to the same torque level. However, this curve does

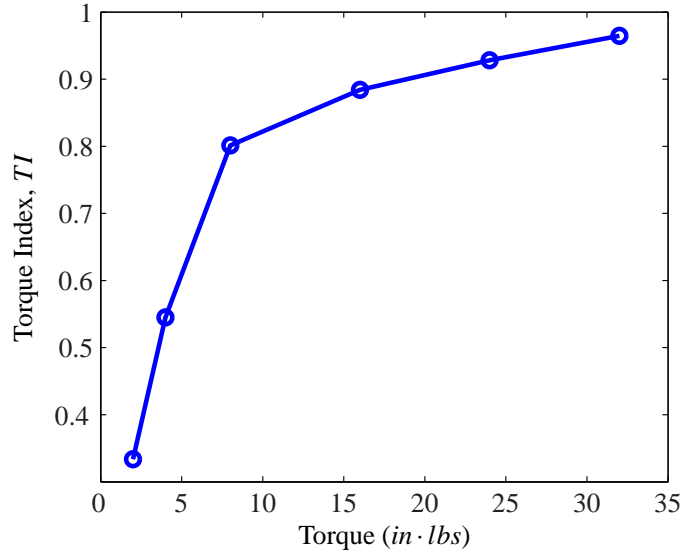


Figure 61: Torque index versus torque on bolt 1.

show that when all parameters except the torque on the bolt of interest are kept constant, the value of  $TI$  will decrease as the torque on the bolt decreases.

The results presented in this section show initial validation of using IM testing with the torque index ( $TI$ ) defined above for identifying the presence of a loose bolt within a structure without reference data. In the following sections, the validation process will continue by studying increasingly more complex structures.

#### 4.1.4 Four-Beam, Three-Bolt Assembly.

##### Experimental Setup and Test Procedure

The three-beam experimental setup described in the previous section was expanded to a four-beam, three-bolt structure in order to add complexity to the setup. Figure 62 shows the actual setup and Figure 63 identifies the sensor placements, impact locations, and actuator location used for IM testing. Initially, four bolt torque cases were studied: Case 32-32-32, Case 2-32-32, Case 32-2-32, and Case 32-32-2, where the numbers represent the torque on each of the three bolts. For each case, IM testing was repeated for each of the seven impact locations. Figure 64 shows the high frequency portion of a typical response spectra from the IM tests on the four-beam structure. For each test, the amplitude of response at the first natural frequency (25 Hz) and amplitudes of the corresponding right and left sidebands were recorded (8,925 Hz and 8,975 Hz). Results of the tests are presented in the next section.

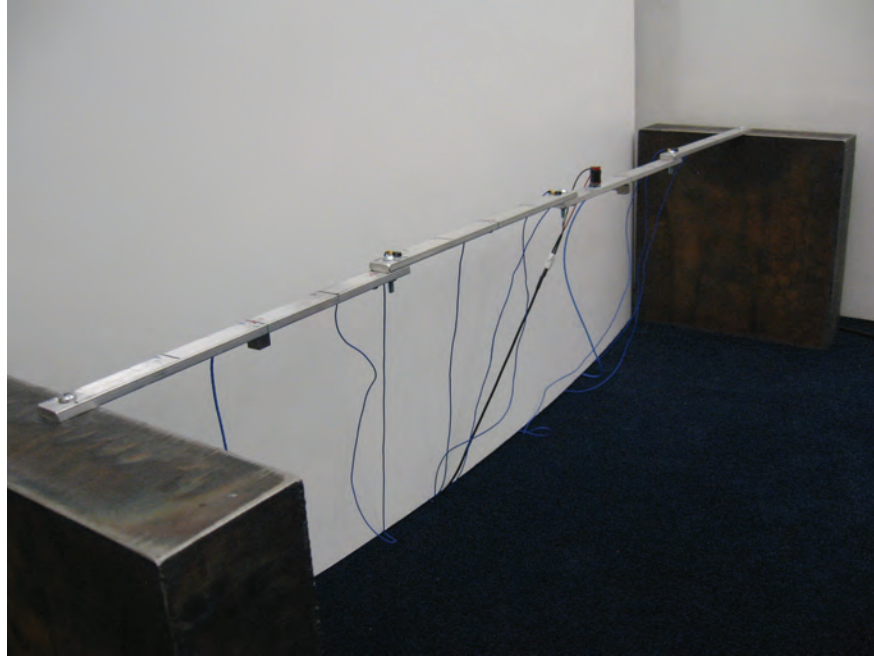


Figure 62: Four-beam, three-bolt setup.

Impact Amplitude:	125-150 N	Actuator Frequency:	8,950 Hz						
Actuator Amplitude:	9 V	Boundary Conditions:	Fixed						
Bolt Torque:	<u>Case</u>	<u>Bolt 1</u>	<u>Bolt 2</u>	<u>Bolt 3</u>					
	32-32-32	32 in·lbs	32 in·lbs	32 in·lbs					
	2-32-32	2 in·lbs	32 in·lbs	32 in·lbs					
	32-2-32	32 in·lbs	2 in·lbs	32 in·lbs					
	32-32-2	32 in·lbs	2 in·lbs	32 in·lbs					

Figure 63: Setup and parameters for the four-beam, three-bolt IM testing. The color of each square indicates the color that will be used when plotting results from that sensor location.

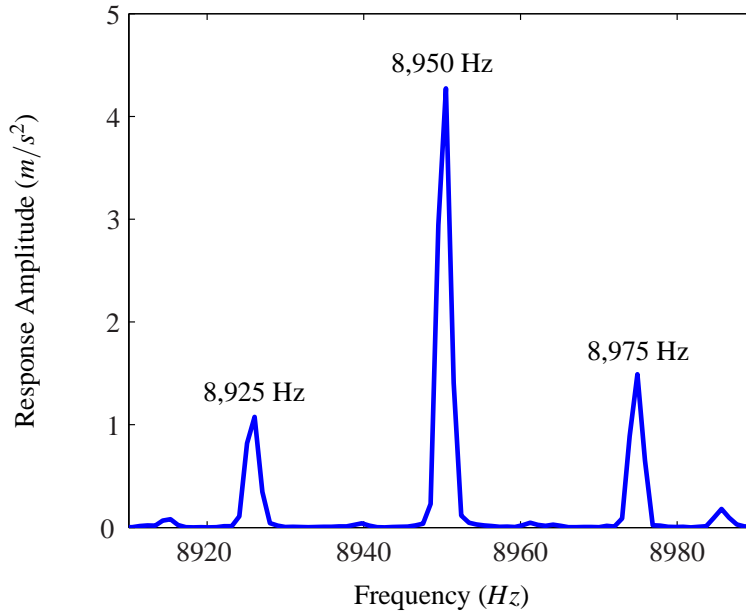


Figure 64: High frequency portion of the response spectra of the four-beam, three-bolt structure to an IM test from sensor S7 and impact location I5.

## Results

After performing IM testing for Cases 32-32-32, 2-32-32, 32-3-32, and 32-32-2, the amplitude of response at the first natural frequency (25 Hz) of the four-beam structure along with the corresponding right and left sideband amplitudes were plotted as a function of impact location. As shown in Figure 65, the same breakdown in the response shape at the sideband frequencies that was observed in the three-beam results is seen here. For Case 32-32-32, the response shape at the sideband frequencies appear to be nearly identical to the shape at the natural frequency. Clearly, the same correlation is not true for the other cases.

Once again, to quantify the degree of correlation between the shape of the response at the natural frequency and the shapes at the sideband frequencies, the torque index,  $TI$ , defined in the previous section was applied. Figure 66 shows that, as expected, the  $TI$  value for Case 32-32-32 is nearly equal to 1 (0.986). The value for  $TI$  in Case 2-32-32 (0.571), Case 32-2-32 (0.826), and Case 32-32-2 (0.499) are all much less than 1. The fact that Case 32-2-32 has a higher  $TI$  than the other two loose bolt cases is not surprising because as seen in Figure 65, the shapes at the sideband frequencies show more similarity to the shape at the natural frequency than in the other two loose bolt cases.

Next, six more bolt torque cases were studied: Case 4-32-32, Case 32-4-32, Case 32-32-4, Case 8-32-32, Case 32-8-32, and Case 32-32-8. Figure 67 shows the  $TI$  values for the cases in which the loose bolt is torqued to 4 in-lbs. Because these values show significant separation from one, they clearly indicate the presence of a loose bolt. Case 4-32-32 (0.728) and Case 32-32-4 (0.585) had higher  $TI$  values when compared to the corresponding value from the 2 in-lb tests. This trend was expected because, as shown in Section 4.1.3, an increase in torque generally leads to an increase in the value of  $TI$ . On the other hand, Case 32-4-32 (0.685) shows a decrease in

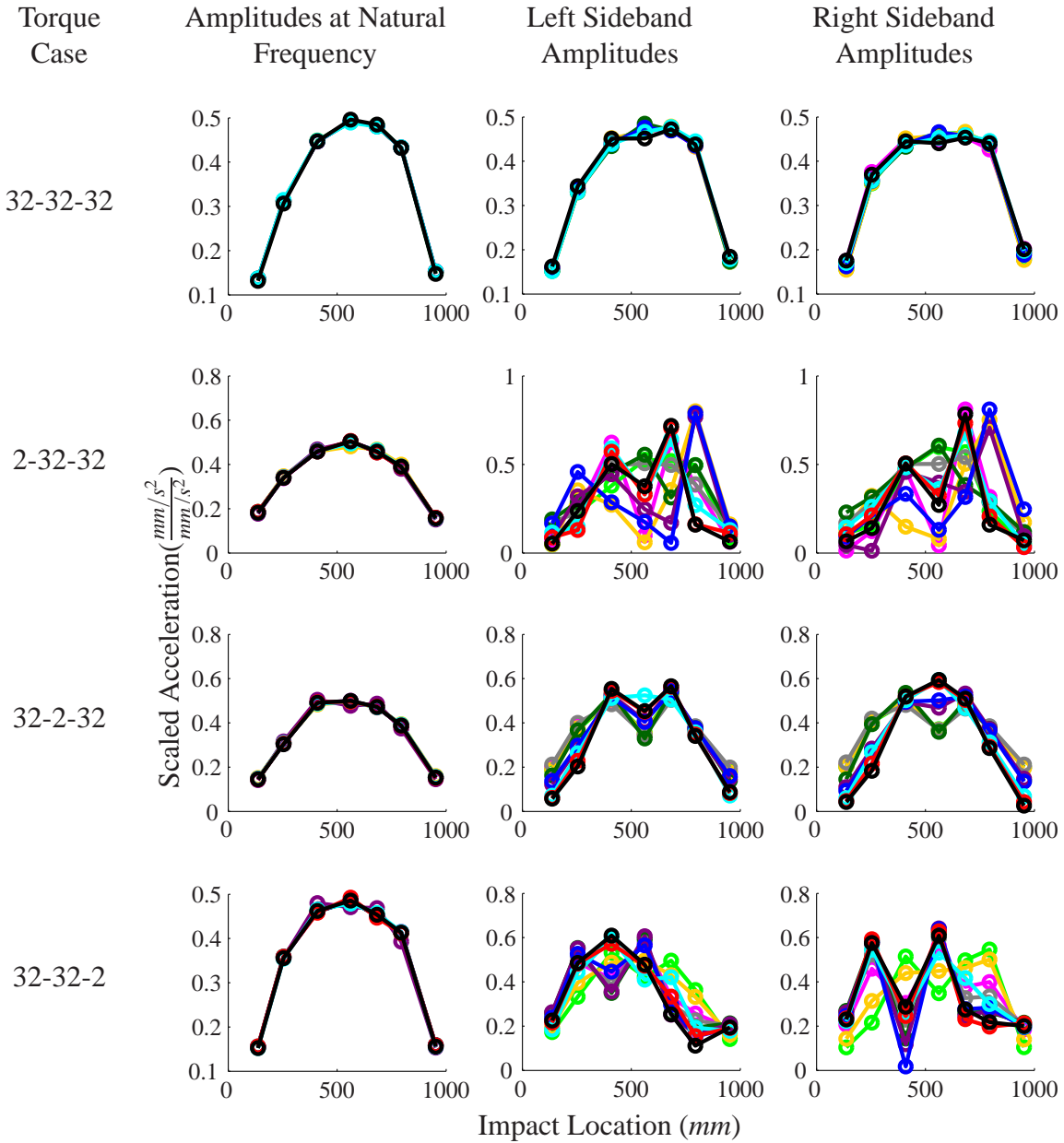


Figure 65: Scaled response amplitudes versus impact location for the four different bolt torque cases as measured from the ten different sensors. (Line colors correspond to the sensor locations as indicated in Figure 63.)

the  $TI$  value. It is unclear at this point what the cause of this unexpected decrease is, although the change in the underlying linear dynamics near the sideband frequencies due the change in torque on bolt 2 is a possible contributor to the decline.

Figure 68 shows the  $TI$  values for the cases in which the loose bolts are torqued to 8 in-lbs. As observed previously in the three-beam results, the  $TI$  values for these cases (0.962, 0.983, and 0.974) do not distinguish the cases in which loose bolts are present and the case when all the bolts are tight. Case 32-32-32, Case 8-32-32, Case 32-8-32, and Case 32-32-8 were repeated with the



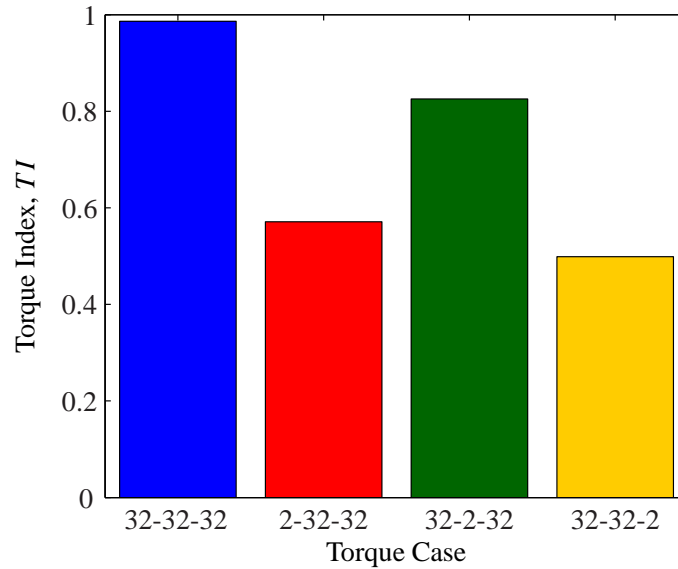


Figure 66: Torque index for Cases 32-32-32 (—), Case 2-32-32 (—), Case 32-2-32 (—), and Case 32-32-2 (—).

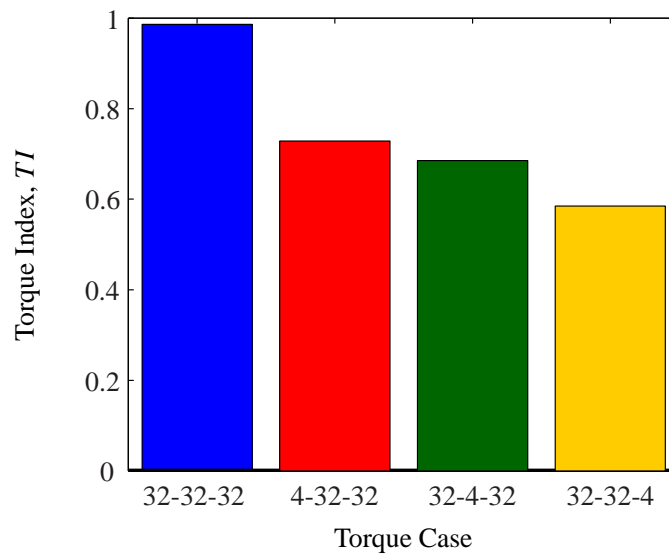


Figure 67: Torque index for Cases 32-32-32 (—), Case 4-32-32 (—), Case 32-4-32 (—), and Case 32-32-4 (—).

impact amplitude range increased to 200-225 N. Figure 69 shows the  $TI$  values for each of these four cases. As expected, increasing the impact amplitude resulted in a drop in the  $TI$  value for each of three cases: 0.87 for Case 8-32-32, 0.785 for Case 32-8-32, and 0.60 for Case 32-32-8. All of these values are well below the  $TI$  value for Case 32-32-32 at the higher impact amplitude (0.9863) and are significantly less than one, indicating that  $TI$  accurately identifies the presence of a loose bolt in the structure.

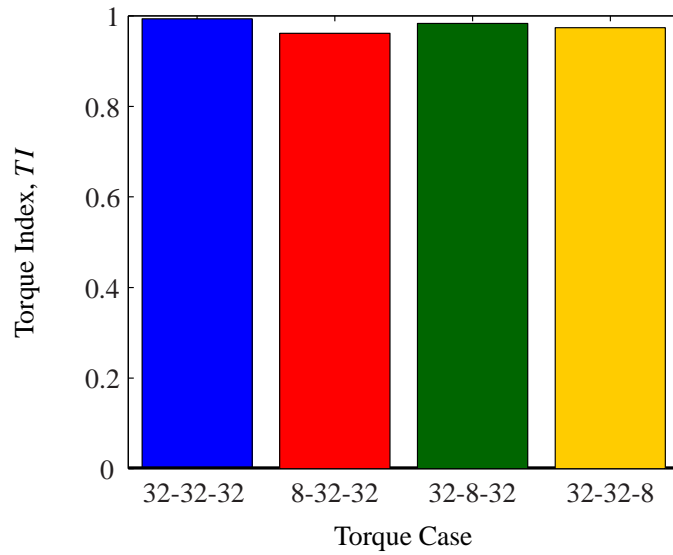


Figure 68: Torque index for Cases 32-32-32 (—), Case 8-32-32 (—), Case 32-8-32 (—), and Case 32-32-8 (—).

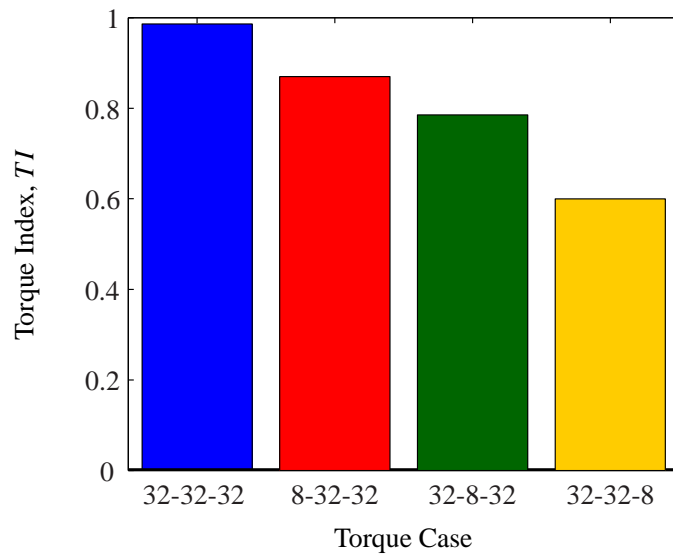


Figure 69: Torque index for Cases 32-32-32 (—), Case 8-32-32 (—), Case 32-8-32 (—), and Case 32-32-8 (—) with higher impact amplitude force.

The results for the four-beam, three-bolt structure presented in this section are consistent with those found for the three-beam, two-bolt structure. However, these test specimens are of relatively simple geometry. In the next section, IM will be applied to a satellite panel to test its effectiveness in identifying the presence of loose bolts in a more complex structure.

**4.1.5 Satellite Panel.** The intention of this work was to develop a method of identifying loose bolts in a satellite structure. Up to this point, only structures of simple geometry have been studied. In this section, IM is applied to realistic satellite panel. This panel is a prototype panel from a plug-and-play (PnP) satellite, which gets its name from its capability to accommodate a variety of different components depending on the mission of the satellite. The panel has a generic pattern of bolt holes which allows the desired set of components to be bolted on to the face of the satellite. This strategy of using bolted-on components to a generic satellite frame allows maximum flexibility in the capabilities of the satellite, but it also introduces the possibility of damage caused by improperly tightened bolts, especially during launch. In the following sections, the results from initial testing on a satellite panel will help determine the feasibility of using IM to detect the presence of loose bolts on a fully assembled satellite.

### Experimental Setup and Test Procedure

Testing was performed on a prototype PnP satellite panel provided by the Air Force Research Laboratory (AFRL) in Albuquerque, New Mexico. The aluminum panel, shown in Figure 70, is a  $31\frac{3}{4}$  inch square and has threaded bolt holes evenly spaced at 2 inch intervals in both directions. Additional bolt holes used for assembly are present at the midpoint of each edge and at each corner. The panel has ten small, removable access plates which are bolted onto the main structure, as shown in Figure 70. While the top side of the panel is smooth and plate-like, the underside is quite complex. Figure 71 shows that the underside has been designed with channels for cable management and with space for interior components.

The goal of the experiments that were performed on the satellite panel was to determine if IM could identify loose bolts in the connection of an external component without reference data. To simulate an external component, a  $4 \times 4 \times \frac{3}{8}$  inch aluminum plate with four through holes drilled to match the bolt hole pattern on the panel was machined. This plate was bolted on between impact points 19, 20, 27, and 28 and is shown in Figure 70. Four 8-32 bolts were used to secure the plate to the panel. Throughout the experiments presented here, the torques on all four bolts were kept at the same level. Five torque levels were used: 24 in-lbs, 4 in-lbs, 2 in-lbs, 1 in-lb, and hand tight. According to data provided by the AFRL, 24 in-lbs is considered proper bolt torque for external component connections.

The panel was equipped with ten PCB356A32 100 mV/g triaxial accelerometers and a PI P-010.10P piezo stack actuator whose locations are shown in Figure 72. An 8 x 8 grid of impact locations was marked with 4 inch spacing between points. The same PCB impact hammer and the same VXI data acquisition system used in previous experiments were again used here. In addition a power amplifier was added to the setup to increase the amplitude range of the actuator. Four bolts that were screwed into bolt holes at each corner on the underside of the panel provided support to the panel during testing, which created pin-like boundary conditions. Like in the previous sections, the testing procedure involved making impacts at each of the grid points while simultaneously exciting the panel with the actuator. A 7,500 Hz actuator frequency was used for all the tests presented in this section. One successful impact was made per point, where success was defined by having an impact amplitude and a response amplitude at the actuator frequency within a pre-specified range. Those ranges will be described further in the results section below. Acceleration time histories for each of the 64 impacts were collected from each of the ten sensors. The time data was windowed using a Tukey window with a ratio of tapered section to constant section of 0.5.

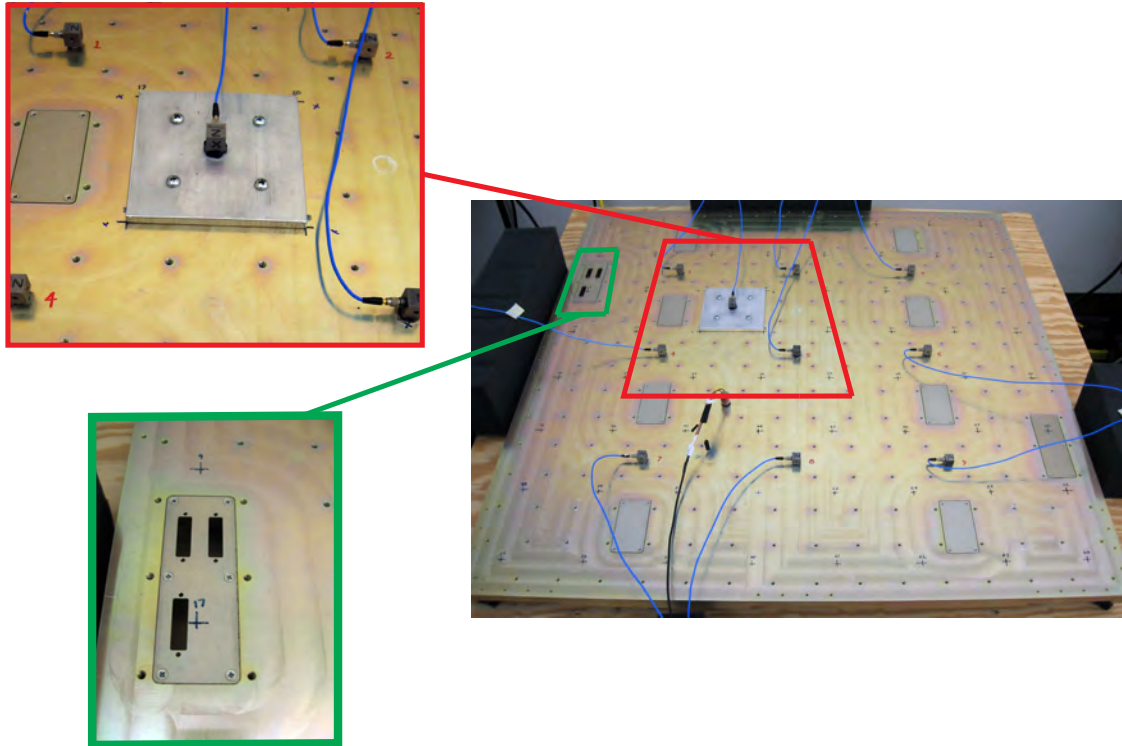


Figure 70: Satellite panel with close-up views of the simulated component and one of the ten access plates.



Figure 71: The underside of the satellite panel.

The windowed data was then transformed into the frequency domain for analysis via the Discrete Fourier Transform algorithm in MATLAB. This procedure was repeated for each of the five torque levels listed above.

The first step in the analysis was to pick out the mode or modes of vibration to analyze. Figure 73 shows the low frequency portion of the response spectra from seven of the impact points (11,

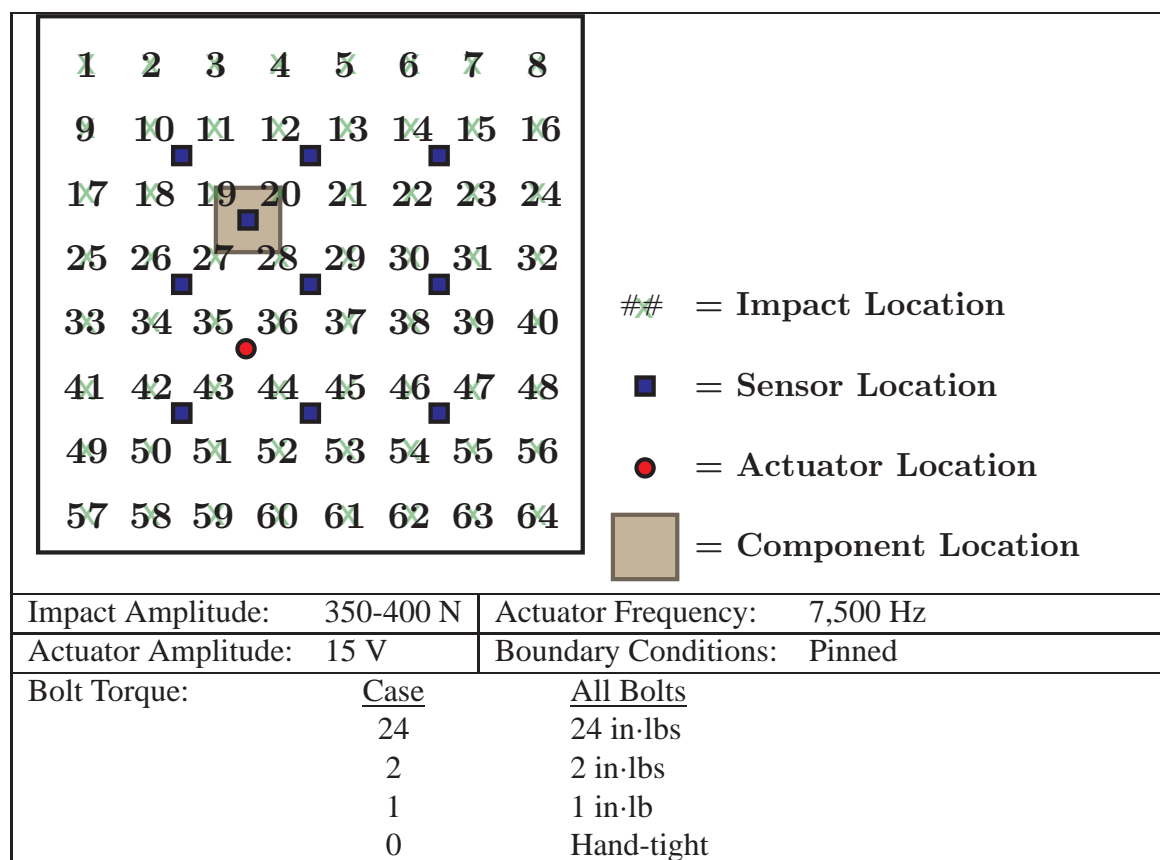


Figure 72: Setup and parameters for the satellite panel IM testing.

22, 41, 47, 51, 55, and 60) from an initial IM test of the satellite panel with all bolts at 24 in·lbs. This plot shows that the first 6 natural frequencies occur at 23 Hz, 41 Hz, 72 Hz, 164 Hz, 203 Hz, and 307 Hz. The strongest responses are at the 72 Hz, the 203 Hz, and the 307 Hz modes. In order to observe which modes were most strongly modulated, the portion of the response spectra surrounding the actuator frequency (7,500 Hz) was plotted, as shown in Figure 74. Nine sets of sidebands were identified. Table 3 details the frequencies at which the sidebands occur and identifies which actuator-natural frequency combination is most likely for each of those sideband frequencies. The first important characteristic of the response spectra to note is that not all modes are modulated as strongly as others. For example, the mode at 164 Hz is not modulated strongly enough to be detected. Also, modes are not modulated symmetrically about the actuator frequency. This is not a surprising results since previous work (Section 3.1.2 and Section 3.2.2) highlighted the effect of the underlying linear dynamics on the amplitude of the sidebands. Most notably, the 307 Hz mode is modulated much more strongly on the right (7,808 Hz) than on the left (7,193 Hz) of the actuator frequency. Finally, the combinations of frequencies for the response of the panel are much more complex than those observed in the response data from the three- and four-beam tests. The sidebands at 7,324 and 7,676 Hz are a combination of three different natural frequencies.

After analyzing Figures 73 and 74, it was determined that the modes of vibration to be analyzed for the satellite panel testing would be the 72 Hz mode, the 203 Hz mode, and the 307 Hz mode (right sideband only) because of the strong responses at both the low frequency and the cor-

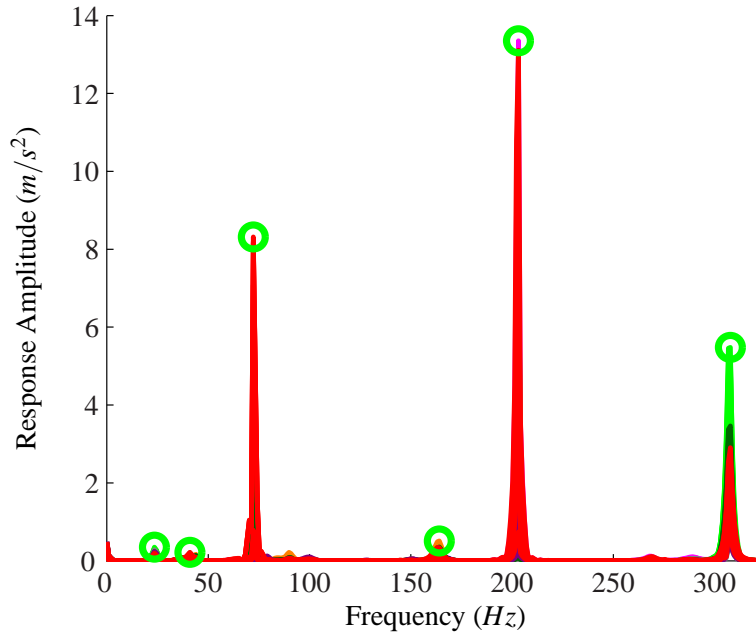


Figure 73: Low frequency portion of the response spectra from IM testing at several impact locations.

responding sideband frequencies. The response at the left sideband frequency for the 307 Hz mode was neglected because of its weak response.

As observed in the three- and four-beam tests, the effectiveness of IM to detect the loose bolts in the satellite panel was heavily dependent on the magnitude of the impact force. Therefore, IM testing was repeated at two different impact force levels. The results of these tests are presented in the next section.

## Results

### Impact Force Level 1

For the first set of IM tests, the impact force level was limited to 350-400 N. The response at the actuator frequency for sensor 7 was monitored to ensure that it was within a  $1.5 \text{ m/s}^2$  range. This monitoring was necessary because the force produced by the actuator occasionally varied significantly from its reference value. After performing an IM test at each of the 64 impact locations, the magnitude of response at each of the three natural frequencies of interest, 72 Hz, 203 Hz, and 307 Hz, was measured. Figure 75 shows the response amplitudes at the first three natural frequencies of interest as well as the response amplitudes at the corresponding sideband frequencies. Qualitatively, the shapes match very well.

In the previous sections, the correlation between the response at the natural frequencies and at the corresponding sideband frequencies was quantified using a scaled dot product on the derivatives of the response vectors. That quantification worked well because the response could be written as a one-dimensional vector. In the case of the satellite panel, the response is written as an  $8 \times 8$  matrix

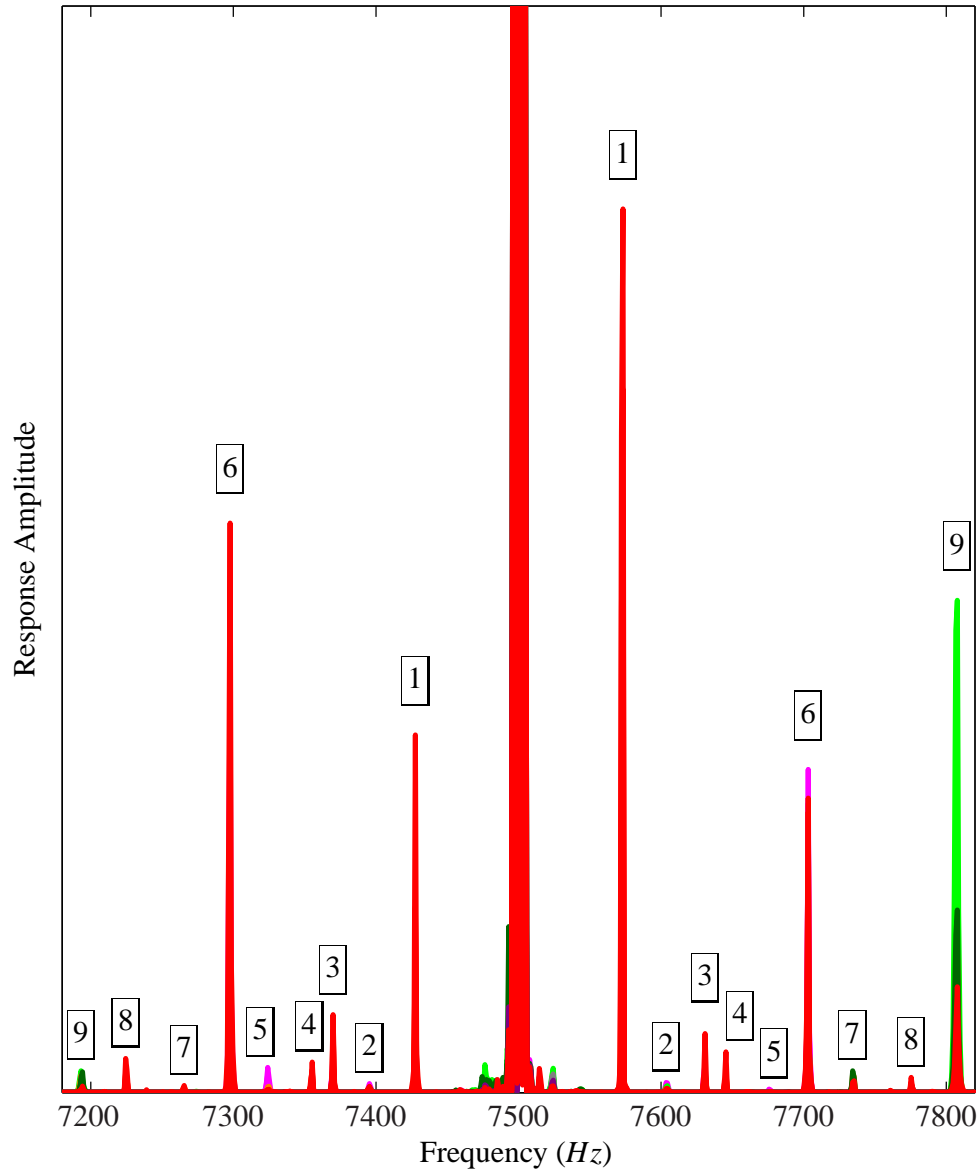


Figure 74: High frequency portion of the response spectra from IM testing at several impact locations.

and, therefore, the dot product as presented in the previous sections is not applicable. In order to quantify the correlation of the response at each natural frequency,  $M$ , with the response at the left sideband frequency,  $SBL$ , the sum of the dot products of the derivatives of each row and column of

Table 3: Sideband frequencies.

ID	Left Sideband Frequency (Hz)	Right Sideband Frequency (Hz)	Possible Combination
1	7,428	7,573	$7,500 \pm 72$
2	7,395	7,604	$7,500 \pm 2*41 \pm 23$
3	7,370	7,631	$7,500 \pm ???$
4	7,355	7,646	$7,500 \pm 72*2$
5	7,324	7,676	$7,500 \pm 2*41 \pm 23 \pm 72$
6	7,298	7,703	$7,500 \pm 203$
7	7,266	7,734	$7,500 \pm 164 \pm 72$
8	7,225	7,754	$7,500 \pm 203 \pm 72$
9	7,193	7,808	$7,500 \pm 307$

the response matrices are averaged as follows:

$$\begin{aligned}
 TI_L = & \left[ \sum_{ii=1}^{N_{row}} \frac{(M_{rowii})_{slope} \bullet (SBL_{rowii})_{slope}}{\|(M_{rowii})_{slope}\| \|(SBL_{rowii})_{slope}\|} \right. \\
 & \left. + \sum_{jj=1}^{N_{col}} \frac{(M_{coljj})_{slope} \bullet (SBL_{coljj})_{slope}}{\|(M_{coljj})_{slope}\| \|(SBL_{coljj})_{slope}\|} \right] / (N_{row} + N_{col}) \quad (32)
 \end{aligned}$$

where  $N_{row}$  and  $N_{col}$  are the number of rows and columns in the response matrices. Similarly,  $TI_R$  is calculated using  $SBR$ , the amplitude of response at the right sideband frequency, in place of  $SBL$ . The total torque index is then calculated by taking the average of  $TI_L$  and  $TI_R$ :

$$TI = \frac{TI_L + TI_R}{2}. \quad (33)$$

In the case that only one set of sidebands is being analyzed, this averaging step is skipped, and  $TI$  is equal to either  $TI_L$  or  $TI_R$  depending on whether the left or right set of sidebands was analyzed.

The  $TI$  was calculated for the 24 in-lb results (Case 24) discussed above. Figure 76 shows that, in agreement with the qualitative observations made about Figure 75, the  $TI$  values for each of the three modes (0.98, 0.96, and 0.89 respectively) are close to one, which indicates that the correlation between the response at the natural frequency and the response at the sideband frequencies is very



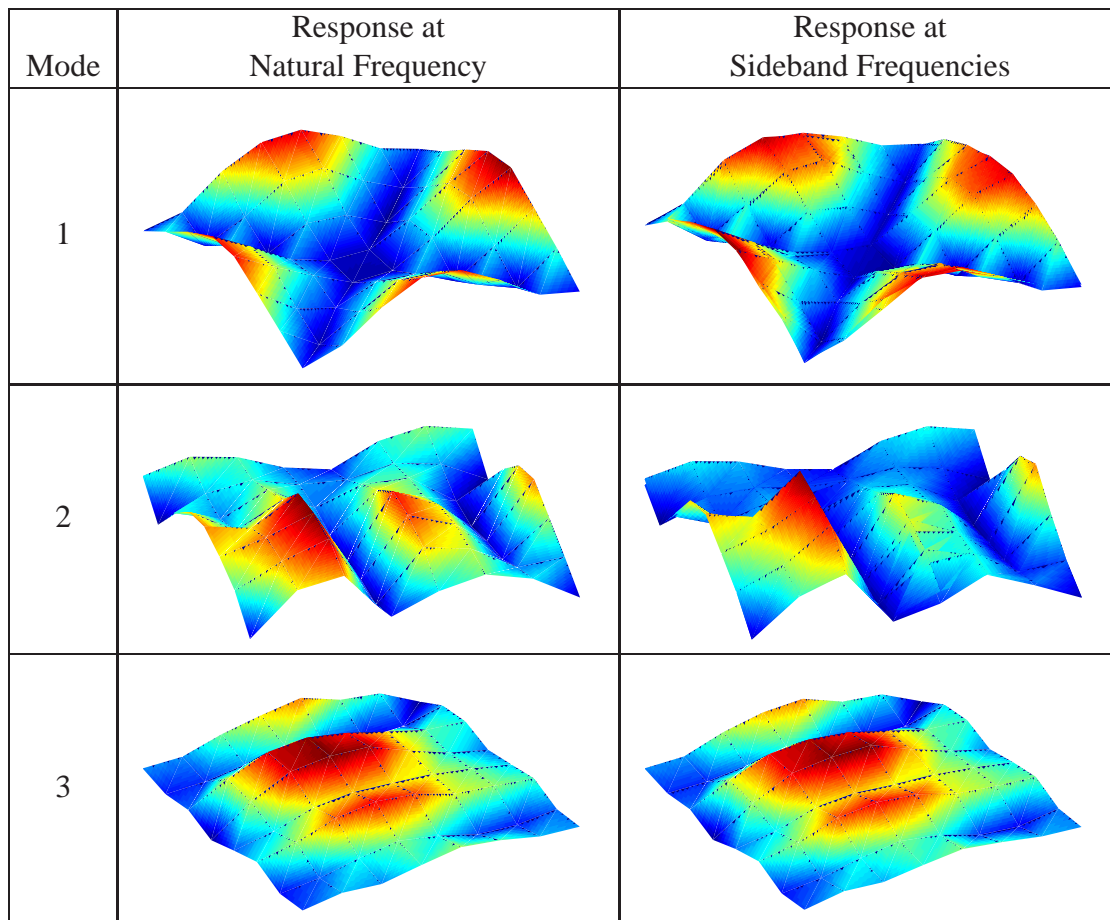


Figure 75: Scaled response amplitudes versus impact location for IM tests for Case 24.

strong. Mode 3 shows the least amount of correlation for this case, which may indicate that this mode should not be considered.

Next, IM tests were repeated with the bolts on the small plate torqued to 2 in·lbs (Case 2), 1 in·lb (Case 1), and then hand tight (Case 0). Figure 77 shows the  $TI$  values for these cases as well as the values for Case 24. Although the expected trend of lower  $TI$  values for lower torque values is evident, the discrepancy between loose and tight is not obvious enough to use for reference-free detection except for Case 0. When the bolts are hand-tightened, the  $TI$  values clearly indicate that loose bolts are present: 0.779 for mode 1, 0.809 for mode 2, and 0.611 for mode 3. In an effort to improve the sensitivity of  $TI$ , tests were performed with an increased impact force amplitude.

## Impact Force Level 2

IM tests for Case 24, Case 2, and Case 1 were repeated with the impact amplitude range raised to 600-675 N in an effort to increase the discrepancy between the  $TI$  values for the loose bolt cases and the tight bolt case. Figure 78 shows that for mode 1, the increase in impact force amplitude did lead to  $TI$  values for Case 1 (0.826) and Case 2 (0.764) which are more distinct from Case 24 (0.924). For mode 2, the separation between Case 1 and Case 2 did increase, but the actual  $TI$

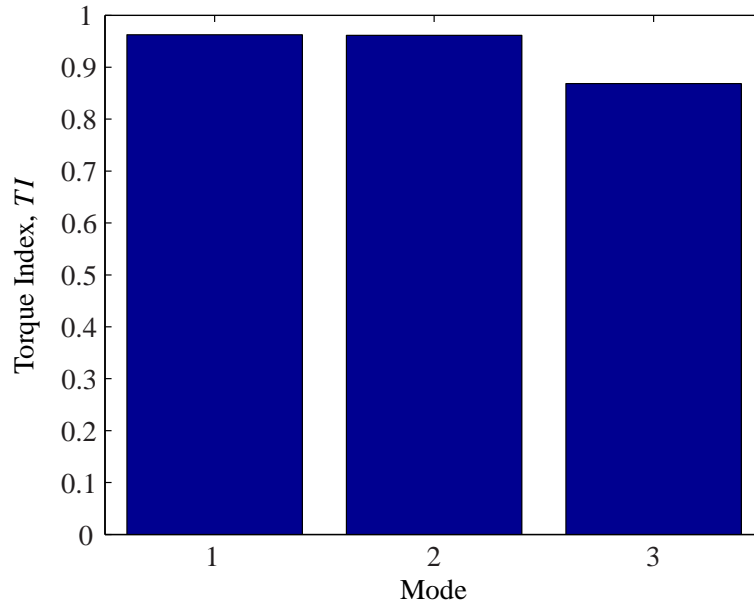


Figure 76: Torque index for Case 24 for the first three modes.

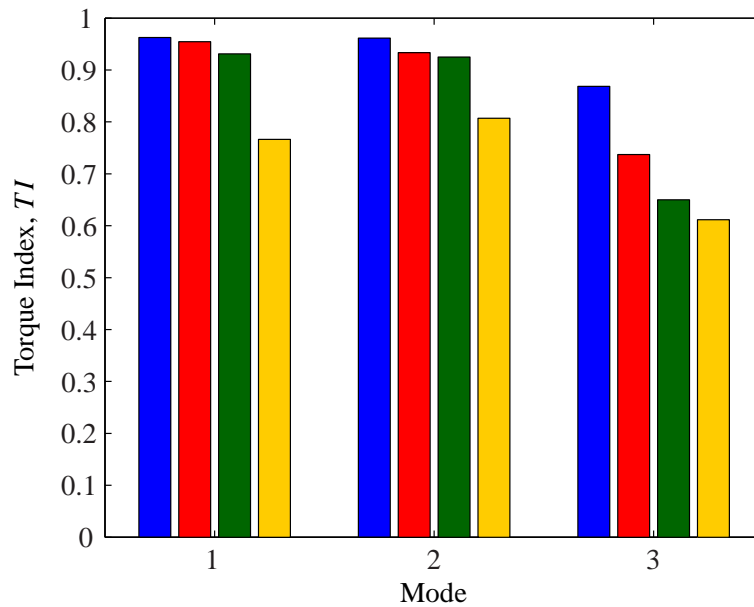


Figure 77: Torque index for Case 24 (—), Case 2 (—), Case 1 (—), and Case 0 (—) for the first three modes.

values (0.878 and 0.915) are not dissimilar enough from one to be good indicators that the bolts are loose. Although the  $TI$  values for mode 3 show the anticipated trend of having a lower value as the torque is lowered, the value for Case 24 (0.695) is too low to be considered healthy. From these results, it appears that modes 2 and 3 are not as effective as mode 1 for the dot product analysis.

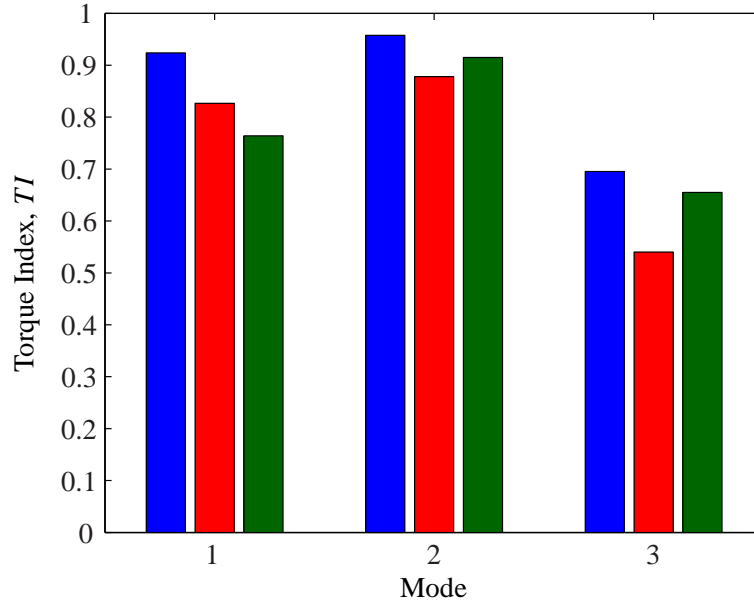


Figure 78: Torque index for Case 24 (—), Case 2 (—), and Case 1 (—) for the first three modes with higher impact amplitude force.

With the increase in input force amplitude, the  $TI$  values associated with mode 1 were able to clearly indicate the presence of the loose bolts in the component-to-satellite panel interface.

**4.1.6 Conclusions.** The results presented in this chapter are important because they establish a unique method for identifying the presence of loose bolts within a structure. The torque index,  $TI$ , was defined to quantify the difference between the shape of the response amplitudes across impact locations at a natural frequency and the shapes at the corresponding sideband frequencies. An important characteristic of  $TI$  is that its value is limited to the range between zero and one, eliminating the need for a historical reference data. The effectiveness of using  $TI$  to identify the presence of loose bolts was demonstrated on a three-beam, two-bolt structure; on a four-beam, three-bolt structure; and on a PnP satellite panel. The  $TI$  values for the tests on the beam structures more clearly identified the loose bolt cases as compared to the values for the satellite panel tests. There are several factors that likely contribute to this decrease in sensitivity for the satellite panel tests. First, the bolts in the beam structures were more fundamentally a part of the stability of the structure. If a bolt were removed, the structure would no longer take the same form. In the case of the satellite panel, removing a bolt changes little about the overall structure. From that perspective, the fact that the  $TI$  was less sensitive on the satellite panel is not surprising. However, it should be noted that the trend of decreasing values of  $TI$  for decreases in torque level was observed. The second factor that may have contributed to the  $TI$  values being less sensitive to the loss of bolt torque in the satellite panel tests is the fact that the components being bolted together were fastened by a through-hole to threaded-hole connection. The beam structures utilized a bolt and nut combination. It is possible that the threaded hole connection maintains a more secure connection at low torque levels than the bolt-nut configuration. This claim is supported by the fact that a large drop in  $TI$  value was observed in the satellite panel tests when the bolts were torqued hand-tight.

In demonstrating the effectiveness of  $TI$  to identify the presence of loose bolts, it was found that the level of impact force used for the IM testing is a key parameter.  $TI$  is not effective if the bolted interface is not sufficiently excited. For this work the amplitude of the impact force that was considered sufficient was determined by trial and error. Further work is needed to establish rule-of-thumb guidelines on determining impact force level depending on the desired sensitivity of  $TI$ . In addition, future work could also look to establish a link between the  $TI$  value and the degree of torque loss within the structure. This will be a difficult task because, as demonstrated throughout the results presented in this work, the complete set of parameters which contribute to the amplitudes of the sidebands has not yet been established. It is known that the torque on the bolts in a structure directly affect the sideband amplitudes, but the effect of factors such as the underlying linear dynamics in the modulation range are, at this point, less predictable.

The testing procedure to determine  $TI$  requires that IM be repeated at an array of impact points. In this work, that array was chosen to be a moderately spaced mesh. Obviously, the number of points in the array directly affects the time required to complete the tests. A requirement of the method desired for loose bolt detection on the satellite structures is that testing time be minimized. With that requirement in mind, future work should look to minimize the number of impact locations necessary to obtain quality results. In addition, a fully instrumented satellite may have fewer impact locations available in a less regular layout. Optimizing impact location placement and frequency is left to future work.

Overall, the work in this chapter lays the groundwork for the development of the use of IM and the torque index,  $TI$ , as a method for identifying the presence of loose bolts within a structure with use of historical reference data. Its application was demonstrated on three, increasingly complex structures with effectiveness.

## 4.2 Loose Bolt Detection Using Impact Modulation With Baseline Data

In the previous chapter, a method for detecting the presence of loose bolts within a structure using Impact Modulation (IM) was presented. The development of that method was motivated by the need to test structures for which no historical reference is available. There are, however, many applications for which IM data from a healthy structure could be acquired and, consequently, IM could be used to monitor the health of the bolted joints within a structure over time. For example, after initial assembly, the rapidly assembled satellites being developed by the Air Force Research Lab (AFRL) experience multiple events, such as validation testing and transport to the launch site, which have the potential to change the status of the satellite's bolted joints. If a baseline IM test were performed after initial assembly, follow-up tests could be performed after each event to evaluate the likelihood that bolts had become loose. In addition, the development of an analysis method using historical data could broaden the application of IM to structures for which making an array of impacts across the entire structure is not feasible. Finally, the use of baseline data could potentially decrease the testing time compared to the history-free method.

The foundation for a baseline-dependent method for identifying the loss of torque on a bolt has been established throughout this work. In Section 3.1.2, results from experimental IM tests with the two-beam, one-bolt setup showed that as the torque on the bolt decreased, the sideband amplitudes increase. In Section 3.2.2, the increase in sideband amplitudes that resulted from simulated IM testing was tied to the increases in nonlinearity at the bolted joint due to the loss of torque on the bolt. In addition to these findings, Amerini and Meo [16] used Vibro-Acoustic Modulation (VM) to show that the difference between the amplitude of response of a bolted structure at the actuator frequency and the sideband amplitudes decreases as bolt torque decreases, implying that the sidebands grow as bolt torque decreases. Using these conclusions as a basis, the goal of the work presented in this chapter is to develop an analysis method that can be used to track the status of the torque on a bolt assuming that measurements from the healthy case are available and to demonstrate the effectiveness of the method on a variety of bolted structures. The following sections outline the details of the method and present the results from its application to the three-beam, two-bolt structure; the four-beam, three-bolt structure; the satellite panel; and a fully instrumented PnP satellite.

**4.2.1 Experimental Procedure and Analysis Method.** It is proposed that the loss of torque on a bolt within a structure can be identified by interrogating the structure using IM testing and then comparing the results of that testing to baseline results acquired from the structure when the bolts were known to be at a proper torque level. However, as concluded in Chapter 3.1, caution must be exercised when comparing results of different IM tests because the linear properties of the structure affect the results. For example, it was found that impact amplitude and location; sensor location; and actuator amplitude and frequency all affect the amplitude of the sidebands that manifest during IM testing. Therefore, it is important that certain test parameters remain constant for all IM testing performed on a given structure. Ideally, the only parameter that should affect the IM results is a change in bolt torque. Variations due to other factors detract from the accuracy of the diagnosis of the torque on the bolt.

Results will be presented below for IM testing of four structures in which the torque on one or more of the bolts within each structure was varied. The experimental procedure used for these tests called for the impact, actuator, and sensor locations to remain constant for all tests performed on the

chosen structure. In addition, the range of acceptable impact amplitudes, the range of acceptable response amplitudes at the actuator frequency, and the actuator frequency were held constant. The response at the actuator frequency was maintained across different tests by adjusting the amplitude of the actuator force. One set of tests was performed for each of the four structures in which the following experimental procedure was executed at various bolt torque levels:

1. Choose impact, actuator, and sensor locations. These locations remain constant for each set of tests.
2. Choose an impact force range and a range for the amplitude of response at the actuator frequency. These ranges remain constant for each set of tests.
3. Choose an actuator frequency. This frequency remains constant for each set of tests.
4. Perform IM testing by simultaneously impacting the structure and exciting the structure with the actuator. Collect the time acceleration time history from the sensor. Repeat three times.

The procedure for the analysis of the data collected from these tests involved calculating the left and right modulation indices using the integration technique, explained in detail in Section 3.1.2, in which the area under the modulated spectrum of response was calculated and then normalized by the area under the modal spectrum. Recall that the modal spectrum refers to the low frequency portion of the response, which contains the dynamics that are a result of the excitation from the impact. The left modulated spectrum refers to the high frequency portion of the spectrum which occurs at frequencies equal to the actuator frequency minus the modal spectrum frequencies. Similarly, the right modulated spectrum occurs at frequencies equal to the actuator frequency plus the modal spectrum frequencies. The detailed analysis procedure used was as follows:

1. Apply a Tukey window with a ratio of tapered section to constant section of 0.5 to the first acceleration time history.
2. Convert time data to the frequency spectrum using the Discrete Fourier Transform algorithm in MATLAB.
3. Calculate the left ( $I_L$ ) and right ( $I_R$ ) modulation indices.
4. Compute the average of the modulation indices:

$$I_{ave1} = \frac{I_L + I_R}{2}. \quad (34)$$

5. Repeat steps 1-3 for the second and third time histories.
6. Find the average modulation index for three repetitions:

$$I = \frac{I_{ave1} + I_{ave2} + I_{ave3}}{3}. \quad (35)$$

For the results presented in the following section, the average modulation index for the three repetitions performed,  $I$ , will be the feature used to diagnose the status of the bolts within the structure. A baseline value of  $I$  will be determined by testing the structure when all the bolts within that structure are properly torqued. Values of  $I$  calculated for tests performed when one or more of the bolts have been loosened will be compared to the baseline value to determine whether the IM testing successfully identified the loose bolt.

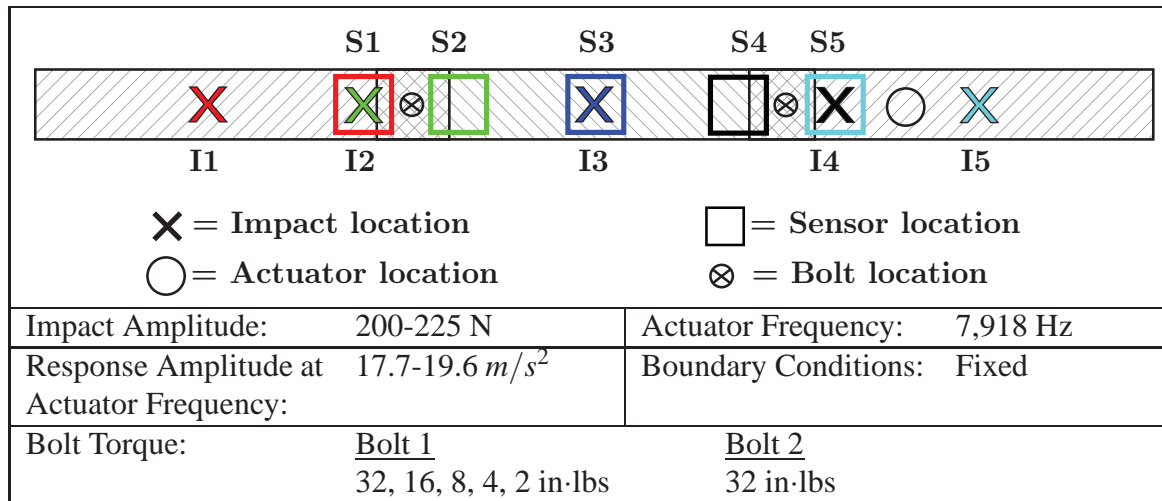


Figure 79: Setup and parameters for the three-beam, two-bolt IM testing. The color of each square and of each X indicates the color that will be used when plotting results from that sensor or impact location.

#### 4.2.2 Results.

**Three-Beam, Two-Bolt Results** The first set of tests was performed on the three-beam, two-bolt structure described in Section 4.1.3. The torque on bolt 2 was kept at 32 in·lbs throughout all tests. IM testing was repeated with the torque on bolt 1 equal to 32, 16, 8, 4, and 2 in·lbs according to the procedure outlined in the previous section. Figure 79 shows the other tests parameters used. Note that five sensor locations and five impact locations are indicated in the figure even though the experimental procedure calls for the use of one impact location and one sensor. The reason for this discrepancy is that the IM tests for the three-beam, two-bolt structure were repeated using several different sensor-impact location combinations to determine the optimum test setup.

To study the effect of sensor location, five sets of data were generated by repeating IM using impact location I1 and each of the five sensors S1-S5. Each set of data included IM tests for each of the five torque levels. The modulation index  $I$  was calculated for each of tests and then normalized by the value of  $I$  from the test where all bolts were properly torqued to 32 in·lbs. Figure 80a shows these normalized values of  $I$  plotted as a function of the torque on bolt 1 for tests using each of the five sensors. As expected, the value of  $I$  tends to increase as the torque on bolt 1 decreases. The results for the different sensors are very similar, indicating that for the three-beam setup, sensor location is not a significant factor in the effectiveness of the analysis method.

Next, the effect of impact location was studied. Five sets of data were generated by repeating IM using sensor S1 and each of the five impact locations I1-I5. Again, each set of data included IM tests for each of the five torque levels. Figure 80b shows the values of  $I$ , normalized by the value for the 32 in·lb test, for each test as a function of the torque on bolt 1. The results again show the expected growth trend in  $I$  with decreasing torque, and are very similar for all impact locations. Interestingly, the  $I$  values for impact location I3 are generally the greatest, followed by the values for I2 and I4, followed by the values for I1 and I5. This ordering reflects the first mode



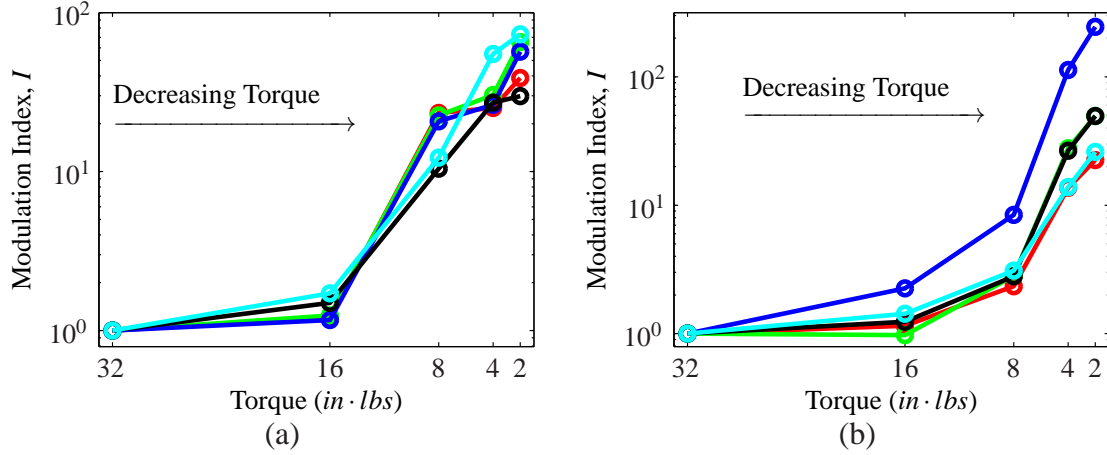


Figure 80: Modulation index,  $I$  versus torque on bolt 1 for IM testing for (a) different sensor locations and (b) different impact locations. Line colors correspond to the sensor and impact locations indicated in Figure 79.

shape of the beam, indicating that even with the normalization of the modulated spectrum by the modal spectrum, the linear properties of the structure can still be observed in the results.

To study the sensitivity of  $I$  to the torque on bolt 1, ten IM tests were repeated for each of the five torque levels using impact location I1 and sensor S1. After each test, bolt 1 was loosened and re-tightened. The results of these tests are presented as a box-and-whiskers plot in Figure 81. The blue box encloses the range of  $I$  values within the 25th to 75th percentiles, with the median indicated by the red line. Whiskers extend to the most extreme data points that are not considered outliers. Red crosses mark outliers. The ranges of  $I$  values for the 32, 16, and 8 in·lb tests show no overlap. The values for the 4 and 2 in·lb cases overlap each other, but are distinct from the higher torque cases. It is likely that one contributing factor to this overlap is that the torque screw driver accuracy was not guaranteed at such low torque levels.

Table 4 shows the percent change in the mean  $I$  values for each case relative to the 24 in·lb, or baseline, case. When bolt 1 was loosened to 16 in·lbs, the  $I$  value increased by about 47% of the baseline. For the 8 in·lb case,  $I$  was over five times higher than the baseline. The value of  $I$  for the lowest torque levels changed by an order of magnitude. These results demonstrate the effectiveness of using the  $I$  values calculated from IM testing to identify the presence of loose bolts within the three-beam, two-bolt structure.

In the work presented by Amerini and Meo [16], a trend similar to that seen in the above figures was observed for a two-plate, one-bolt structure. In that work, a hyperbolic tangent curve was fit to VM data that quantified the difference in response amplitude at the actuator frequency and the sideband amplitudes. This curve-fitting procedure was applied to the IM results for the three-bar structure. Figure 82 shows the mean  $I$  values from the IM tests at the five torque levels as a function of percent torque loss relative to 32 in·lbs. A curve of the following form was fit to that data:

$$I_{trend} = A + \tanh[B(t - C)] + D \quad (36)$$



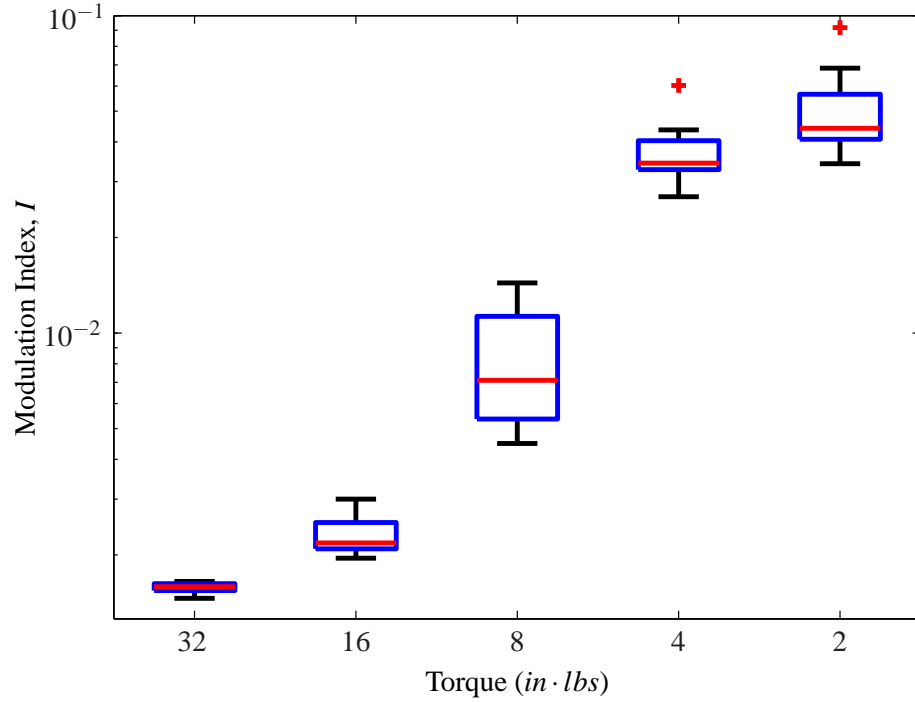


Figure 81: Distributions of the modulation index,  $I$ , versus bolt torque from ten repetitions of IM at each torque level for the three-beam, two-bolt structure.

Table 4: Three-beam, two-bolt results.

Torque on Bolt 1 ( <i>in · lbs</i> )	% Change in $I$
16	46.6
8	420.7
4	2,255
2	3,099

where

$$A = \frac{\max(I) + \min(I)}{2}$$

$$D = \min(I) + A$$

and B and C are tuned to fit the data. The blue line in Figure 82 shows  $I_{trend}$  for the three-beam data with a B=0.06 and C=87. This curve fit implies that, in agreement with Amerini and Meo, the

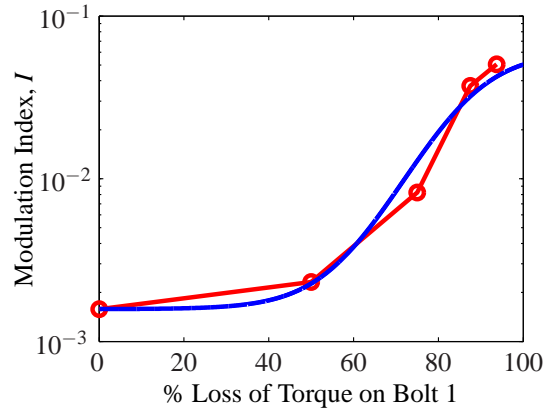


Figure 82: Mean  $I$  values versus percent loss in torque on bolt 1 (—) and a corresponding hyperbolic tangent curve fit (—) for the three-beam, two-bolt test results.

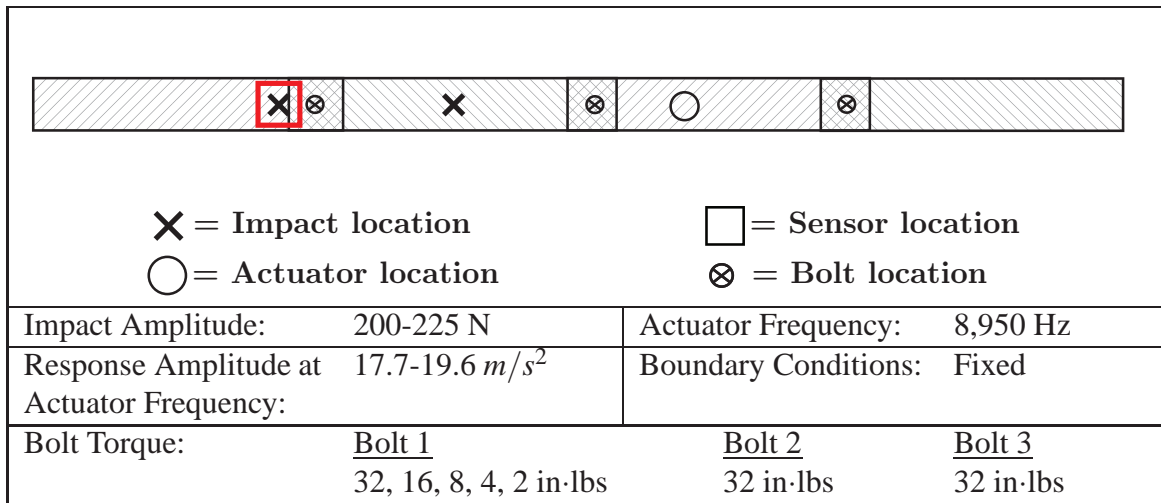


Figure 83: Setup and parameters for the four-beam, three-bolt IM testing.

hyperbolic tangent is a good approximation of the trend observed in  $I$  as bolt torque decreases. In addition, Equation (36) provides a potential method for quantifying the torque loss on the bolt.

#### Four-Beam, Three-Bolt Results

The three-beam, two-bolt structure used for the experiments in the previous section was expanded to the four-beam, three-bolt structure described in Section 4.1.4. Throughout all the tests on the four-beam structure, the torque on bolts 2 and 3 were kept at 32 in·lbs. IM tests were repeated with the torque on bolt 1 equal to 32, 16, 8, 4, and 2 in·lbs. Other tests parameters are listed in Figure 83. One sensor location and one impact location were used exclusively for these tests. Like the procedure detailed in the previous section, IM tests were repeated ten times for each torque case, and the value for  $I$  was calculated for each repetition. Figure 84 shows the results of these tests.

Unlike the three-beam results, the four-beam results show more overlap between the results

Table 5: Four-beam, three-bolt results.

Torque on Bolt 1 ( <i>in · lbs</i> )	% Change in <i>I</i>
16	25.2
8	2,679
4	6,536
2	5,508

from different torque cases. In addition, there is a decline in the *I* value when the torque on bolt 1 is loosened to 2 in·lbs. It is possible that this decline is a result of the loss of pre-load on the bolt. As concluded in Chapter 4.1, increasing the input force may increase the separation between cases. However, it is important to note that the results from the lowest three torque cases are distinct from the highest two. Table 5 lists the percent change relative to the baseline case in which the torque on bolt 1 was 32 in·lbs. It is clear that the changes in *I* reflect the change in bolt torque for the four-beam structure.

Next, a hyperbolic tangent curve of the form stated in Equation (36) was fit to the data. Figure 85 shows the mean values of *I* from the results shown in Figure 84 in red.  $I_{trend}$  was calculated with  $B=0.09$  and  $C=77$  and is shown in blue. This approximation accurately characterizes the trend in *I* as the torque on bolt 1 changes. The results from this data and the data presented for the three-beam structure support the quantification of bolt torque loss using a hyperbolic tangent curve fit.

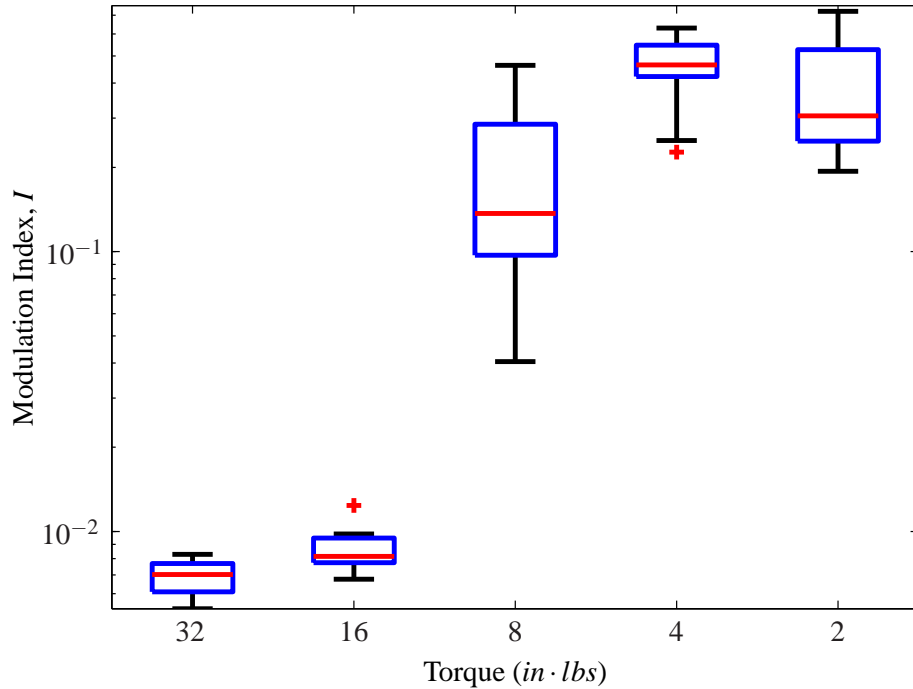


Figure 84: Distributions of the modulation index,  $I$ , versus bolt torque from ten repetitions of IM at each torque level for the four-beam, three-bolt structure.

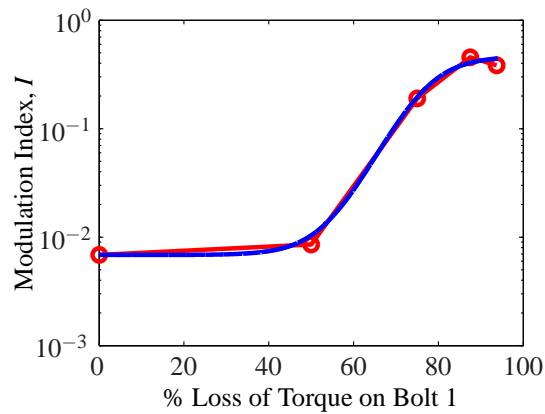


Figure 85: Mean  $I$  values versus percent loss in torque on bolt 1 (—) and a corresponding hyperbolic tangent curve fit (—) for the four-beam, three-bolt test results.

### Satellite Panel Results

The same analysis performed on the three-beam and four-beam structures was repeated on the satellite panel setup, described in detail in Section 4.1.5. Ten repetitions of IM tests were performed for each torque case in which all four bolts were torqued to 24, 16, 8, 4, 2, and 1 in·lbs. Figure 86 shows other test parameters including impact, actuator, and sensor locations. The impact and sensor locations were chosen to be near the attached plate. Optimization of sensor, impact and actuator locations is left for future work. Figure 87 shows the box-and-whiskers plot for the data

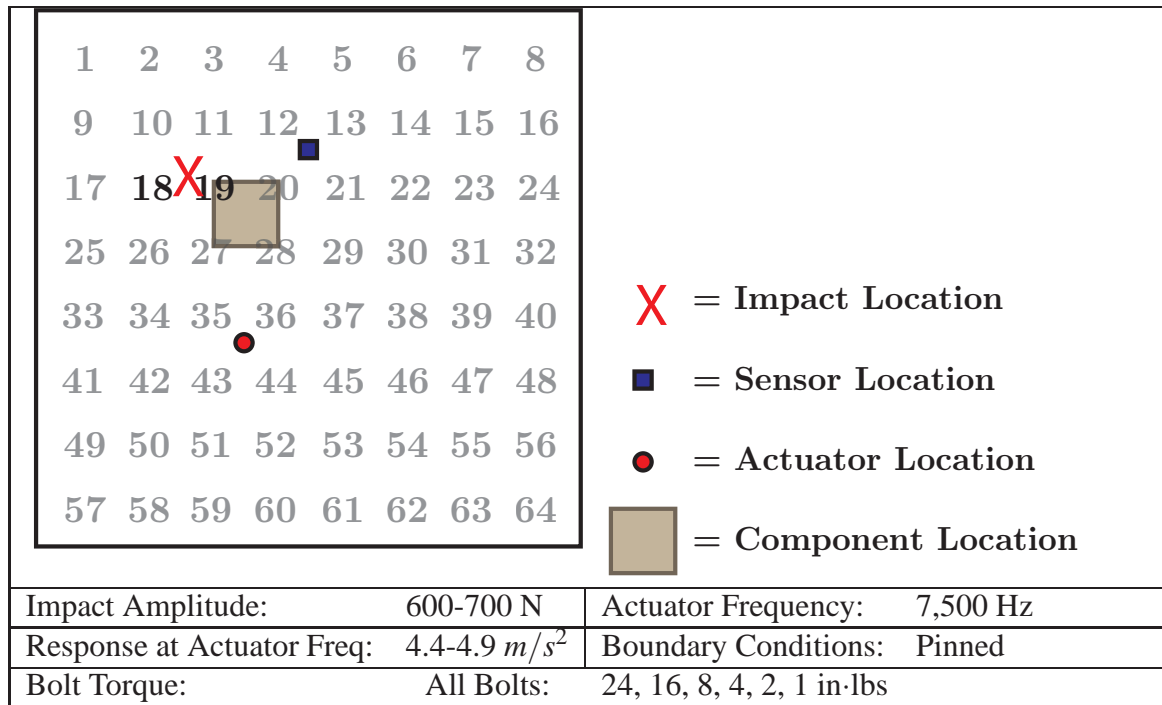


Figure 86: Setup and parameters for satellite panel IM testing.

collected from all the IM tests. The results are similar to those observed for the four-beam structure. The results from the lowest torque cases are separated from the results from the highest torque cases, but there is still overlap amongst the results from the lowest and amongst the results from the highest torque cases. Increasing the input amplitude may help differentiate the results from the different torque cases more clearly. However, the trend in the data noted throughout this chapter is clearly present: the modulation index,  $I$ , tends to grow as the torque on the bolt is reduced. In addition, as Table 6 shows, the change in the values of  $I$  as bolt torque decreases are able to identify the loss of torque on the bolts. The exception here is the 16 in-lb case, which represents only a 33% loss of torque on the bolts.

Next, Equation (36) was fit to the data. Figure 88 shows the mean  $I$  values in red and the curve fit with  $B=.09$  and  $C=88$  in blue. Interestingly, the  $B$  value for this plot is the same as the  $B$  value used in the four-beam curve fit. This observation supports the qualitative observation made earlier that the results from these two structures appear to be similar. The hyperbolic tangent curve fit for this case fits well, which further indicates the effectiveness of this type of curve to quantify the loss of torque on the bolts within a structure.

### PnP Satellite Results

The last test case used to explore the effectiveness of using the modulation index,  $I$ , to identify the presence of loose bolts within a structure was performed on a fully assembled PnP satellite. Access to this satellite was granted for a limited amount of time, so performing repetitions of data sets was not possible. Figure 91 shows the PnP satellite with several external components bolted on to its frame. One of these components was secured to the frame via an L-shaped bracket and four bolts. This bracket, shown from several angles in Figure 91, is the focus of this investigation.

Table 6: Satellite panel results.

Torque on Bolts ( <i>in · lbs</i> )	% Change in <i>I</i>
16	-13.3
8	22.5
4	908
2	2,629
1	2,259

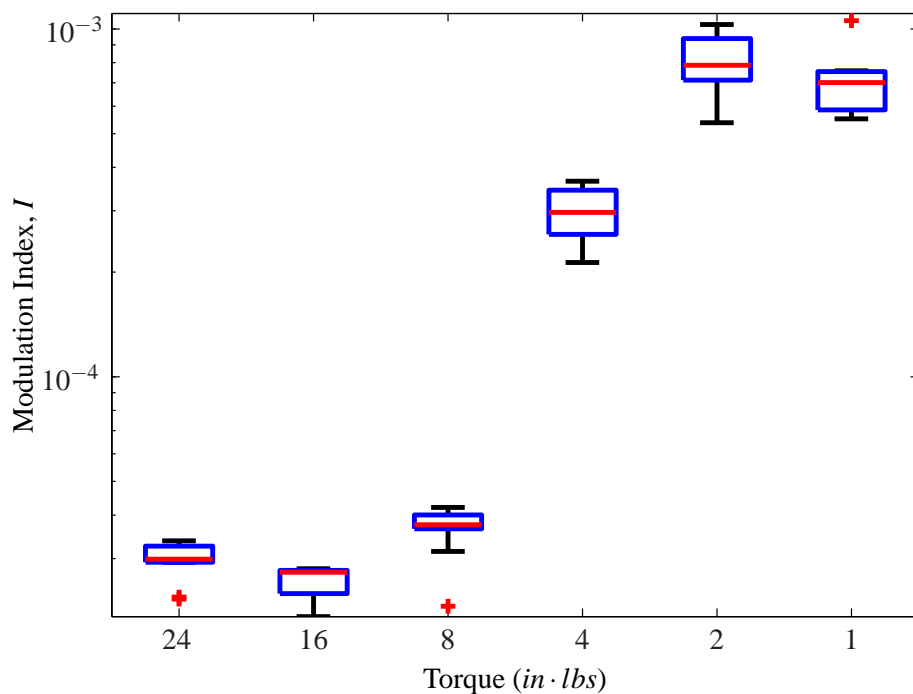


Figure 87: Distributions of the modulation index,  $I$ , versus bolt torque from ten repetitions of IM at each torque level for the satellite panel.

Note that some of the sensors shown in these pictures were not used for this analysis, as will be described below.

Figure 90 shows the testing parameters and setup used for the IM tests on the PnP satellite. The sensor, actuator, and impact locations were chosen to be near the bolts of interest. Throughout the tests performed for this study, the four bolts were all torqued to equal levels. IM testing

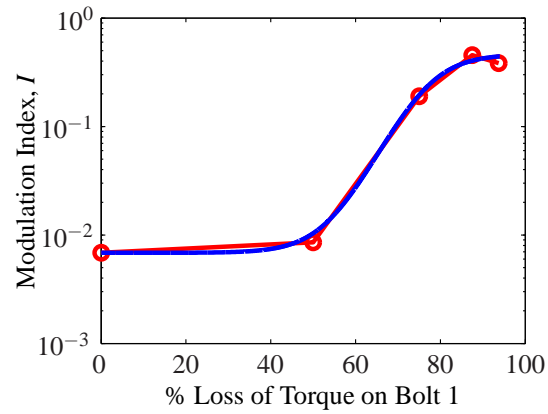


Figure 88: Mean  $I$  values versus percent loss in torque on the bolts (—) and a corresponding hyperbolic tangent curve fit (—) for the satellite panel test results.

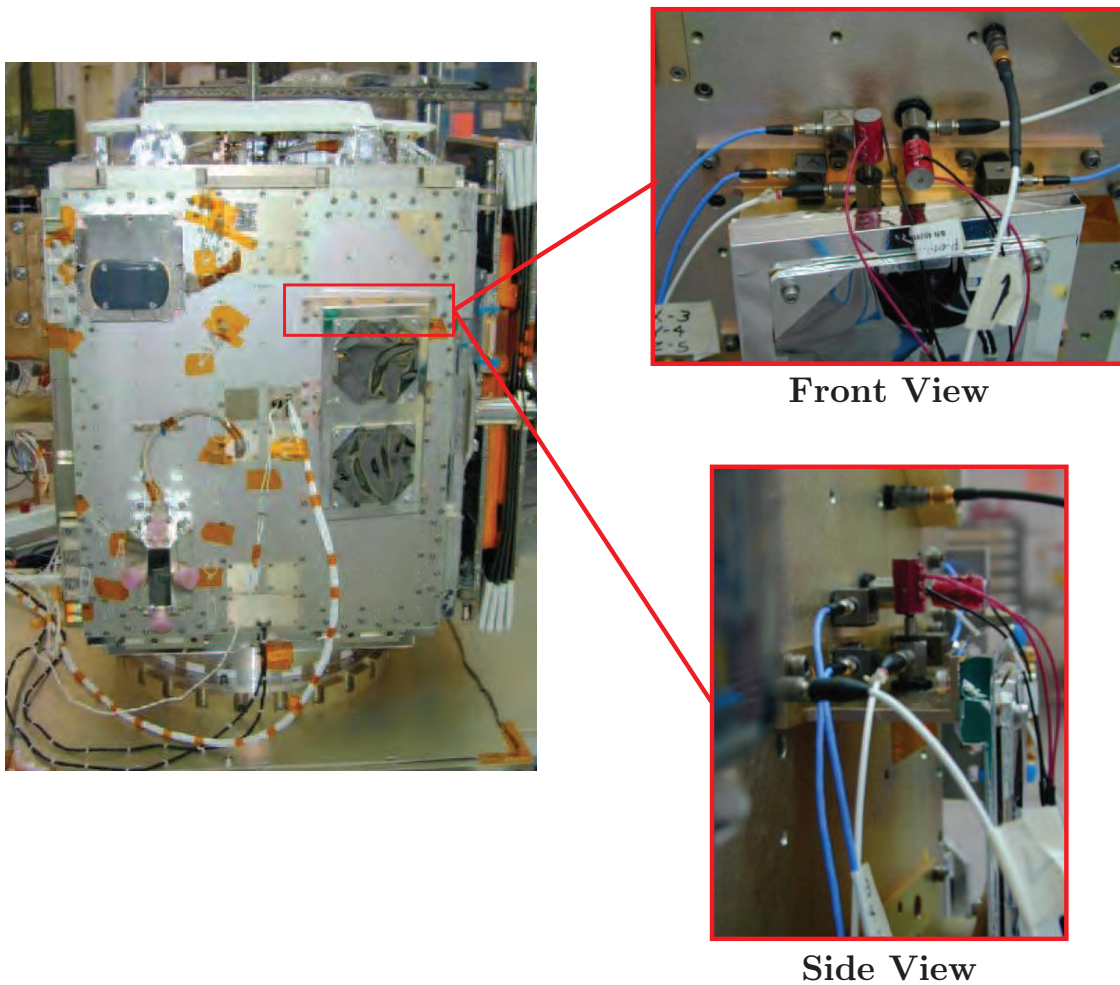


Figure 89: PnP satellite with close-up views of the L-shaped bracket.

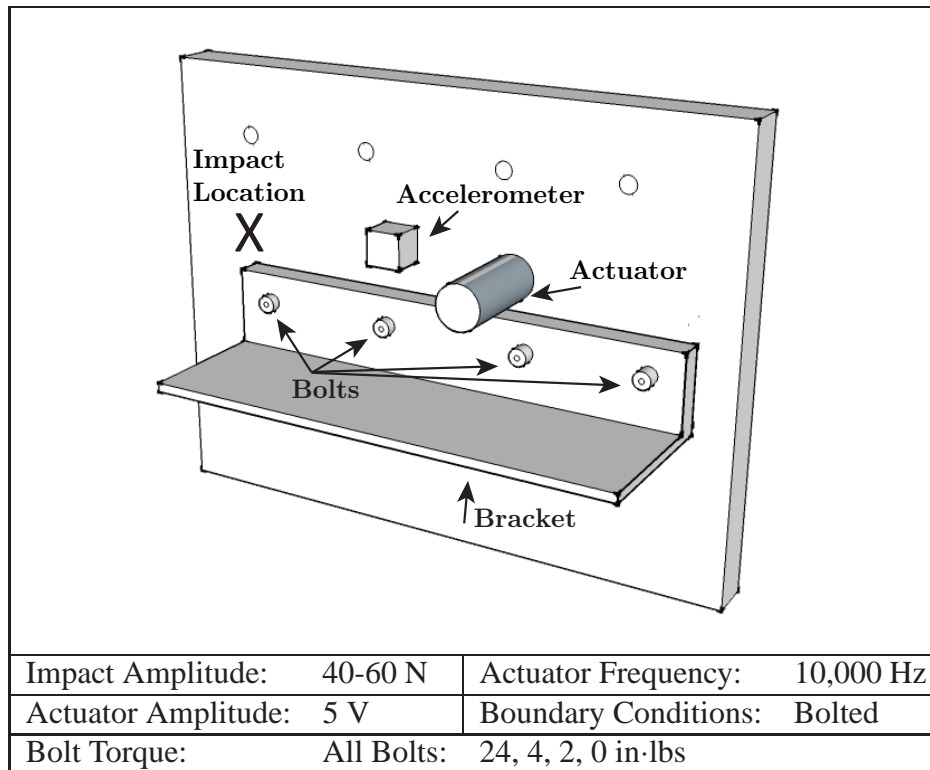


Figure 90: Setup and parameters for the PnP satellite IM testing.

was repeated with the torque on all the bolts equal to 24, 4, 2, and hand-tight, or 0 in-lbs. The same experimental procedure that was outlined in Section 4.2.1 was used except five repetitions per torque level (instead of three) were used for the averaging. In addition, a constant actuator amplitude was used for all the tests, because these test were performed before it was understood that the amplitude of response at the actuator frequency affects the amplitudes of the sidebands. However, the variation observed in the response amplitude at the actuator frequency across tests was not significant.

Figure 91 shows that  $I$  values calculated for the IM tests at the four torque levels. The values of  $I$  clearly increase as the torque on the bolts decrease. Table 7 shows the percent change in the  $I$  values from the 24 in-lb case. Although the percent changes are not as drastic as those observed for the other structures, the trend is clear. These results are important because they show that IM testing can be effective in identifying the presences of a loose bolt even in a fully assembled, complex structure.

**4.2.3 Conclusions.** The goal of the work presented in this chapter was to demonstrate the feasibility of using IM to track the status of the bolted joints within a structure over time. An analysis method based on the integration technique detailed in Section 3.1.2 was developed to calculate a modulation index,  $I$ . It was shown that  $I$  was a good indicator of the loss of torque on one or more bolts within a three-beam, two-bolt structure; a four-beam, three-bolt structure; a satellite panel; and on a fully assembled, PnP satellite. In addition, hyperbolic tangent curve fit was applied to describe the trend in the  $I$  data as torque loss progressed.



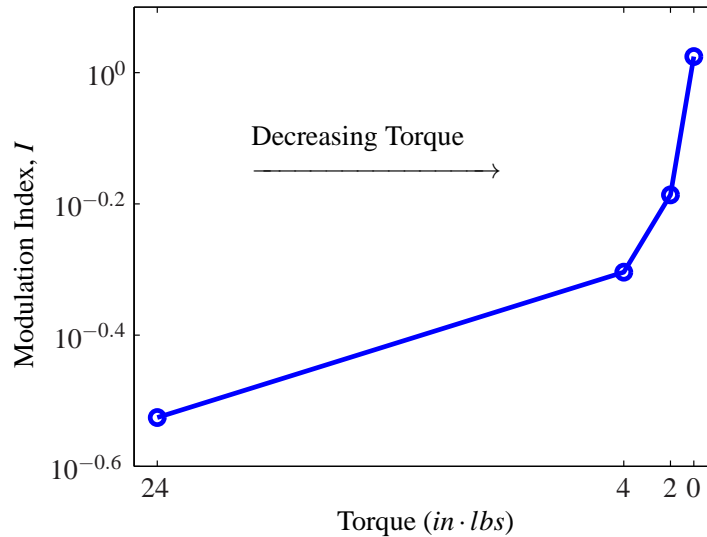


Figure 91:  $I$  values versus percent loss in torque on the bolts for the PnP satellite test results.

Table 7: PnP satellite results.

Torque on Bolts (in · lbs)	% Change in $I$
4	66.6
2	118.5
0	254.9

The analysis procedure presented in this chapter provides an alternate application of IM relative to the procedure outlined in Chapter 4.1. The advantage of the method presented in Chapter 4.1 is that it does not require historical reference data. While the method presented in this chapter does rely on historical data, its application is more time efficient, requiring only one impact location as opposed to an array of impact locations. Further work is necessary to optimize the test parameters such as impact, sensor and actuator location. Overall, the work presented in this chapter demonstrates the effectiveness of using IM to track the status of a bolt joint within a structure.

## 5.0 CONCLUSIONS

### 5.1 Conclusions

The main objectives of this work were to study the application of Impact Modulation (IM) to structures with bolted joints and to develop analysis methods that extract data from IM test results to diagnose the condition of the bolted joints within a structure. In particular, these analysis methods were to be applicable to quickly-built satellites that are currently being developed as an alternative to traditional satellite platforms. To accomplish these objectives, an experimental sensitivity analysis was conducted to verify that the response of a structure whose bolts were all properly torqued to IM testing was distinct from the response of a structure that contained a loose bolt. In addition, the sensitivity study identified the effects that changing certain test parameters had on the IM results. Analytical models were developed to establish a theoretical basis for the application of IM testing to structures with bolted joints. A sensitivity study using finite element-based simulations generated results that were compared to the results of the experimental sensitivity study. Based on the findings from these initial studies, two analysis methods were developed to diagnose the condition of the bolted joints within a structure. Finally, the effectiveness of these methods was demonstrated on several different bolted structures.

In Chapter 2, a two-beam, one-bolt structure was studied to develop an understanding of how sensitive IM test results are to certain test parameters and to changes in the torque on the bolt. Impact amplitude and location; actuator amplitude and frequency; and sensor location were varied to study each parameter's influence on the results of IM testing. The feature of interest when evaluating the response characteristics was the amplitude of the response at the sideband frequencies. It was found that the underlying linear dynamics of the system have great influence on IM results. The amplitude of the sidebands are linearly related to the amplitude of the response at the natural frequencies, which was shown by varying impact amplitude and impact location. By varying the actuator amplitude, it was shown that the trend in the growth of the sideband amplitudes mirrors the trend in the growth of the response at the actuator frequency. The linear dynamics of the structure at frequencies within the modulation range were shown to have a great affect on the IM results. If the linear response at a sideband frequency is of low magnitude, the sideband amplitude will also be relatively small. Conversely, if the response at the sideband frequency is large, the sideband amplitude will be relatively large. The study of the effect of sensor location on IM results was the least conclusive. It is believed that the linear operating deflection shapes at the sideband frequencies are correlated to the shape of the sideband amplitudes across sensor locations. However, this hypothesis was not decisively confirmed by experimental or simulation results. The most important conclusion drawn from the work in Chapter 2 was a result of studying the change in sideband amplitudes due to a change in torque on the bolt in the two-beam, one-bolt structure. Because the sideband amplitudes increased as bolt torque decreased, it was concluded that IM testing was a viable method to diagnose the condition of the bolts within a structure. It was upon this conclusion that the rest of the work was based. Finally, it was shown that IM results were robust to changes in boundary conditions.

In Chapter 3, a theoretical foundation was developed to support the experimental results mentioned above. A nonlinear, single degree of freedom model was derived and a closed-form solution was obtained to show the relationship between the sideband amplitudes and the amplitudes of response at the natural frequency and at the probing force (actuator) frequency. Then, a nonlinear

finite element model of the two-beam, one-bolt structure was presented and used to replicate the sensitivity study that was performed experimentally. The results of the analytical sensitivity study confirmed the conclusions drawn from the experimental work.

The next two chapters were devoted to developing analysis methods that could identify the presence of a loose bolt within a structure without a priori knowledge. In Chapter 4, a method based on quantifying the breakdown in the correlation between the approximated mode shapes estimated at the natural frequency and at the sideband frequencies was developed. The estimated mode shapes were identified from IM tests using impacts at an array of impact locations, similar to the procedure for modal analysis. An index, called the torque index ( $TI$ ), quantified the correlation between the shapes using a normalized dot product. The main advantage of this index is that it always falls in the interval  $[0,1]$ . These limits are structure-independent, eliminating the need for historical or baseline data. The effectiveness of  $TI$  to identify the presence of loose bolts within a structure was demonstrated on a three-beam, two-bolt structure; a four-beam, three-bolt structure; and a realistic satellite panel.  $TI$  was most effective in the tests on the beam assemblies, but the appropriate trend in  $TI$  was shown for the satellite panel. It was concluded that the most likely reason that  $TI$  was more effective in identifying the loose bolts in the beam assemblies is that impacts on the beam assemblies more effectively exercised the nonlinearities in the bolted joints by changing the contact surface area. An important conclusion drawn from these tests is that the impact amplitude must be sufficiently high in order to exercise these nonlinearities at the bolted joint. The appropriate level of impact force depends on the properties of the structure.

Finally, in Chapter 5, a second analysis method was developed to track the status of the bolted joints within a structure over time. This method assumes that IM data from a healthy structure is available. A modulation index,  $I$ , was defined to quantify the amount of modulation present near the actuator frequency. As was shown in the results of Chapter 2, the response of a healthy structure will contain less modulation than the response of a structure with loose bolts.  $I$  was measured for several structures with bolted joints and it was shown that the value of  $I$  grew as the torque on the bolts within the structures decreased. To generalize the trend in  $I$  as the torque on the bolts changes, a hyperbolic tangent curve was fit to each set of data. The curve fit matched the  $I$  data very well.

Overall, the main contribution of this work is that IM testing has been established as a viable method for identifying the presence of loose bolts within a structure. Experimental and analytical results support using changes in the sideband amplitudes measured in the IM results to indicate changes in bolt torque level. Analytical methods based on these changes in sideband amplitudes were shown to be effective in identifying loose bolts within increasingly complex structures.

## 5.2 Recommendations for Future Work

The use of IM is a new approach for diagnosing the condition of the bolts within a structure. Although this work addressed many aspects of applying IM to a structure, the opportunities for further research on this topic are plentiful. For example, during the analysis of the sensitivity study results, a conclusive explanation of how sensor location affected the IM results was not established. This issue highlights a larger aspect of IM that needs further study: the quantification of the sideband amplitude dependence on system and testing parameters. It has been established in this work that parameters such as impact amplitude and actuator frequency affect the sideband amplitudes, but some aspects of IM response, including why some linear modes are modulated

more strongly than others or what linear modes contribute to the operating shape at the sideband frequencies, are as of yet unexplained. It is likely that the underlying linear dynamics of the structure in the modulation range can account for some of the unexplained phenomena, and future work should address how to quantify its effects.

In terms of the analytical analysis, the finite element model presented in this work accurately captured many of the phenomena observed experimentally. The exception to this accuracy was the model's ability to simulate the breakdown in mode shape approximations observed experimentally at low bolt torque levels. Improvements to the model could include adding the effects of damping in the shearing, or tangential, direction in the joint model. Also, expanding the finite element model to a three-dimensional model would allow the coupling between dynamics in the normal and tangential directions to be studied.

The analysis methods presented here could also be further studied and improved by conducting experiments to optimize test parameters. Of particular interest would be the optimum placement of the actuator and the minimum number of impacts necessary to diagnose a loose bolt. In addition, methods to locate the loose bolt within the structure would greatly enhance the value of these analysis methods. Another important issue that was not addressed in this work was the ability to identify a feature in the data that uniquely characterizes bolt torque loss. In other words, a method for directly attributing changes in IM results to changes in bolt torque as opposed to changes in other nonlinearities in the system would be desirable.

In conclusion, future efforts should build on the foundation established in this work to improve and expand the applications of IM testing for the identification of loose bolts within a structure.

## References

- [1] B.J. Arritt, S.J. Buckley, J.M. Ganley, J.S. Welsh, B.K. Henderson, M.E. Lyall, A.D. Williams, J.C. Prebble, J. DiPalma, G. Mehle, and Roopnarine. Development of a satellite structural architecture for operationally responsive space. In *Proceedings of The International Society for Optical Engineering (SPIE)*, volume 6930, 2008.
- [2] A. Bhopale and C. Finley. How ORS will answer the 7-day tier-2 challenge. In *7th Responsive Space Conference*, April 27-30, 2009.
- [3] K.E.A. Van Den Abeele, P.A. Johnson, and A. Sutin. Nonlinear elastic wave spectroscopy (NEWS) techniques to discern material damage, part I: Nonlinear wave modulation spectroscopy (NWMS). *Research in Nondestructive Evaluation*, 12(1):17 – 30, 2000.
- [4] D. Donskoy, A. Sutin, and A. Ekimov. Nonlinear acoustic interaction on contact interfaces and its use for nondestructive testing. *NDT&E International*, 34(4):231 – 238, 2001.
- [5] S. Ritdumrongkul, M. Abe, Y. Fujino, and T. Miyashita. Quantitative health monitoring of bolted joints using a piezoceramic actuator-sensor. *Smart Materials and Structures*, 13(1):20 – 29, 2004.
- [6] S. Park, C.B. Yun, Y. Roh, and J.J. Lee. PZT-based active damage detection techniques for steel bridge components. *Smart Materials and Structures*, 15(4):957 – 966, 2006.
- [7] J. Guarino, R. Hamilton, and W. Fischer. Acoustic detection of bolt detorquing in structures. *Proceedings of Meetings on Acoustics*, 6(1):065002–065002–17, 2009.
- [8] E.H. Clayton, M.B. Kennel, Fasel T.R., M.D. Todd, M.C. Stabb, and B.J. Arritt. Active ultrasonic joint integrity adjudication for real-time structural health monitoring. In *Proceedings of the 15th SPIE Smart Structures and Materials & Nondestructive Evaluation and Health Monitoring*, 2008.
- [9] S.E. Olson, M.P. DeSimio, and M.M. Derriso. Fastener damage estimation in a square aluminum plate. *Structural Health Monitoring*, 5(2):173–183, 2006.
- [10] C.K. Coelho, S. Das, A. Chattopadhyay, A. Papandreou-Suppappola, and P. Peralta. Detection of fatigue cracks and torque loss in bolted joints. In *Health Monitoring of Structural and Biological Systems, Proceedings of SPIE*, volume 6532, pages 6532–6504, 2007.
- [11] L. Moniz, J.M. Nichols, C.J. Nichols, M. Seaver, S.T. Trickey, M.D. Todd, L.M. Pecora, and L.N. Virgin. A multivariate, attractor-based approach to structural health monitoring. *Journal of Sound and Vibration*, 283(1-2):295 – 310, 2005.
- [12] P.A. Lovell and D.J. Pines. Damage assessment in a bolted lap joint. In *5th Annual SPIE Smart Materials and Structures Symposium: Smart Buildings, Bridges, and Highways*, volume 3325, pages 112 – 126, 1998.

- [13] P. Driesch, J.A. Mann III, and H. Gangala. Identification of loose bolts using wavenumber filtering of low frequency vibration data. In *Proceedings of the National Conference on Noise Control Engineering*, volume 2, pages 769 – 774, 1996.
- [14] W.D. Reynolds, D. Doyle, and B. Arritt. Active loose bolt detection in a complex satellite structure. *Health Monitoring of Structural and Biological Systems 2010*, 7650(1):76500E, 2010.
- [15] V. Caccese, R. Mewer, and S.S. Vel. Detection of bolt load loss in hybrid composite/metal bolted connections. *Engineering Structures*, 26(7):895 – 906, 2004.
- [16] F. Amerini and M. Meo. Structural health monitoring of bolted joints using linear and non-linear acoustic/ultrasound methods. *Structural Health Monitoring*, 2011.
- [17] A. Milanese, P. Marzocca, J.M. Nichols, M. Seaver, and S.T. Trickey. Modeling and detection of joint loosening using output-only broad-band vibration data. *Structural Health Monitoring*, 7(4):309–328, 2008.
- [18] J.M. Nichols, S.T. Trickey, M. Seaver, S.R. Motley, and E.D. Eisner. Using ambient vibrations to detect loosening of a composite-to-metal bolted joint in the presence of strong temperature fluctuations. *Journal of Vibration and Acoustics*, 129(6):710 – 717, 2007.
- [19] E.E. Ungar. The status of engineering knowledge concerning the damping of built-up structures. *Journal of Sound and Vibration*, 26(1):141 – 154, 1973.
- [20] A.A. Ferri. Friction damping and isolation systems. *Journal of Vibration and Acoustics*, 117(B):196–206, 1995.
- [21] L. Gaul and R. Nitsche. The role of friction in mechanical joints. *Applied Mechanics Reviews*, 54(2):93–106, 2001.
- [22] D.J. Segalman. Modelling joint friction in structural dynamics. *Structural Control and Health Monitoring*, 13(1):430–453, 2005.
- [23] R.A. Ibrahim and C.L. Pettit. Uncertainties and dynamic problems of bolted joints and other fasteners. *Journal of Sound and Vibration*, 279(3-5):857–936, 2005.
- [24] H. Wentzel. Modelling of frictional joints in dynamically loaded structures-a review. Technical report, Department of Solid Mechanics, Royal Institute of Technology, 2006.
- [25] L. Gaul and J. Lenz. Nonlinear dynamics of structures assembled by bolted joints. *Acta Mechanica*, 125(1-4):169–181, 2005.
- [26] M. Oldfield, H. Ouyang, and J.E. Mottershead. Simplified models of bolted joints under harmonic loading. *Computers & Structures*, 84(1-2):25 – 33, 2005.
- [27] Y. Song, C.J. Hartwigsen, D.M. McFarland, A.F. Vakakis, and L.A. Bergman. Simulation of dynamics of beam structures with bolted joints using adjusted Iwan beam elements. *Journal of Sound and Vibration*, 273(1-2):249 – 276, 2004.



- [28] C.J. Hartwigsen, Y. Song, D.M. McFarland, L.A. Bergman, and A.F. Vakakis. Experimental study of non-linear effects in a typical shear lap joint configuration. *Journal of Sound and Vibration*, 277(1-2):327 – 351, 2004.
- [29] H. Ouyang, M.J. Oldfield, and J.E. Mottershead. Experimental and theoretical studies of a bolted joint excited by a torsional dynamic load. *International Journal of Mechanical Sciences*, 48(12):1447 – 1455, 2006.
- [30] M.H. Mayer and L. Gaul. Segment-to-segment contact elements for modelling joint interfaces in finite element analysis. *Mechanical Systems and Signal Processing*, 21(2):724 – 734, 2007.
- [31] Y. Ren, T. M. Lim, and M. K. Lim. Identification of properties of nonlinear joints using dynamic test data. *Journal of Vibration and Acoustics*, 120(2):324–330, 1998.
- [32] X. Ma, L. Bergman, and A. Vakakis. Identification of bolted joints through laser vibrometry. *Journal of Sound and Vibration*, 246(3):441 – 460, 2001.
- [33] M. Bowden and J. Dugundji. Joint damping and nonlinearity in dynamics of space structures. *AIAA Journal*, 28(4):740–749, 1988.
- [34] J. Esteban and C. A. Rogers. Energy dissipation through joints: theory and experiments. *Computers & Structures*, 75(4):347 – 359, 2000.
- [35] H. Ahmadian and H. Jalali. Identification of bolted lap joints parameters in assembled structures. *Mechanical Systems and Signal Processing*, 21(2):1041 – 1050, 2007.
- [36] H. Jalali, H. Ahmadian, and J.E. Mottershead. Identification of nonlinear bolted lap-joint parameters by force-state mapping. *International Journal of Solids and Structures*, 44(25-26):8087 – 8105, 2007.
- [37] H. Jalali, H. Ahmadian, and F. Pourahmadian. Identification of micro-vibro-impacts at boundary condition of a nonlinear beam. *Mechanical Systems and Signal Processing*, 25(3):1073 – 1085, 2011.
- [38] H. Ahmadian and H. Jalali. Generic element formulation for modelling bolted lap joints. *Mechanical Systems and Signal Processing*, 21(5):2318 – 2334, 2007.
- [39] A.A. Barhorst. Modeling loose joints in elastic structures-variable structure motion model development. *Journal of Vibration and Control*, 14(11):1767–1797, 2008.
- [40] S.J.I. Walker, G.S. Aglietti, and P. Cunningham. A study of joint damping in metal plates. *Acta Astronautica*, 65(1-2):184 – 191, 2009.
- [41] S.A. Nassar, V.L. Virupaksha, and S. Ganeshmurthy. Effect of bolt tightness on the behavior of composite joints. *Journal of Pressure Vessel Technology*, 129(1):43–51, 2007.
- [42] V. Zaitsev, V. Nazarov, V. Gusev, and B. Castagnede. Novel nonlinear-modulation acoustic technique for crack detection. *NDT&E International*, 39(3):184 – 94, 2006.

- [43] A.M. Sutin and D.M. Donskoy. Vibro-acoustic modulation nondestructive evaluation technique. *Proceedings of SPIE - The International Society for Optical Engineering*, 3397:226 – 237, 1998.
- [44] N.C. Yoder, D.E. Adams, and M. Triplett. Multidimensional sensing for impact load and damage evaluation in a carbon filament wound canister. *Materials Evaluation*, 66(7):756–763, 2008.
- [45] M. Meo, U. Polimeno, and G. Zumpano. Detecting damage in composite material using nonlinear elastic wave spectroscopy methods. *Applied Composite Materials*, 15(3):115 – 126, 2008.
- [46] V. Zaitsev and P. Sas. Nonlinear response of a weakly damaged metal sample: A dissipative modulation mechanism of vibro-acoustic interaction. *Journal of Vibration and Control*, 6(6):803–822, 2000.
- [47] M. Haroon and D.E. Adams. Implementation of nonlinear acoustic techniques for crack detection in a slender beam specimen. *Proceedings of the SPIE - The International Society for Optical Engineering*, 6935:69350 – 1, 2008.
- [48] C.R.P. Courtney, B.W. Drinkwater, S.A. Neild, and P.D. Wilcox. Factors affecting the ultrasonic intermodulation crack detection technique using bispectral analysis. *NDT&E International*, 41(3):223 – 234, 2008.
- [49] U. Polimeno and M. Meo. Understanding the effect of boundary conditions on damage identification process when using non-linear elastic wave spectroscopy methods. *International Journal of Non-Linear Mechanics*, 43(3):187 – 193, 2008.
- [50] P. Duffour, M. Morbidini, and P. Cawley. A study of the vibro-acoustic modulation technique for the detection of cracks in metals. *Journal of the Acoustical Society of America*, 119(3):1463 – 75, 2006.
- [51] N.C. Yoder and D.E. Adams. Vibro-acoustic modulation utilizing a swept probing signal for robust crack detection. *Structural Health Monitoring*, 9(3):257–267, 2010.
- [52] P.A. Johnson, A. Sutin, and K.E.A. Van Den Abeele. Applications of nonlinear wave modulation spectroscopy to discern material damage. In *2nd International Conference on Emerging Technologies in NDT, Athens (Greece)*, May 24-26, 1999.
- [53] A.H. Nayfeh and D.T. Mook. *Nonlinear Oscillations*. Wiley-VCH, 1995.
- [54] M. Geradin and D. Rixen. *Mechanical Vibrations: Theory and Applications to Structural Dynamics*. Wiley, 1997.
- [55] K.E.A. Van Den Abeele, J. Carmeliet, J.A. Ten Cate, and P.A. Johnson. Nonlinear elastic wave spectroscopy (news) techniques to discern material damage, part ii: Single-mode nonlinear resonance acoustic spectroscopy. *Research in Nondestructive Evaluation*, 12(1):31–42, 2000.



- [56] S. Underwood, D.E. Adams, D. Koester, M. Plumlee, and B. Zwink. Structural damage detection in a sandwich honeycomb composite rotor blade material using three-dimensional laser velocity measurements. In *Annual Forum Proceedings - AHS International*, volume 3, pages 2687 – 2696, Grapevine, TX, United states, 2009.
- [57] A.K. Pandey, M. Biswas, and M.M. Samman. Damage detection from changes in curvature mode shapes. *Journal of Sound and Vibration*, 145(2):321 – 332, 1991.
- [58] R.J. Allemang and D.L. Brown. A correlation coefficient for modal vector analysis. *Proceedings, International Modal Analysis Conference*, pages 110–116, 1982.
- [59] C. Andrew, J.A. Cockburn, and A.E. Waring. Metal surfaces in contact under normal forces: some dynamic stiffness and damping characteristics. *Proceedings of the Institute of Mechanical Engineering*, Part 3K:92100, 1968.

## Appendix A: Simulation Parameters and MATLAB Code

```
%2 Beam Model
%Models beams with N nodes---2N=total # of nodes

%Note: Odd nodes are translational nodes, even nodes are rotational nodes

clear all
close all
clc

global N

N=10;    %N/2 nodes per bar

%-----%
%%MATERIAL PROPERTIES%%
%-----%
%Input properties for beam 1
L1=.266*1e3;    %length of beam (mm)
E1=68.9e9/(1e3);    %Young's modulus (N/mm^2)
b1=.01905*1e3;    %length of cross section (mm)
h1=.00635*1e3;    %height of cross section (mm)
A1=b1*h1;    %Cross sectional area of bar (sq. mm)
rho1=2691/(1e3)^3;    %mass/volume (kg/mm^3)
I1=b1*h1^3/12;    %Area moment of inertia (mm^4)

%Input properties for bar 2
L2=.266*1e3;    %length of bar (mm)
E2=68.9e9/(1e3);    %Young's modulus (N/mm^2)
b2=.01905*1e3;    %length of cross section (mm)
h2=.00635*1e3;    %height of cross section (mm)
A2=b2*h2;    %Cross sectional area of bar (sq. mm)
rho2=2691/(1e3)^3;    %mass/volume (kg/mm^3)
I2=b2*h2^3/12;    %Area moment of inertia (mm^4)

%-----%
%%BOLT PROPERTIES%%
%-----%

%Define stiffness and damping of bolts
%k12=stiffness between bar1 and bar2, etc.

%Declare these parameters global so they can be used in the function Fbolt
global k1_sq k1_cube k12_sq k12_cube k3_sq k3_cube kr12_cube kr12_sq
k1=3e7; %3.1e1 ground spring (free) 3e7 (fixed)
k1_sq=0;
k1_cube=0;
c1=0.04;
kr1=3e1*1e3;%3.1e1*1e3 ground spring (free) 3e7*1e3 (fixed)
cr1=0.4;

k12=6e6;
k12_sq=-3e6;
k12_cube=0;
c12=.2;

kr12=6e6*1e3;%rotational stiffness (needed to couple rotatational and transverse d.o.f.s.
%In other words, it keeps the beams from flying off to infinity when a
%force is applied.
kr12_cube=0;
kr12_sq=-8e10*0;
cr12=.4;

k3=3e7; %3.1e1 ground spring (free) 3e7 (fixed)
```

```

k3_sq=0;
k3_cube=0;
c3=0.04;
kr3=3e1*1e3;%3.1e1*1e3 ground spring (free) 3e7*1e3 (fixed)
cr3=0.4;

%-----%
%%%TIME%%%
%-----%

%Define time vector
deltat=5e-6;
t=0:deltat:1.5;

%-----%
%%%INITIAL CONDITIONS%%%
%-----%

%First set all initial conditions to zero
qo=zeros(2*N,1);
qdoto=zeros(2*N,1);

%Define any nonzero initial conditions here:
% qo(3,1)=0; %initial displacement

%-----%
%%%BOLT INTERFACE FORCES%%%
%-----%
global Kbolt_lin C

%Assemble *linear* bolt stiffnesses
Kbolt_lin=zeros(2*N);
Kbolt_lin(1,1)=k1;
Kbolt_lin(2,2)=kr1;
Kbolt_lin(N-1,N-1)=k12;
Kbolt_lin(N-1,N+1)=-k12;
Kbolt_lin(N+1,N-1)=-k12;
Kbolt_lin(N+1,N+1)=k12;
Kbolt_lin(N,N)=kr12;
Kbolt_lin(N,N+2)=-kr12;
Kbolt_lin(N+2,N)=-kr12;
Kbolt_lin(N+2,N+2)=kr12;
Kbolt_lin(2*N-1,2*N-1)=k3;
Kbolt_lin(2*N, 2*N)=kr3;

%Assemble *linear* bolt damping
C=zeros(2*N);
C(1,1)=c1;
C(2,2)=cr1;
C(N-1,N-1)=c12;
C(N-1,N+1)=-c12;
C(N+1,N-1)=-c12;
C(N+1,N+1)=c12;
C(N-1,N)=cr12;
C(N-1,N+2)=-cr12;
C(N+1,N)=-cr12;
C(N+1,N+2)=cr12;
C(2*N-1,2*N-1)=c3;
C(2*N-1,2*N)=cr3;

%*Nonlinear* bolt forces are calculated by the function Fbolt

%-----%
%%%M AND K MATRICES%%%
%-----%

global K

```

```

%Assemble M and K matrices

%First calculate K and M for each beam
%Beam 1
K1=zeros(2*N/2);
M1=zeros(2*N/2);
l1=L1/(N/2-1); %length of element
k1=E1*I1/l1^3*[12 6*l1 -12 6*l1;6*l1 4*l1^2 -6*l1 2*l1^2;-12 -6*l1 12 -6*l1;6*l1 2*l1^2 -6*
    l1 4*l1^2];
m1=rho1*A1*l1/420*[156 22*l1 54 -13*l1;22*l1 4*l1^2 13*l1 -3*l1^2;54 13*l1 156 -22*l1;-13*l1
    -3*l1^2 -22*l1 4*l1^2];
N1=N/2-1;
m1mod=ModifiedMassMatrix(l1,A1,rho1,'right'); %modify mass matrix for elements at lap joint

for nn=1:N1
    ktemp1=padarray(k1,[2*(nn-1),2*(nn-1)],'pre');
    ktemp2=padarray(ktemp1,[2*(N1-nn),2*(N1-nn)],'post');
    K1=K1+ktemp2;
    if nn~=N1
        mtemp1=padarray(m1,[2*(nn-1),2*(nn-1)],'pre');
        mtemp2=padarray(mtemp1,[2*(N1-nn),2*(N1-nn)],'post');
        M1=M1+mtemp2;
    else %adjust mass of last beam element to account for overlap
        mtemp1=padarray(m1mod,[2*(nn-1),2*(nn-1)],'pre');
        mtemp2=padarray(mtemp1,[2*(N1-nn),2*(N1-nn)],'post');
        M1=M1+mtemp2;
    end

    clear ktemp1 ktemp2 mtemp1 mtemp2
end

%Beam 2
K2=zeros(2*N/2);
M2=zeros(2*N/2);
l2=L2/(N/2-1);
k2=E2*I2/l2^3*[12 6*l2 -12 6*l2;6*l2 4*l2^2 -6*l2 2*l2^2;-12 -6*l2 12 -6*l2;6*l2 2*l2^2 -6*
    l2 4*l2^2];
m2=rho2*A2*l2/420*[156 22*l2 54 -13*l2;22*l2 4*l2^2 13*l2 -3*l2^2;54 13*l2 156 -22*l2;-13*l2
    -3*l2^2 -22*l2 4*l2^2];
N1=N/2-1;
m2mod=ModifiedMassMatrix(l2,A2,rho2,'left');

for nn=1:N1
    ktemp1=padarray(k2,[2*(nn-1),2*(nn-1)],'pre');
    ktemp2=padarray(ktemp1,[2*(N1-nn),2*(N1-nn)],'post');
    K2=K2+ktemp2;
    if nn==1 %adjust mass of the first beam element to account for overlap
        mtemp1=padarray(m2mod,[2*(nn-1),2*(nn-1)],'pre');
        mtemp2=padarray(mtemp1,[2*(N1-nn),2*(N1-nn)],'post');
        M2=M2+mtemp2;
    else
        mtemp1=padarray(m2,[2*(nn-1),2*(nn-1)],'pre');
        mtemp2=padarray(mtemp1,[2*(N1-nn),2*(N1-nn)],'post');
        M2=M2+mtemp2;
    end

    clear ktemp1 ktemp2 mtemp1 mtemp2
end

%Assemble into global K and M matrices

M=blkdiag(M1,M2);

K=blkdiag(K1,K2);

C=(C+15*M+8e-7*K);

%Adjust non-proportional damping

```

```

%NODES 4 and 7
C(8,8)=C(8,8)*2;%Mostly affects 3
C(14,14)=C(14,14)*2;%Mostly affects 3
%
% %NODES 5 and 6
C(10,10)=C(10,10)*5; %Mostly affects 2 and 4
C(12,12)=C(12,12)*5;%Mostly affects 2 and 4

%-----%
%%INTERNAL AND EXTERNAL FORCES%%
%-----%

%Create a function that calculates the internal forces f(q,qdot)
%Create a function that calculates the external forces g(q,t)

%-----%
%%SOLVE EQUATIONS OF MOTION%%
%-----%

%Choose constant parameters to be used in Newmark calculations
alpha=0;

%Newmark algorithm
[q, qdot, qdotdot, ExternalForce, InternalForce]=NewmarkAlgorithm(t, qo, qdoto, M, alpha, '
    InternalForce','ExternalForce');

```

---

```

function Fbolt=Fbolt(q)

%-----%
%This function calculates the nonlinear forces at the bolt interfaces
%-----%
%
% Name Description Size
%
%INPUT:
%
% q displacement at current time [N,1]
%
%OUTPUT:
%
% Fbolt Nonlinear force [N,1]
%
% N=# of degrees of freedom
%

global k1_sq k1_cube k12_sq k12_cube k3_sq k3_cube N kr12_cube kr12_sq

N1=N-1;
N2=N+1;
N3=2*N-1;

Fbolt=zeros(2*N,1);

Fbolt(1,1)=k1_sq*q(1)^2+k1_cube*q(1)^3;
Fbolt(N1,1)=k12_cube*(q(N2)-q(N1))^3+k12_sq*(q(N2)-q(N1))^2;
Fbolt(N2,1)=-k12_cube*(q(N2)-q(N1))^3-k12_sq*(q(N2)-q(N1))^2;
Fbolt(N3,1)=k3_cube*q(N3)^3+k3_sq*q(N3)^2;

Fbolt(N,1)=kr12_cube*(q(N+2)-q(N))^3+kr12_sq*(q(N+2)-q(N))^2;
Fbolt(N+2,1)=-kr12_cube*(q(N+2)-q(N))^3-kr12_sq*(q(N+2)-q(N))^2;

```

---

```

function InternalForce=InternalForce(q,qdot)

%-----%
%This function calculates the internal forces of the system.
%-----%
%
%   Name           Description           Size
%
%INPUT:
%
%   q               displacement at current time   [2N,1]
%   qdot            velocity at current time      [2N,1]
%
%OUTPUT:
%
%   InternalForce   Internal force               [2N,1]
%
%   N=# of degrees of freedom
%
global K Kbolt_lin C
InternalForce=(K+Kbolt_lin)*q+C*qdot+FboltN(q);

```

---

```

function Q=ExternalForce(q,t,jj)

%-----%
%This function calculates the external forces applied at each node at a
%given time.
%-----%
%
%   Name           Description           Size
%
%INPUT:
%
%   q               displacement at current time   [2N,1]
%   t               current time                  [1,1]
%
%OUTPUT:
%
%   Q               External Force               [2N,1]
%
%   N=# of degrees of freedom
%
%NOTE: the N used below is the number of nodes used. Therefore, 2N=# of
%degrees of freedom.
%-----%

global N ImpactTimeHistory

%%Create force vectors
F1e=zeros(N,1);
F2e=zeros(N,1);

%%%%%%%%%%%%%%%%%%%%%%%%%%%%%%%%%%%%%%%%%%%%%%%%%%%%%%%%%%%%%%%%%%%%%%%%
%%Define actuator force at chosen location:
%%%%%%%%%%%%%%%%%%%%%%%%%%%%%%%%%%%%%%%%%%%%%%%%%%%%%%%%%%%%%%%%%%%%%%%%

%Define external (applied) forcing on bar 1
F1e(7,1)=1000*sin(2*pi*9580*t);

```

```

%%%%%%%%%%%%%%%%%%%%%%%%%%%%%%%%%%%%%%%%%%%%%%%%%%%%%%%%%%%%%%%%%%%%%%%%
%Define Impact Force:
%%%%%%%%%%%%%%%%%%%%%%%%%%%%%%%%%%%%%%%%%%%%%%%%%%%%%%%%%%%%%%%%%%%%%%%%
    if t>.5 && t<(.01+.5)
        F1e(3,1)=1.5*ImpactTimeHistory(jj);
    end

%Assemble
Q=[F1e;F2e];

%%%%%%%%%%%%%%%%%%%%%%%%%%%%%%%%%%%%%%%%%%%%%%%%%%%%%%%%%%%%%%%%%%%%%%%%

function mmod=ModifiedMassMatrix(L,A,rho,orientation)

%L=length of element
%A=Area =b1*h1
%rho=mass density
%orientation=specifies whether the mass is added to the left or right end
%of the element

%Define shape functions (polynomial form)
N1=[2/L^3 -3/L^2 0 1];
N2=[1/L^2 -2/L 1 0];
N3=[-2/L^3 3/L^2 0 0];
N4=[1/L^2 -1/L 0 0];

if strcmp(orientation,'right')==1

    lstar=L-12.7; %127mm=length of overlap section

    for ii=1:4
        for jj=1:4
            eval(['T=conv(N' num2str(ii) ',N' num2str(jj) ');'])
            TI=polyint(T);
            temp=polyval(TI,lstar)-polyval(TI,0);
            M1(ii,jj)=rho*A*temp;
            temp2=polyval(TI,L)-polyval(TI,lstar);
            M2(ii,jj)=4*rho*A*temp2;
            clear T TI temp temp2
        end
    end

    mmod=M1+M2;

elseif strcmp(orientation,'left')==1

    lstar=12.7; %127mm=length of overlap section

    for ii=1:4
        for jj=1:4
            eval(['T=conv(N' num2str(ii) ',N' num2str(jj) ');'])
            TI=polyint(T);
            temp=polyval(TI,lstar)-polyval(TI,0);
            M1(ii,jj)=4*rho*A*temp;
            temp2=polyval(TI,L)-polyval(TI,lstar);
            M2(ii,jj)=rho*A*temp2;
            clear T TI temp temp2
        end
    end

    mmod=M1+M2;
end

```

## Appendix B: Newmark's Method MATLAB code

```
function [q, qdot, qdotdot, ExternalForce, InternalForce] = NewmarkAlgorithm(t, qo, qdoto, M
    , alpha, f, g)

%-----%
%%%Newmark's Implicit Integration Method%%%
%-----%
%-----%
%Solves  $M \ddot{q} + f(q, \dot{q}) = g(q, t)$  where
%   -qo and qdoto are known
%   -f and g can be linear or nonlinear
%-----%
%
%      Name           Description           Size
%
%INPUT:
%
%      t           time vector           [1,n]
%      qo          initial displacement   [N,1]
%      qdoto       initial velocity       [N,1]
%      M           Mass matrix           [N,N]
%      alpha       Newmark parameter      [1,1]
%      f           name of the internal force function   string
%                  NOTE: The function is a user-created
%                  file that defines the internal forces
%                  present in the system. The function
%                  must have two inputs: q, qdot.
%      g           name of the external force function   string
%                  NOTE: The function is a user-created
%                  file that defines the external forces
%                  present in the system. The function
%                  must have two inputs: q, t.
%
%OUTPUT:
%
%      q           displacement           [N,n]
%      qdot        velocity               [N,n]
%      qdotdot     acceleration           [N,n]
%      ENERGY     Total Energy           [1,n]
%
%      N=# of degrees of freedom
%      n=# of time steps
%-----%
%
%Define Newmark parameters
deltat=t(2)-t(1);
gamma=.5+alpha;
beta=.25*(gamma+.5)^2;
maxiter=100;
epsilon=1e-5; %1e-5
DOF=length(qo);

%Allocate space for q, qdot, and qdotdot vectors.

q=zeros(DOF,length(t));
qdot=zeros(DOF,length(t));
qdotdot=zeros(DOF,length(t));

%Assign initial displacements, velocities
q(:,1)=qo;
qdot(:,1)=qdoto;

%Calculate initial acceleration
fo=eval([f '(q(:,1),qdot(:,1))']);
go=eval([g '(q(:,1),0,1)']);
```



```

qdotdot(:,1)=inv(M)*(go-fo);

aa=0;%dummy variable used later

%Newmark algorithm
for jj=1:length(t)-1
    %Initial prediction
    qdot(:,jj+1)=qdot(:,jj)+(1-gamma)*deltat*qdotdot(:,jj);
    q(:,jj+1)=q(:,jj)+deltat*qdot(:,jj)+(.5-beta)*deltat^2*qdotdot(:,jj);
    qdotdot(:,jj+1)=0;

    %Calculate residual vector and check for convergence
    for ii=1:maxiter
        ff=eval([f '(q(:,jj+1),qdot(:,jj+1))']);
        gg=eval([g '(q(:,jj+1),t(jj))']);
        residual=M*qdotdot(:,jj+1)+ff-gg;

        if all(abs(residual)<= epsilon*abs(ff))
            clear ff gg residual
            break
        else
            %Calculate correction deltaq
            %Note: A user-created function 'JacobianMatrixN' should be
            %created to calculate the Jacobian matrix: dresidual/dq
            S=JacobianMatrixN(q(:,jj+1),qdot(:,jj+1),M,deltat,alpha);

            Si=inv(S);

            deltaq=-Si*residual;

            %Correct previous estimate
            q(:,jj+1)= q(:,jj+1)+deltaq;
            qdot(:,jj+1)=qdot(:,jj+1)+gamma/(beta*deltat)*deltaq;
            qdotdot(:,jj+1)=qdotdot(:,jj+1)+1/(beta*deltat^2)*deltaq;

            %Display warning if solution didn't converge
            if ii == maxiter
                aa=aa+1; %Keep track of how many time steps don't converge
                disp('Max iteration reached')
                disp(t(jj))
                temp=find(abs(residual)>= epsilon*abs(ff));
                disp('abs(residual)=')
                disp(abs(residual(temp)))
                disp('epsilon*abs(ff)=')
                disp(epsilon*abs(ff(temp)))
                disp('The offending node is:')
                disp(temp)
                clear temp
                if aa==10% If solution is diverging, give it up.
                    return%%%%%%%%%%%%
                end%%%%%%%%%%%%
            end
            clear ff gg residual S Si deltaq
        end
    end
end
end
end

```

---

```

function S=JacobianMatrix(q,qdot,M,deltat,alpha)

%
%This function calculates the Jacobian (iteration) matrix for Newmark.
%S = dresidual/dq

```

```

%S = df/dq +df/dqdot dqdot/dq +M dqdotdot/dq - dg/dq
%-----%
%
%      Name              Description              Size
%
%INPUT:
%
%      q              displacement at current time      [N,1]
%      qdot           velocity at current time          [N,1]
%
%OUTPUT:
%
%      S              Jacobian (iteration) matrix      [N,N]
%
%      N=# of degrees of freedom
%
%
%
%      global K Kbolt_lin C k1_sq k1_cube k12_sq k12_cube k3_cube k3_sq N kr12_cube kr12_sq k23_sq
%              k23_cube kr23_cube kr23_sq
%
%      %Newmark parameters:
%      gamma=.5+alpha;
%      beta=.25*(gamma+.5)^2;
%
%      %Form Kt matrix. Kt=df/dq.
%
%      %First calculate dFbolt/dq
%
%      %FOR BEAMS:
%      %*****
%      Ktemp=zeros(2*N);
%
%      %3BEAMS-----
%      N1=2*N/3-1;
%      N1r=2*N/3;
%      N2=2*N/3+1;
%      N2r=2*N/3+2;
%      N3=4*N/3-1;
%      N3r=4*N/3;
%      N4=4*N/3+1;
%      N4r=4*N/3+2;
%      N5=2*N-1;
%
%      Ktemp(1,1)=3*k1_cube*q(1)^2+2*k1_sq*q(1);
%
%      Ktemp(N1,N1)=-3*k12_cube*(q(N2)-q(N1))^2-2*k12_sq*(q(N2)-q(N1));
%      Ktemp(N1,N2)=-Ktemp(N1,N1);
%      Ktemp(N2,N1)=-Ktemp(N1,N1);
%      Ktemp(N2,N2)=Ktemp(N1,N1);
%
%      Ktemp(N1r,N1r)=-3*kr12_cube*(q(N2r)-q(N1r))^2-2*kr12_sq*(q(N2r)-q(N1r));
%      Ktemp(N1r,N2r)=-Ktemp(N1r,N1r);
%      Ktemp(N2r,N1r)=-Ktemp(N1r,N1r);
%      Ktemp(N2r,N2r)=Ktemp(N1r,N1r);
%
%      Ktemp(N3,N3)=-3*k23_cube*(q(N4)-q(N3))^2-2*k23_sq*(q(N4)-q(N3));
%      Ktemp(N3,N4)=-Ktemp(N3,N3);
%      Ktemp(N4,N3)=-Ktemp(N3,N3);
%      Ktemp(N4,N4)=Ktemp(N3,N3);
%
%      Ktemp(N3r,N3r)=-3*kr23_cube*(q(N4r)-q(N3r))^2-2*kr23_sq*(q(N4r)-q(N3r));
%      Ktemp(N3r,N4r)=-Ktemp(N3r,N3r);
%      Ktemp(N4r,N3r)=-Ktemp(N3r,N3r);
%      Ktemp(N4r,N4r)=Ktemp(N3r,N3r);
%
%      Ktemp(N5,N5)=3*k3_cube*q(N5)^2+2*k3_sq*q(N5);

```

```

%-----
%2BEAMS-----
% N1=N-1;
% N2=N+1;
% N3=2*N-1;
%
% Ktemp(1,1)=3*k1_cube*q(1)^2+2*k1_sq*(q(1));
% Ktemp(N1,N1)=-3*k12_cube*(q(N2)-q(N1))^2-2*k12_sq*(q(N2)-q(N1));
% Ktemp(N1,N2)=-Ktemp(N1,N1);
% Ktemp(N2,N1)=-Ktemp(N1,N1);
% Ktemp(N2,N2)=Ktemp(N1,N1);
% Ktemp(N3,N3)=3*k3_cube*q(N3)^2+2*k3_sq*(q(N3));
%
% Ktemp(N,N)=-3*kr12_cube*(q(N+2)-q(N))^2-kr12_sq*(q(N+2)-q(N));
% Ktemp(N,N+2)=-Ktemp(N,N);
% Ktemp(N+2,N)=-Ktemp(N,N);
% Ktemp(N+2,N+2)=Ktemp(N,N);
%
%-----

%*****

Kt=K+Kbolt_lin+Ktemp;

%Form Ct matrix. Ct=df/dqdot
Ct=C;

%Assemble S matrix.
S=Kt+gamma/(beta*deltat)*Ct+1/(beta*deltat^2)*M;

```

## DISTRIBUTION LIST

DTIC/OCF	
8725 John J. Kingman Rd, Suite 0944	
Ft Belvoir, VA 22060-6218	1 cy
AFRL/RVIL	
Kirtland AFB, NM 87117-5776	2 cys
Official Record Copy	
AFRL/RVSV/Whitney Reynolds	1 cy